STRUCTURAL HEALTH MONITORING USING LAMB WAVES ACTUATED BY SURFACE-MOUNTED PIEZOELECTRIC MATERIALS

By

Lassaad Mhamdi

A THESIS

Submitted to
Michigan State University
in partial fulfillment of the requirements
for the degree

MASTER OF SCIENCE

Civil Engineering

2011

ABSTRACT

STRUCTURAL HEALTH MONITORING USING LAMB WAVES ACTUATED BY SURFACE-MOUNTED PIEZOELECTRIC MATERIALS

By

Lassaad Mhamdi

Piezoelectric materials have gained wide acceptance in the world and have been successfully used in a myriad of applications (industrial, engineering, etc.) thanks to their potential and ability of electromechanical conversion. The research in this thesis focuses on exploring the capabilities of surface-mounted piezoelectric (PZT) patches in exciting and detecting lamb waves in order to assess the integrity of a sample of aluminum plates. Therefore, numerical and analytical formulations of the impedance of an unbonded PZT patch were conducted and two different S.H.M techniques: the ultrasonic nondestructive technique of pitch-catch and the traditional technique of phased arrays were studied. First, a free PZT patch was modeled both analytically and numerically in order to see how its impedance varies depending on its mechanical parameters. The modeling can help understanding the electromechanical behavior of the patch and control its quality before using it in SHM tasks. Second, the technique of pitch catch was used in order to study the effect of crack depth on the propagation of lamb waves. For this reason, experiments on aluminum plates with defects of variable depths were conducted and results show significant variations of the energy of the wave as function of the crack depth. Finally, the technique of phased arrays, using a linear array of piezoelectric patches, was investigated in order to focus the lamb waves in specific directions and enhance the detection of small notches manufactured in the aluminum plates. Results showed that the simple phased array made of six simple piezoelectric transducers was able to detect the notches predefined on the aluminum plates.

AKNOWLEDGEMENTS

In the name of Allah, the Most Beneficent, the Most Merciful

First and foremost, may all praise and glory be to Almighty “Allah” whom without his blessings and guidance, I would not be able to finish this thesis. Alhamdulillah, Thank you Allah for giving me the patience and the strength.

I would like to express my deepest gratitude and my most considerate acknowledgements to both my advisor, Dr. Nizar Lajnef and my co-advisor Dr. Jung Wuk Hong for their patient guidance, and their priceless, insightful and knowledgeable advices. Their incessant support and help have been of a great importance to me through this work. Most considerate acknowledgements and deepest gratitude are also due to Dr. Lalita Udpa for her support and help and for accepting to serve as a member of my committee.

Thanks are due to all the wonderful people and colleagues I had the great opportunity to know during the years I spent at Michigan State University. Without their generous support and help, this work would not be possible.

I am very grateful for all the members of my loving family and all my dearest friends for their encouragements. Words cannot express my gratitude for their continuous emotional support.

TABLE OF CONTENTS

LIST OF TABLES

LIST OF FIGURES

Chapter 1

Introduction

Repair, maintenance and rehabilitation of structures in different fields (aerospace engineering, maritime engineering, civil engineering, mechanical engineering, etc.) and sectors (government, private and commercial) are usually tasks that necessitate both considerable amounts of time and highly varying costs depending on the age of structures and on their importance. The United States spends yearly a huge amount of money, more than $200 billion, for only maintenance tasks (maintain buildings, bridges, aircraft, railroads, and other infrastructure). Maintenance of commercial US aircrafts, for example, is estimated to a quarter of operating costs. Approximately 200000 bridges in the US national inventory need either repair (because of structural deficiencies, deteriorations, reduced bearing capacities, etc.) or replacement (because of geometrical non conformity to new standards). Costs of reparation and maintenance in 2004, of some deficient and obsolete bridges were estimated to $12 billion as reported by the Federal Highway Administration in 2006 (FHWA). All those high costs of reparation and maintenance aim at reducing as maximum as possible the risk for the general public since the high number of damaged structures put the human safety in concern and any possible failure of a frequently used structure (aircraft, bridge, building, etc.) may lead to catastrophic results (loss of human lives, loss of the structure, etc.). Many examples of catastrophic failures of daily used structures show the big need for more advanced and accurate inspection methods that effectively reveal on time all the appropriate safety concerns. The most horrific bridge failure in the United States was the collapse in December 5, 1967 of the silver bridge which caused death of 46 people, serious injuries for 9 persons and struck fear across the US. Investigation of the wreckage of the bridge showed that the cause of the collapse was the failure of a single eyebar in a suspension chain, due to a small defect of 0.1 inch depth. A less horrific bridge failure, as measured in terms of loss of life was the collapse, on August 1, 2007, of the Mississippi River Bridge in Minneapolis which resulted in the loss of 13 lives and the injury of 145 persons. The National Transportation Safety Board (NTSB) cited in the investigation that a design flaw was likely the cause of the collapse. Both collapses were caused by small structural faults. In Train tracks, faults caused also approximately 1080 train accidents in 2005 which resulted in approximately $220 Million of equipment damages and $114 Million of track damages as reported by the Federal Railroad Administration in its annual report of 2005 (FHWA). In aviation industry, huge amount of money is spent yearly on maintenance of aircrafts which make the probability of failure less compared to the probability of failure in other industries. Despite all the effort made in inspection (high cost, long time of inspection, etc.), the frequency at which aircrafts are inspected is limited which may increase the chance of not detecting faults that may, depending on their severity, result in dramatic accidents that cause more and more costs and send more lives to death. The National Transportation Safety Board recorded two fatal accidents in 2006 due to structural faults, which resulted in the loss of 50 lives (NTSB).

All those dramatic accidents due to tiny structural blemishes put in evidence the great need for developing new accurate and reliable inspection techniques that can be implemented on different structures (bridges, aircrafts, railroads, buildings, etc.) in order to considerably enhance structural and human safety and reduce maintenance costs.

A massive scientific effort has been devoted during the two last decades to build up novel reliable techniques for the diagnosis and assessment of structures. Researchers have been trying to come up with new techniques that will grant efficient inspections, reduce considerably the cost of maintenance, eliminate unscheduled maintenance, address problems related to aging structures and extend the service life of expensive structures. The scientific endeavor has led to the development of many methods of inspection, the most important technique that has gained a momentum in use in industrial communities and much interest in scientific community is the Structural Health Monitoring (SHM). This technique has provided world-wide confidence and satisfaction leading to its acceptance as prominent and efficient approach of structural evaluation. Its concept is straightforward: every structure has sensitive features that are subjected to changes as the structure degrades and gets old with time, the idea behind the Structural Health Monitoring is to measure the changes of those sensitive structural features, collect and save periodical measurements and extract important information (dynamic signature of the structure, properties, etc.) in order to give a diagnosis and a prognosis (residual life, evolution of cracks and damage, etc.) of the structure at every moment during its service life.

SHM offered a significant boost to the area of health monitoring introducing powerful techniques of monitoring that improve the detection of damages, help reducing the maintenance costs, help reducing common design and technical errors and help enhancing the overall safety of structures. The most important potential of the technique, however, is that it enables continuous monitoring of structures. A SHM system mounted on a bridge, for example, could be used for incessant control of the structure, without interrupting the traffic and could help detecting small flaws in their beginning stages of growth. On aging aircrafts, SHM packages could be used to detect possible problems, help limiting unscheduled maintenance and help repairing the structure, when necessary, based on its condition. Many other SHM schemes have been successfully used for the inspection of other infrastructures (buildings, railroads, etc.). In all cases, safety of the structures could be enhanced and costs of maintenance could be reduced.

SHM is an area of growing interest due to its advantageous capabilities which put it in the forefront of the enabling technologies. Implementation of some SHM systems on existing structures, however, still faces many challenges such as the development of autonomous vibration transducers, self-powered inspecting systems, low power wireless systems.

(a) Shuttle Columbia During launching (b) Wreckage of the crashed shuttle

Figure 1.01: Crash of Shuttle Columbia on March 14, 2003 (www.life.com)

“For interpretation of the references to color in this and all other figures, the reader is referred to the electronic version of this thesis.”

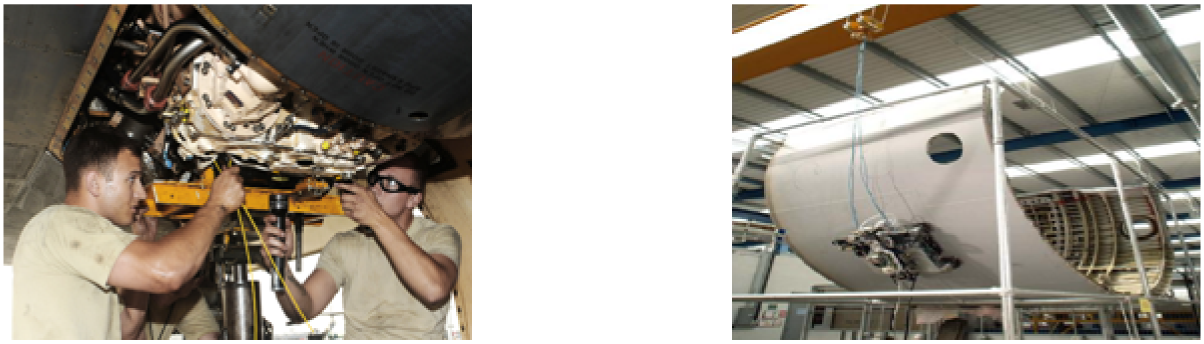

(a) Inspection of an aircraft (b) Robot inspection of a fuselage

Figure 1.02: Inspection of aircrafts (www.life.com)

1. Literature Review:

Tremendous amount of research has been conducted in the area of structural health monitoring. Many scientists excelled in this field and published valuable works in books and papers. The following is a literature review on the most important contributions that have been achieved on the area of structural health monitoring over the past few decades with an emphasis on works that involved the development of novel effective methods and schemes, especially methods which involve the use of Lamb waves.

1.1. SHM Overview:

During the last few decades, there has been a lot of interest, among researchers, in the field of Structural Health Monitoring; this growing interest has led to valuable advancement in inspection techniques. In fact, many inspection tasks that have been hard to carry out two decades ago due to different difficulties (complex structures, very small faults, etc.) are now feasible to accomplish due to the innovative brilliant and enabling techniques the SHM has brought. Many online monitoring operations that have been difficult to conduct, two decades ago, using the ordinary nondestructive evaluation (NDE) methods are now easy to perform using smart monitoring devices permanently mounted on structures. Several others methods of inspection have been put in practice and have showed a great success for the industrial community. The following is a chronological overview of the most important historical events and technological breakthroughs that led to the acceptance, among the world, of structural health monitoring as the preeminent most proficient inspection scheme.

The real beginning of the research on the structural health monitoring, started with the first IWSHM (International Workshop on Structural Health Monitoring) launched in 1997 by

Professor Fu-Kuo Chang and held at Stanford University. This workshop received an overwhelming success and was followed by a second workshop in 1999 where researchers emphasized on the identification of promising key technologies for industrial monitoring applications. From that time, researchers have devoted huge amounts of their times for the understanding of the concepts related to SHM and the development of new ideas, formulations and experiments in order to give answer to aroused questions related to inspection limitations. We count today more several journals and conferences throughout the world where big parts are devoted to the field of structural health monitoring. Many ideas and techniques that have been first proposed during conferences or first cited in journals can be now found fully documented on books, articles and review articles. The published documentation show that the first attempts on the development of new SHM techniques were first performed in order to find ways for the damage identification of structures under ambient and forced vibration. Doebling *et al* [10] presented the first review article on this issue where damage identification of structural and mechanical systems can be performed through the measurement of changes of vibration characteristics. The same authors published in the Shock and Vibration Digest in 1998 a revised and more condensed version of their 1996 review article. In 2001, Sohn *et al* [47] published an article in which they presented a general review of structural health monitoring from 1996 to 2001. Many others researchers excelled in the field and published many articles and books related to the field of structural health monitoring such as the book by Inman *et al* [26], the book by Balageas *et al* [06] the book by Giurgiutiu [21] in which he fully documented his work on the health monitoring of structures using Piezoelectric Wafer Active Sensors (PWAS), etc.

Ample literature on diversified methods and techniques related to the field of structural health monitoring is available on different manuscripts (books, articles, reports, reviews, web, etc). In this thesis, we emphasize on methods that involve the use of smart actuators and sensors for assessment and damage identification of structures, especially techniques that involve use of piezoelectric materials. Those techniques have gained wide acceptance due to the simplicity in implementation, efficiency and due to the numerous enabling features they present. In the following, a succinct description is given to highlight the importance of two main types of smart materials (magnetostrictive materials and fiber optic materials) and a more elaborated description is given to illustrate the efficiency of using piezoelectric materials for monitoring applications. The three smart materials greatly contribute to the evolution of the structural health monitoring area.

1.2. Magnetostrictive Transducers:

Ferroelectric and ferromagnetic materials (cobalt, nickel, iron, etc.) have the ability to undergo changes in size and/or shape in the presence of a magnetic field, this physical property is known as Magnetostriction. A magnetostrictive material undergoes changes in dimension when placed under a time varying magnetic field; it enlarges with positive magnetostriction and shrinks with negative magnetostriction, this effect is called the magnetostrictive effect. Inversely, a magnetostrictive material undergoes changes in its magnetic properties when subjected to a time varying stress field; this effect is referred to as the Villari effect. Both effects have been of great utility in structural health monitoring related tasks. The magnetostrictive effect has been used for actuating purposes; changes in shape of a ferroelectric-made transducer under a magnetic field induce vibrations in the structure on which the actuator is mounted, this will generate a wave that will propagates along the structure. The inverse magnetostrictive effect (Villari effect) has been used for sensing purposes; the same transducer is subjected to changes on its magnetic effect due to the presence of a propagating wave in the test structure. The changes in the magnetic properties of the transducer are recorded and saved in order to be analyzed. For example, the evaluation, using magnetostrictive materials, of the current state of a structure, is based on the comparison between baseline measurements from the structure in its healthy state and measurement from the structure in its actual state. Magnetostrictive actuators are first used to induce vibrations in the structure and magnetostrictive sensors are used to collect the dynamic response of the structure. The comparison between the two recorded signals is carried out using the mathematical processing technique of damage index in order to quantify the damage in the structure.

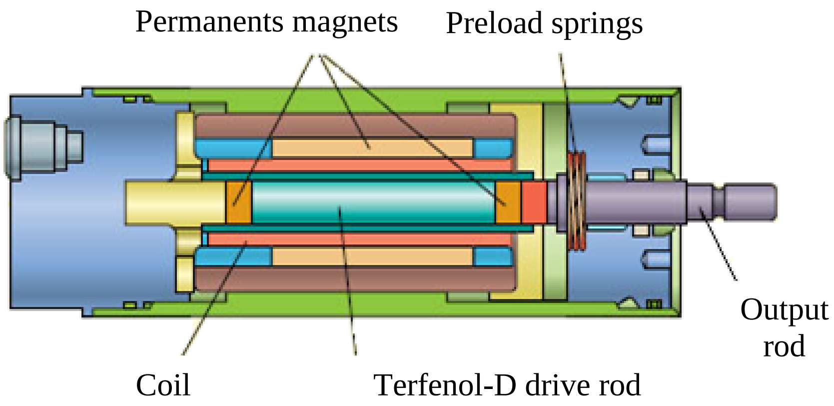

Figure 1.03: Smart Magnetostrictive Sensor

Many structural health monitoring tasks have been achieved using magnetostrictive materials. Weber *et al* [53] developed and characterized a method for the health monitoring of adhesive joints by incorporating magnetostrictive filler into the polymeric matrix. Light *et al* [32] developed a thin-nickel-strip magnetostrictive guided-wave sensor in order to monitor the growth of cracks and corrosion wall losses in piping and plates. Ghosh *et al* [14] proposed a new numerical method for the structural assessment of laminated composite beams with embedded magnetostrictive patches. Kwun *et al* [29] studied the feasibility of magnetostrictive sensors for the detection of corrosion near fasteners in aircraft wings and similar structures. Giurgiutiu *et al* [15] conducted an experimental study of magnetostrictive tagged composite strain response for health monitoring purposes.

1.3. Fiber Optic Sensors:

Optical fibers are thin, flexible, transparent cables that act as waveguides to transmit the light. They are made of plastic or glass cores and outer claddings which allow the transmission of the light to be carried only through the length and not through the lateral surfaces of the cables. Optical fibers have gained wide acceptance in the research and industrial communities due to their enabling capabilities and have been widely approved for several engineering applications. They have been successively applied in structural health monitoring applications due to their great ability of sensing and consequently detecting changes and damages in structures. The concept behind the technique of optical fiber is straightforward; an optical fiber embedded into a structure to be evaluated, represent a thin light pipe; changes and damages in the structure to be evaluated result directly on changes on the properties of the light (intensity, wavelength, phase, etc.. By sensing the variation of those properties, one can collect data that contain the information about the changes and the possible damages that are happening in the structure.

A typical fiber optic-based experiment involves embedding one optical fiber into a structure to be evaluated, use a source of light to generate a wave in one end of the optical fiber and use a photo-detector to sense the light in the other end. Three main techniques are used to sense the light, each rely on measuring the variation of one different property. The first method is based on sensing the intensity of the light and comparing the amount of light generated by the source to the amount captured by the photo-detector. Any damage in the structure will result on the variation of the amount of light transmitted through the optical fiber. The second method is based on the variation of the phase of the light. It resembles to the first method except that, in this method measurement are effectuated on the phase and not on the intensity of the light. The third conventional method relies on the measurement of the variation of the wavelength; this method is commonly known as Fiber Bragg Grating (FBG) (Figure 1.04). In this method, the form of the cable is different from the standard geometry; the plastic or glass core of the optical fiber contains equally spaced carves. When the wave encounter a carve, a small band of light will reflect back to the source. The presence of any damage in the structure will manifest in a shift in the reflected wavelength due to the presence of induced strain in carves. Measurements of the wavelength variations, helps quantifying the damages in the structure.

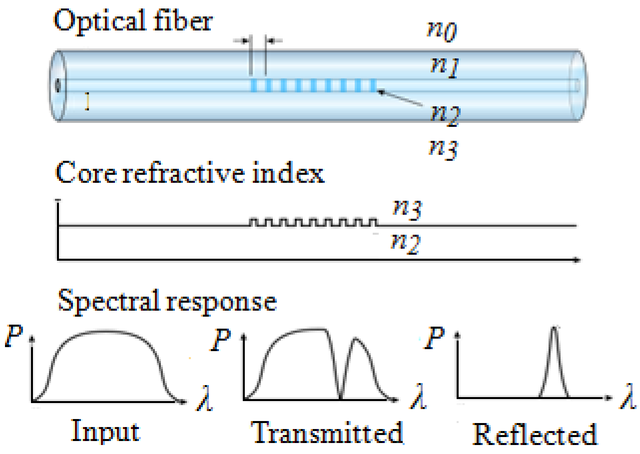

Figure 1.04: Fiber Bragg Grating method

Many researchers conducted studies on the practicability of using fiber optic based sensors for the health monitoring of structures. Rippet *et al* [45] showed the ability of an integrated simple microbend optical sensor to sense information on the elastic energy released by a host structure whenever damage is being introduced to it. Zhou *et al* [57] proposed a Fiber Bragg Grating sensor for the health monitoring of civil infrastructures. Ecke *et al* [11] used a network of multiplexed system of FGP strain and temperature sensors for the health monitoring of spacecrafts. Several other publications have contributed to the development of the fiber optic sensing technique. Measures [39] documents good contributions in his book and give an excellent review of optical sensors for health monitoring applications.

1.4. Piezoelectric Sensors:

Piezoelectric materials have been markedly used in a myriad of engineering applications due to the remarkable characteristics they present. They are known for their great inherited ability of electromechanical coupling, a property that allow the conversion of mechanical stimuli to electrical energy and inversely the conversion of electrical stimuli to a mechanical output. Piezoelectric materials are among the most frequently used materials for structural health monitoring. In most SHM related applications, transducers made of piezoelectric materials are surface mounted on host structures and used as sensors and/ or actuators depending on the SHM task. A piezoelectric material can perform as an actuator to induce vibrations in the host structures, as a sensor to sense vibrations and stress waves or as both an actuator and a sensor at the same time. In piezoelectric vibration-related SHM schemes, we distinguish two major techniques; the first technique is based on the measurement of the electrical impedance of the piezoelectric and the second technique is based on the propagation of waves in the host structure to which the piezoelectric is surface-mounted. The former is commonly known as impedance technique, the latter is termed wave propagation-based technique. For the impedance technique, the piezoelectric transducer is used to excite the host structure with a high frequency and sense its structural response. Any variation of the mechanical impedance of the host structure, due to the presence of damage, will generate a change on the impedance of the piezoelectric transducer

(Liang *et al* [31]). Damages in the structure are quantified based on the comparison of a baseline measurement of the structure with current measurements. Both measurements are carried out on the mechanical impedance of the host structure. Many authors contributed to the development and the improvement of the piezoelectric impedance-based technique. Park *et al* [41] presented a general review of the impedance technique, the theory behind it and stated results of some past experiments. Giurgiutiu *et al* [18] used the impedance technique for the detection of damages in aircraft structures. Grisso *et al* [22] applied the impedance technique with the aim to monitor the thermal protection systems on space shuttles. Park *et al* [42] also discussed the possibility of using the impedance technique for the detection of cracks in concrete structures. The second vibration-based technique that involves the use of piezoelectric transducers is the technique of wave propagation. This method of SHM differs from the impedance based technique in the concept, in the theory and in the applications. In a wave based technique, a piezoelectric device attached to the surface of a structure generates a stress wave when fed with an electrical input. The induced stress wave will propagate through the structure and interact with possible present defects and flaws. Comparison between baseline measurements and current measurements helps quantifying the damage and conducting a successful interrogation of the structure. The method of wave propagation has been in the forefront of the methods used for the nondestructive evaluation of structures. Perhaps lamb waves stand as the best proof for the success of wave based structural health monitoring techniques. Those waves have gained a momentum in use in the research and industrial communities due to their enabling capabilities. They are elastic waves capable of propagating for long distances in thin solid and shell structures. They remain constrained between the upper and the bottom surfaces of the structure, hence termed guided waves. A detailed description of lamb waves, including historical backgrounds, theoretical backgrounds, will be furnished in the third chapter of this thesis. Lamb waves have been extensively studied by many researchers and have been used in myriad of structural health monitoring applications. One among the first uses of lamb waves was to study the influence of the homogeneity of materials on the propagation behavior of the wave. Researchers then realized the sensitivity of lamb waves to the presence of damages in structures and components and started to use them for the detecting of possible flaws and cracks. Worlton *et al* [55] conducted the first ultrasonic testing using lamb waves in order to locate possible cracks in isotropic structures. They used two transducers, one as actuator and the other as receiver. Worlton and his group used the hypothesis of infinite surface because the formulation of lamb waves for semi-infinite and finite plates were not developed yet at that time. It was until a decade later when such an assumption was proposed by Torvik *et al* [49] who paved the way for other researchers interested in lamb waves to study the reflection from boundaries and the conversion of modes. Raghavan *et al* [44] presented a good review in which they gave a grasp of the lamb wave theory, discussed the use of several smart materials (magnetostrictive transducers, fiber optic transducers, piezoelectric transducers) to generate stress Lamb waves in isotropic plates, and included some examples of lamb wave based inspection in several areas (civil infrastructures, pipelines, aerospace, turbines, etc.). Another good review on nondestructive health monitoring based on wave propagation was presented by Giurgiutiu *et al* [20] in 2005. The authors enclosed a brief historical overview of NDE, a theoretical overview of lamb waves and discussed their use for health mentoring applications along with piezoelectric transducers. Some lamb waves techniques (pulse-echo and pitch-catch) used to identify and detect flaws and delaminations in composite structures were also discussed by the authors. Piezoelectric based Lamb waves were exploited by Giurgiutiu *et al* [18] in order to detect cracks near rivets on the panel of an aging aircraft in a pulse-echo configuration. Wang et *al* [51] introduced an active damage detection technique based on lamb wave propagation actuated by piezoelectric transducers in order to locate cracks and damages in an isotropic plate. Kim *et al* [28] proposed a new methodology based on lamb waves in order to detect damages in civil infrastructures (bridges, buildings, etc.). The technique does not rely on the use of baseline measurements to interrogate the health of the structure, rather on the polarization properties of the piezoelectric devices. Many other researchers combined experimental work with theoretical and/or numerical analysis in order to prove the efficiency of piezo-actuated waves damage detection techniques. Liu *et al* [34] investigated on the use of the finite element method to simulate the propagation of lamb waves actuated by Piezoelectric Wafer Actuated Sensors (PWAS). Lu *et al* [38] proposed also both an experimental study and a numerical modeling using the finite element method for the quantitative assessment of through-thickness crack sizes in a finite aluminum plate. Han *et al* [25] compared computational, experimental and theoretical results of the response of piezo-actuated lamb wave models in a thin aluminum plate in order to study the effect of variable isothermal and thermal gradient conditions on the propagation of the waves and hence on the detection of damages and cracks.

1.5. Issues in Structural Health Monitoring:

Many issues present barriers for judicious practical health monitoring. In many cases, several conventional techniques of structural health monitoring have been employed successfully. In some other cases however, many conventional techniques could not be adapted effectively. Such circumstances put in evidence the need for more advanced techniques in order to resolve the challenges. In lamb wave based health monitoring, two major techniques (Pitch-catch, Pulse-echo) have been used to interrogate, qualify and quantify damages in simple isotropic and composite structures. They have been satisfactory enough for certain structures. For many other structures with complex geometries, pitch-catch and pulse-echo are not suitable for efficient detection of damages and cracks in structural components. Complex structures usually present variable sections, geometries and shapes. It is impossible to mount the piezoelectric devices on some narrow, curved and angled parts and locations (welded joints, hard to reach locations, etc.). This makes the detection of cracks within those regions very cumbersome. Therefore, there has been an urgent need for the improvement of the conventional techniques based on guided wave inspection.

1.6. Phased Array Structural Health Monitoring:

In the quest for more reliable guided-wave propagation methods, the inspection using phased arrays is being actively pursued by many researchers. Phased array is an ultrasonic wave propagation-based technique, suitable for almost all tests where conventional methods have been traditionally used. It has been used in wide range of industrial applications (aerospace, pipelines, tubular manufacturing and maintenance and in other general manufacturing purposes). It uses an assembly of transducers arranged in a predefined form (one dimensional array, two dimensional arrays) in order to steer and focus all the waves induced by the elements of the array in one direction.

2. Thesis Overview:

2.1. Research Objectives:

Based on the literature review given above, one can underline the importance of the field of structural health monitoring for the assessment of structures. This field encompasses a number of interactive technologies and advanced procedures combined together in order to offer systems that can potentially interrogate structures by identifying possible damages and characterizing structural performances. The implementation of those systems on different structures can reduce the cost associated with inspection and maintenance as well as increase safety and save lives. The research in this thesis is conducted in order to prove the efficiency of using simple piezoelectric transducers for the detection of predefined notches manufactured on thin aluminum plates. The first main part of the thesis focuses on studying the impedance of the piezoelectric materials, that will be used in the experiments, by plotting analytical and numerical results and compare them. This study is of a great importance for checking the healthy state of the piezoelectric transducers and judge about their efficiency before using them in real experiments. The second part is devoted to the study of two basic techniques of ultrasonic structural health monitoring mainly the pitch catch technique and the phased array technique in order to show their efficiency in detecting the defects predefined on the aluminum plates. Both techniques will be presented in details in the following chapters and results of experimental testing will be analyzed and discussed.

Chapter 2

Piezoelectric Materials: Properties and Characteristics

1. Introduction to Piezoelectricity:

Etymologically, electricity by pressure or Piezoelectricity, as widely known, takes its root from the Greek word “piezein” which means “to squeeze” or “to press”. It characterizes the ability of certain materials (notably crystals and certain ceramics) to produce an electric potential in response to an applied mechanical stress and, conversely, generate a stress in response to an electric stimulus. The electric to mechanical conversion is called “direct piezoelectric effect” and the reversible effect is termed “converse piezoelectric effect”. All piezoelectric materials available in nature exhibit both the direct and the converse piezoelectric effects. The direct piezoelectric effect was discovered and initiated by the brothers Pierre and Jacques Curie. The Curies, who first observed this unusual property, combined their understanding of crystals with their knowledge in pyroelectricity and demonstrated in 1880 the direct piezoelectric effect using crystals of quartz and Rochelle salt. Subsequently, the converse process was predicted by the mathematician Gabriel Lippmann in 1881 and then immediately confirmed by the Curies.

Although discovered in in 1880, the first industrial applications of this fundamental breakthrough started in 1940-1950. Since then, piezoelectricity has been used in many fields mainly in electromechanical engineering applications: piezoelectric materials were notably used as electromechanical transducers such as echographic probes, sensors and actuators.

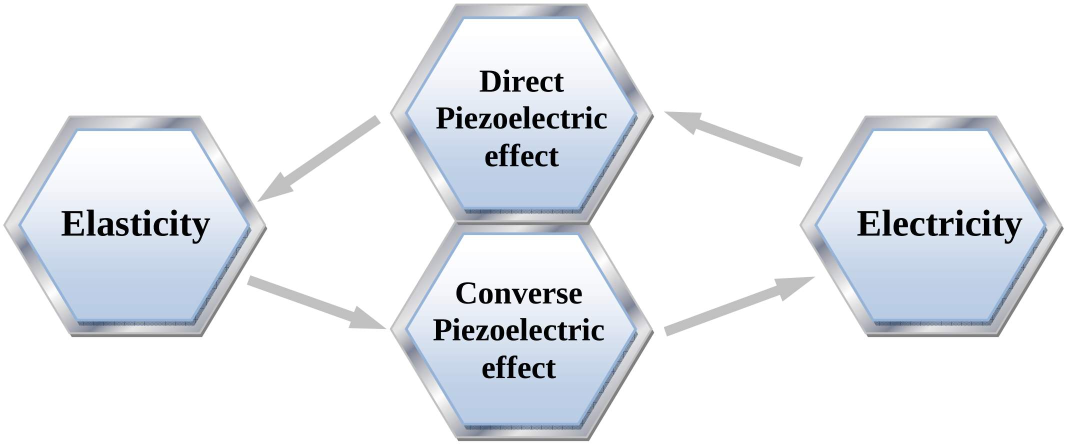

Figure 2.01: Coupling effects between Elasticity and Electricity

Recently, piezoelectric materials are used in myriads of engineering and industrial applications (power harvesting devices, ultrasonic probes, smart actuators and sensors for structural health monitoring, etc.).

2. Understanding of the Piezoelectric Effect:

When a piezoelectric material is subjected to a mechanical stress, intermolecular distances and forces vary. This variation manifests at the surface of the element by generation of small electrical dipoles. This process is called the piezoelectric effect and can be better understood by the explanation of its microscopic origins. A molecular model illustrating the piezoelectric effect is, illustrated in Figure 2.02. When the molecule is unperturbed, the centers of its positive and negative charges coincide and the external effects of the charges cancel out in a reciprocal way. As a result, the molecule remains neutral (Figure 2.02 (a)). However when the molecule is disturbed due to an external force or pressure applied on the material, its internal structure deforms which causes the separation of the positive and negative centers (Figure 2.02 (b)), thus small dipoles appears between two neighbors molecules (Figure 2.02 (c)). Inside the material the dipoles cancel mutually and charges appears only on the surface thus the material is polarized and an electric field is generated.

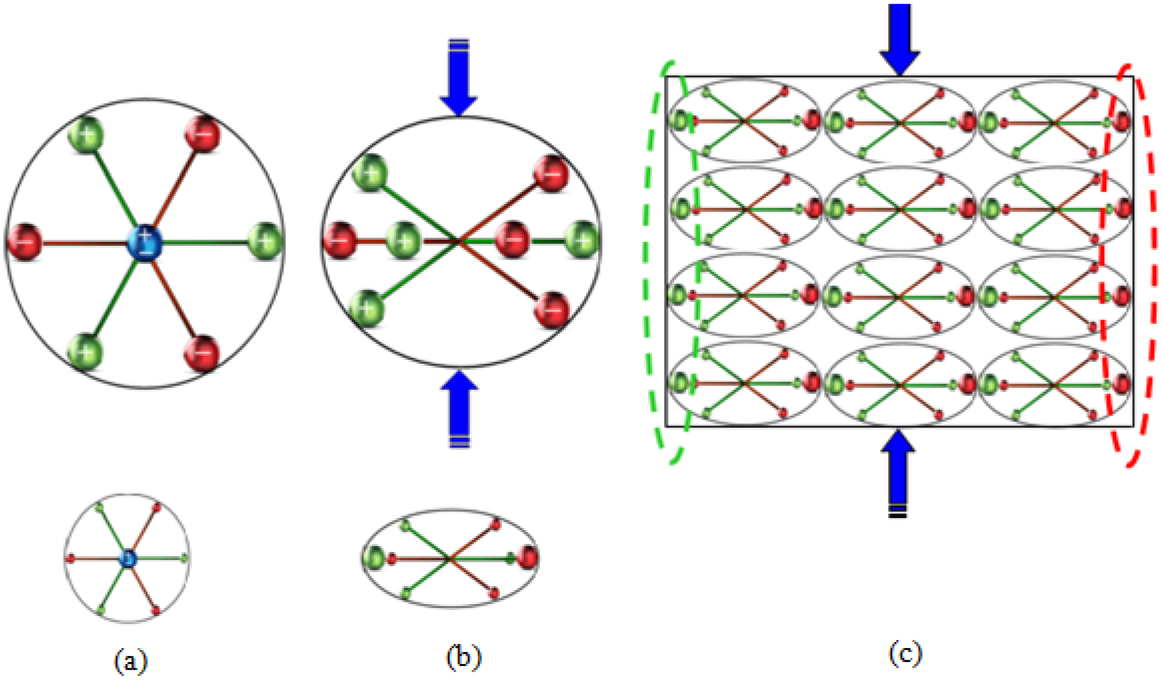

(a) (b) (c)

Figure 2.02: Molecular Modeling of Piezoelectricity Effect: (a) Unagitated Molecule, (b) Molecule under external stress (c) Polarization Effect

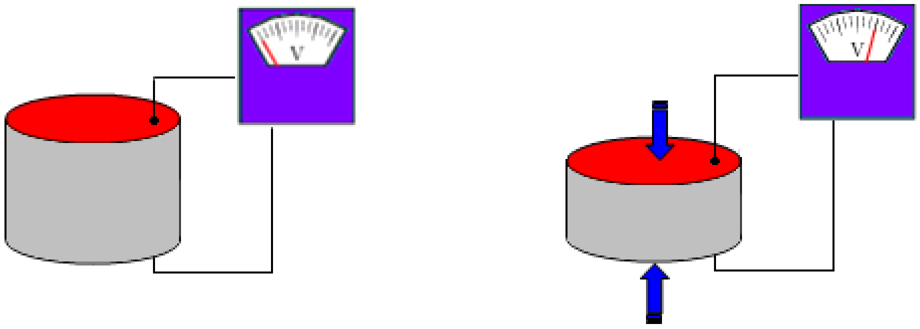

Figure 2.03: Polarization of the piezoelectric material and generation of electric field

3. Piezoelectric Materials:

We distinguish many materials that exhibit piezoelectric effects. Natural and artificial piezoelectric materials include quartz, Rochelle salt, Topaz, Tourmaline, Barium Titanate and Lead Zirconate Titanate. Each material responds differently to external stimuli (stress, pressure, electric field, etc.). Some of the materials, especially man-made materials containing Lead, raised big environmental concerns regarding toxicity. As a result, necessary iniatives have been taken in order to manufacture innovative lead-free materials, safe and friendly for the environment.

Many piezoelectric materials have gained wide applications in industry. The Lead-Zirconate Titanate $Pb(Zr,Ti)O_3$ and the Polyvinilidene Fluoride (PVDF) are among the most preferred candidates due to their actuating and sensing capabilities. The $Pb(Zr,Ti)O_3$ (PZT) is a synthetic compound formed by small ceramic particles obtained by calcination and grinding of different oxides. During the polarization step, the material is placed in a silicon oil bath at a temperature 150 ^oC and subjected to an electrical field of 3KV/mm for one minute. The $Pb(Zr,Ti)O_3$ (PZT) is known for its higher piezoelectric constant and can be used to manufacture many electronic components (ultrasonic transducers, ceramic resonators, ceramic capacitors, etc.) however it is very brittle. Unlike, $Pb(Zr,Ti)O_3$ (PZT), PVDF is a plastic material, It can be synthesized from the gaseous VDF monomer via a radical or controlled polymerization process followed by a melt casting process. When poled, PVDF exhibits efficient piezoelectric properties which make it very useful for many industrial applications. PVDF is a very flexible material, it allows the health monitoring of curved structures.

Single crystals piezoelectrics
(Quartz, Lead Magnesium Niobate)

Ceramic piezoelectrics
(Lead Zirconate Titanate, Lead Titanate)

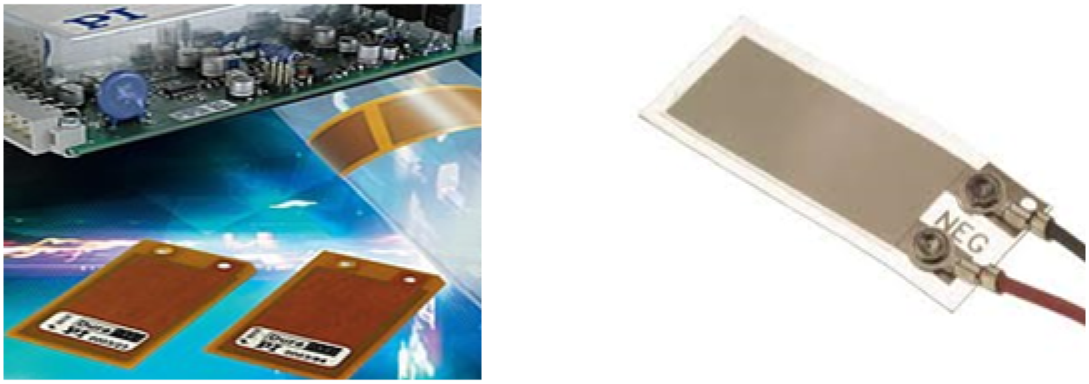

Composite piezoelectrics
(Ceramic polymer, ceramic glass)

Polymers piezoelectrics
(Polyvinilidene Fluoride (PVDF)

Figure 2.04: Different natural and made-up piezoelectric materials

3.1. Polarization of Piezoelectric Materials:

Polarization in electricity is commonly known as the rearrangement of the intermolecular distances and the shifting of positive and negative electric charges in opposite directions within a dielectric material under an external electric field. This physical property is applied for almost all piezoelectric materials which are not naturally polarized. For ceramic piezoelectrics, for example, the polarization is achieved under an appropriate electric voltage in order to guarantee that the material remains poled and electric dipoles are arranged. The polarization of a piezoelectric material will be altered when the temperature of the material reaches the Curie temperature.

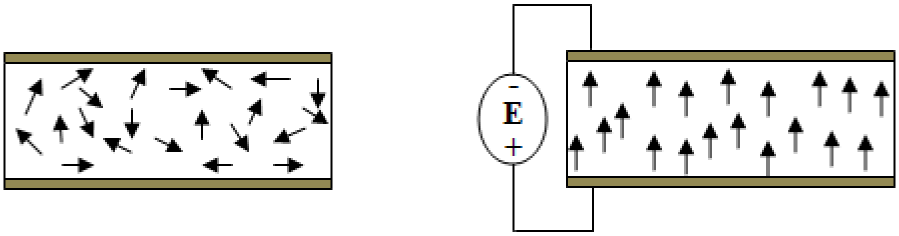

Figure 2.05: Polarization of a Ceramic Piezoelectric Material

4. Piezoelectric Constitutive Equations:

The constitutive equations of piezoelectricity represent the fundamental relations that describe the electromechanical coupling between elasticity and electricity. Mathematical relations are derived from linear field equations (Equations of motion, Gauss's, kinematic relations, Maxwell's Law) in order to model the direct and the converse piezoelectric effects. Field linear equations are as follows:

- Equations of Motion in Elasticity: $T_{ij,j} + f_i = \rho \ddot{u}_i$
- Gauss's Law in Electricity: $D_{i,i} - q = 0$
- Kinematic relations in Elasticity: $2S_{ij} = (u_{i,j} + u_{j,i})$
- Maxwell's Law: $E_i = -\phi_{,i}$

The constitutive equations in the stress-charge form are given as follows:

$$T_{ij} = c_{ijkl} S_{kl} - e_{kij} E_k$$

$$D_k = e_{kij} S_{ij} + \varepsilon_{ki} E_i$$

where: the Scalars, vectors and tensor quantities are as follows:

u_i: Mechanical Displacement (m)

ϕ : Electric Field Potential (V=J/C)

S_{ij} : Electric Field Potential (m/m)

E_i : Electric Field Potential (V/m)

T_{ij} : Stress tensor (N / m^2)

D_i : Electric Displacement (C / m^2)

f_i : Mechanical Body forces (N / m^3)

q: Electric Body Charge (C / m^3)

ρ: Mass Density (Kg/m^3)

c_{ijkl} : Elastic Material Constants (N / m^2)

e_{ij} : Piezoelectric stress constants (C / m^2)

ε_{ij} : Dielectric Constant (F/m)

Those constitutive equations can also be written the forms below:

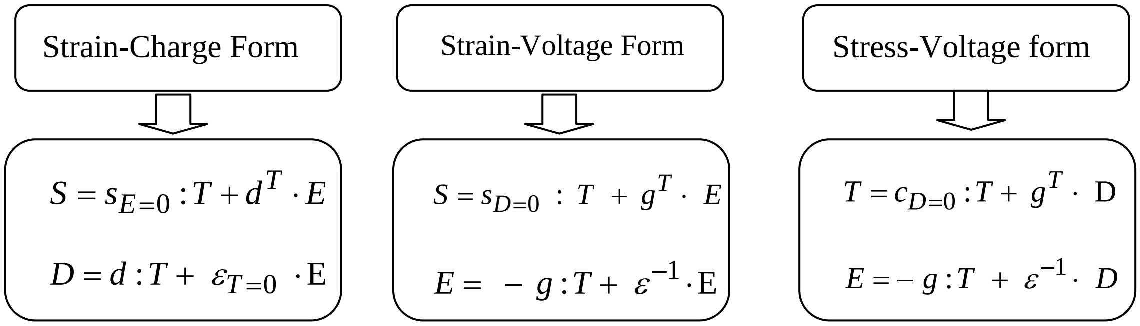

Figure 2.06: Other forms of the piezoelectric constitutive equations

s: Compliance Matrix

q: Piezoelectric Stress matrix (Stress-Voltage Form)

d: Piezoelectric Strain matrix (Strain-Voltage Form)

g: Piezoelectric Strain matrix (Strain-Voltage Form)

Table.2.01 gives a summary of the four different forms of the piezoelectric constitutive equations:

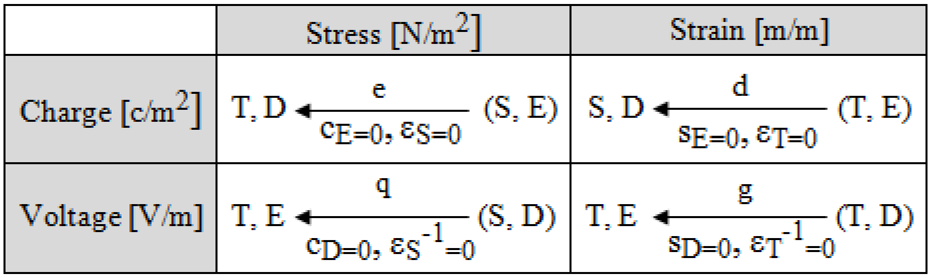

	Stress [N/m^2]	Strain [m/m]
Charge [c/m^2]	$T, D \xleftarrow[c_E=0,\ \varepsilon_S=0]{e} (S, E)$	$S, D \xleftarrow[s_E=0,\ \varepsilon_T=0]{d} (T, E)$
Voltage [V/m]	$T, E \xleftarrow[c_D=0,\ \varepsilon_S^{-1}=0]{q} (S, D)$	$T, E \xleftarrow[s_D=0,\ \varepsilon_T^{-1}=0]{g} (T, D)$

Table 2.01: Forms of piezoelectric constitutive relations

5. Electrical Impedance of a Piezoelectric Patch:

5.1. Introduction:

When an unbonded PZT patch is driven by an alternating electric voltage, a mechanical strain is produced and electrical charges are generated in the surface electrodes of the PZT. The ratio of the applied voltage to the induced current (resulting from the accumulations of electrical charges on the top and bottom electrodes) is defined as the electrical impedance of the PZT and can be measured by commercially available impedance analyzers. In this part of the thesis, a finite element model of an unbonded PZT was built using the Finite Element Multipurpose Software ANSYS and impedance data was extracted and compared to results obtained from available analytical formulation. The modeling of the unbonded piezoelectric patch can be of good utility for the understanding of the electromechanical behavior of the PZT patch and can also be useful for controlling the qualities of the patch before using it in structural health monitoring tasks.

5.2. Analytical Formulation of the Electrical Impedance of a PZT:

Giurgiutiu *et al* [16] developed the expression of the electrical impedance of a free PWAS (Piezoelectric Wafer Actuated Sensor) driven by an electrical voltage $V(t)=Ve^{iwt}$ between the top and bottom surface electrodes. The PZT is polarized in the thickness direction and its length *l*, its width *w* and its thickness *t* satisfy the condition $l >> b >> t$ by assuming uncoupled motions and hence unidirectional motion in the longitudinal direction.

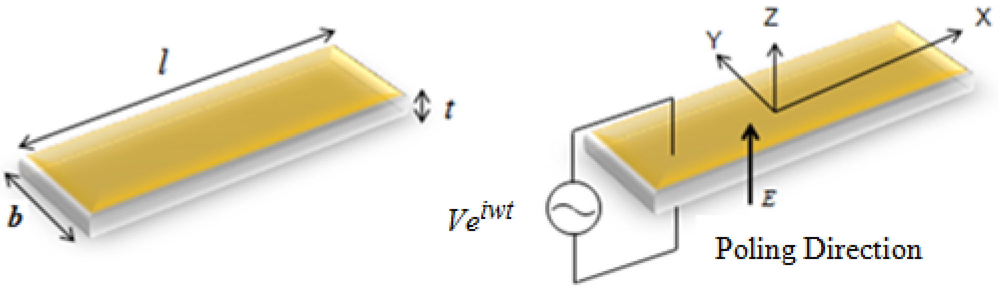

Figure 2.07: Z-polarized Piezoelectric Patch under Electric Voltage

The developed expression of the electrical impedance is given by:

$$Z = \frac{1}{jwc}\left[1-k_{31}^{2}\left(1-\frac{\tan\left(\frac{1}{2}\lambda l\right)}{\frac{1}{2}\lambda l}\right)\right]^{-1} \qquad \text{(Eq1)}$$

The above equation is obtained after developing the expression of the electrical displacement D_3, the electric charge Q and the electric current I as follows:

$$D_3 = d_{31}T_1 + \varepsilon_{33}E_3 = \frac{d_{31}}{s_{11}}\left(s_{11} - d_{31}E_3\right) + \varepsilon_{33}E_3 = \varepsilon_{33}E_3\left[1-k_{31}^{2}\left(1-\frac{u'}{d_{31}E_3}\right)\right]$$

$$Q = \int_{-l/2}^{l/2}\int_{0}^{b} D_3 dx_1 dx_2 \quad \text{and} \quad I = \frac{dQ}{dt} = iwQ$$

where: $$\frac{u'(l/2) - u'(-l/2)}{d_{31}El} = \frac{\tan(\lambda l/2)}{\lambda l/2}$$

All the parameters and their expressions are summarized in Table 2.02:

Property	Symbol	Expression
Capacitance	C	$\varepsilon_{33} \frac{l \times w}{t}$
Electromechanical Coupling Factor	k_{31}	$\frac{d_{31}}{\sqrt{s_{11}\varepsilon_{33}}}$
Wave Number	λ	$\frac{w}{c}$
Wave Speed	c	$\frac{1}{\sqrt{\rho s_{11}}}$
Dielectric constant	ε_{33}	*******
Compliance, in plane	s_{11}	*******
In plane strain coefficient	d_{31}	*******
Angular Frequency	w	*******
Density	ρ	*******

Table 2.02: Properties and expressions of the parameters used in the analytical model

5.3. Numerical Modeling of an Unbonded PZT Patch:

A coupled-field finite element analysis is conducted using the finite element code ANSYS in order to simulate the behavior of a free PZT-5A piezoelectric patch under an electrical voltage and extract appropriate data in order to plot the graph of the electrical impedance and compare the results to the analytical results obtained from the expression (Eq1). 3-D brick coupled-field finite elements are used in the analysis. These elements are eight-noded elements with six degrees of freedom in each node and an extra degree of freedom which represent the electrical DOF. In this study, we account only for the three displacements degrees of freedom X, Y and Z and the electrical degree of freedom V so we used 3-D coupled-field SOLID5 elements available in ANSYS. For each displacement degree of freedom X, Y and Z, in a SOLID5 element, corresponds a reaction force RX, RY and RZ respectively and for the electrical DOF V corresponds an electrical charge which represent the reaction force that we need to extract from ANSYS in order to plot the impedance graph. For this purpose, a harmonic coupled field analysis is performed on a PZT-5A by sweeping the frequency from 0 to 1MHz and data are collected and postprocessed. The electrical charge Q extracted from ANSYS is related to the electric impedance Z by the following expression:

$$Z = \frac{V}{I} = \frac{V}{iwQ} = \frac{V}{i2\pi f\left(\mathrm{Re}(Q) + i\,\mathrm{Im}(Q)\right)} \qquad \text{(Eq2)}$$

Where: *f*, Re (Q) and Im (Q) represent, respectively, the frequency, the real part of the electrical charge and the imaginary part of the electrical charge

The harmonic analysis was performed in a frequency range of [0, 1MHz]. Applying a voltage of magnitude 1V on the top electrode, the expression of the Impedance reduces to the following:

$$Z = \frac{1}{i2\pi f\left(\mathrm{Re}(Q) + i\,\mathrm{Im}(Q)\right)} \qquad \text{(Eq3)}$$

The frequency, the real and the imaginary parts of the electrical charge are extracted in the form of a table from the time history output of the harmonic analysis.

5.3.1. Properties of the Material:

The material used in this study is the Zirconate Titanate (PZT-5A). It has the following mechanical properties:

$$S=\begin{pmatrix}16.4 & -5.74 & -7.22 & 0 & 0 & 0\\ -5.74 & 16.4 & -7.22 & 0 & 0 & 0\\ -7.22 & -7.22 & 18.8 & 0 & 0 & 0\\ 0 & 0 & 0 & 47.5 & 0 & 0\\ 0 & 0 & 0 & 0 & 47.5 & 0\\ 0 & 0 & 0 & 0 & 0 & 44.3\end{pmatrix}\times10^{-12}\,\frac{m^2}{N};\ d=\begin{pmatrix}0 & 0 & -171\\ 0 & 0 & -171\\ 0 & 0 & 374\\ 0 & 584 & 0\\ 584 & 0 & 0\\ 0 & 0 & 0\end{pmatrix}\times10^{-12}\,\frac{C}{N}$$

where: *S* and *d* represent, respectively, the compliance matrix and the piezoelectric strain matrix. The density of the material is ρ=7500Kg/m^3. The properties of the Z-polarized PZT patch used for the analytical and numerical models are summarized in Table 2.03

Variable		Analytical model	Numerical Model
Length (mm)		20	20
Width (mm)		1	1
Thickness (mm)		0.5	0.5
Stiffness Coefficients	S_{11}	$16.4x10^{-12}$	$16.4x10^{-12}$
	S_{22}	********	$16.4x10^{-12}$
	S_{33}	********	$18.8x10^{-12}$
	S_{12}	********	$-5.74x10^{-12}$
	S_{13}	********	$-7.22x10^{-12}$
	S_{44}	********	$44.3x10^{-12}$
	S_{55}	********	$47.5x10^{-12}$
	S_{66}	********	$47.5x10^{-12}$
Coupling Coefficients	d_{13}	$-171x10^{-12}$	$-171x10^{-12}$
	d_{23}	********	$-171x10^{-12}$
	d_{33}	********	$374x10^{-12}$
	d_{42}	********	$584x10^{-12}$
	d_{51}	********	$584x10^{-12}$
Permittivity Coefficients	ε_{11}	********	$1730\ \varepsilon_0$
	ε_{22}	********	$1730\ \varepsilon_0$
	ε_{33}	$1700\ \varepsilon_0$	$1700\ \varepsilon_0$
Damping Coefficient		0	0.0001

Table 2.03: Geometrical and Mechanical properties of the analytical and numerical models

5.3.2. Geometry and Meshing of the Numerical Model:

The numerical model is built, meshed and processed using the software ANSYS (see ANSYS code in Appendix A). The body of the model was meshed into 10000 hexahedral mapped elements. Each element is a coupled-field cube of edge length 0.1mm. No boundary conditions are assigned to the model and the PZT is subjected to only a potential difference V in the thickness direction as indicated in Figure 2.07. The bottom electrode was grounded while the top electrode was subjected to a voltage which has maximum amplitude of 1V.

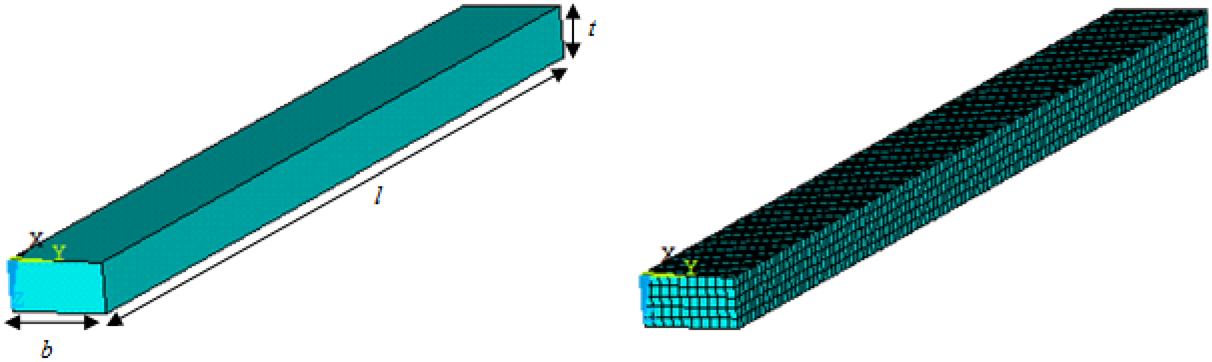

Figure 2.08: ANSYS FEM Model of the Piezoelectric Patch

5.4. Impedance Plots:

The numerical data (frequency, real and imaginary parts of the electrical charge) was extracted from ANSYS and processed using MATLAB in order to plot the graph of the impedance. The analytical formulation was also coded on MATLAB (see Matlab code in Appendix A) and appropriate mechanical properties were provided in the code in order to plot the graph of the analytical impedance. For all the geometrical and mechanical parameters summarized in Table 2.03, the plot in Figure 2.09 was obtained for both the numerical impedance and the analytical impedance.

- **Interpretation:**

The two curves have the same trend and same number of resonance and anti-resonance peaks but they present some clear differences. As depicted from the plot, the variation between the amplitude of the numerical impedance and the amplitude of the analytical impedance increases with the frequency so does the error between the resonance and anti-resonance peaks of the two curves. A first apparent reason of this variation is that the assumption of uncoupled motions of the PZT patch in the analytical formulation cannot be perfectly assumed in the numerical simulation thereby coupling cannot be totally ignored.

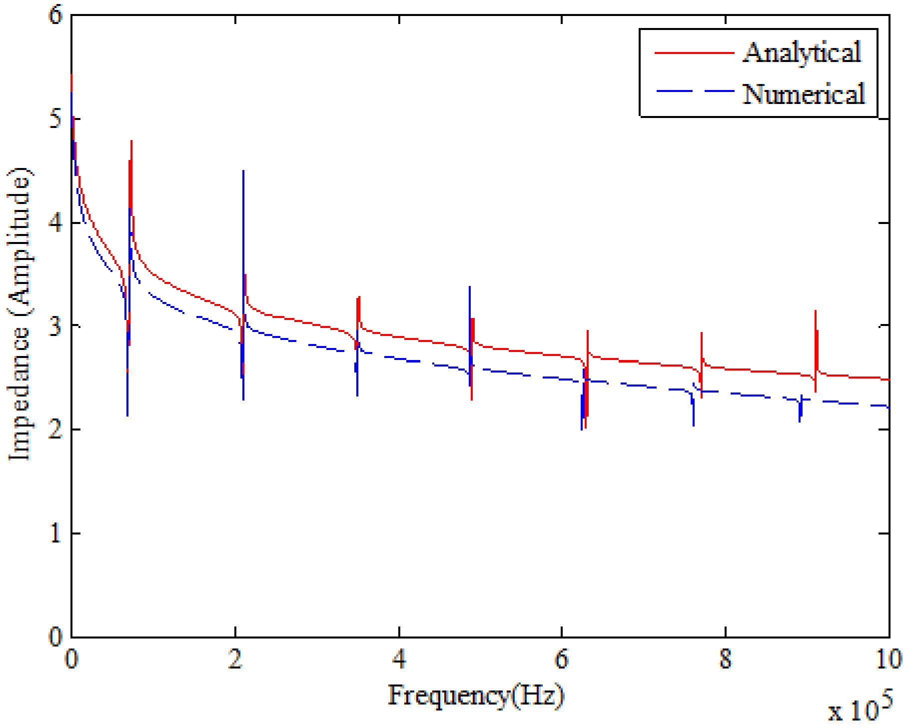

Figure 2.09: Analytical and Numerical Impedance of the Unbounded PZT Patch

5.5. Parametric Study:

In order to find other possible reasons behind the analytical and numerical variations, we run several finite element simulations using the built model in Figure 2.08 where in each simulation we vary only one parameter (except S_{11} and d_{31} which remain constant in all simulations) and keep all the other parameters unchangeable. No variations at all were made on the analytical model. The idea behind this parametric study is to study the possible variations of the numerical impedance and specify the parameters most affecting those variations. For all the simulations performed in this parametric study, the curve of the analytical result remains the same as no variation at all was applied to the analytical model.

❖ Variation of the piezoelectric strain coefficient d_{51}:

This section aims at studying the effect of variation of the coefficient d_{51} on the numerical impedance of the piezoelectric patch. For this purpose we run four different numerical simulations in which the coefficient d_{51} was increased by, respectively, 0%, 25%, 50% and 75% from its initial value while all the other parameters were kept unchanged. The variations of the coefficient d_{51} are presented in Table 2.04 as follow:

	Initial value $(d_{51})_I$	New value $(d_{51})_N$	$\alpha = \frac{(d_{51})_N - (d_{51})_I}{(d_{51})_I}$ (%)
Run 1	$584x10^{-12}$	$584x10^{-12}$	0%
Run 2	$584x10^{-12}$	$730x10^{-12}$	25%
Run 3	$584x10^{-12}$	$876x10^{-12}$	50%
Run 4	$584x10^{-12}$	$1022x10^{-12}$	75%

Table 2.04: Variation of the Coefficient d_{51}

➢ Interpretation:

Once the simulations carried out, the numerical data was extracted from ANSYS, separately, for each simulation and then processed on Matlab. The plots of the numerical results corresponding to the four different simulations are presented in Figure 2.08 along with the plot of the analytical model. It appears from the plot that the curves corresponding to the four different simulations are exactly the same with no clear variations neither on the amplitude of the impedance nor on the number and/or the frequencies of the peaks. As a result, we can conclude that the coefficient d_{51} does not have any effect on the impedance of the PZT hence it is not responsible for the errors between the numerical model and the analytical model.

❖ Variation of the piezoelectric strain coefficient d_{42}:

Similar to d_{51}, d_{42} was varied four times from its initial value with 0%, 25%, 50% and 75% respectively. Four simulations were run on ANSYS for the model in Figure 2.06 and the results showed no variations at all on the numerical impedance; neither the amplitude nor the peaks (number and frequencies) were affected. We got the exact plots of Figure 2.10. As a result, the variation of the coefficient d_{42} does not have any effect on the impedance of the PZT. Hence, the coefficient d_{42} is, like d_{51}, not responsible for the errors between the numerical and the analytical models.

❖ Variation of the compliance coefficient S_{44}:

Similar to d_{51} and d_{42}, S_{44} was varied four times from its initial value with 0%, 25%, 50% and 75% respectively. Four simulations were run on ANSYS for the model in Figure 2.08 and the results showed no variations at all on the numerical impedance, neither the amplitude nor the peaks (number and frequencies) were affected. We got the exact plots of Figure 2.10. As a result, the variation of the coefficient S_{44} does not have any effect on the impedance of the PZT.

❖ Variation of the compliance coefficient S_{55}:

Similar to d_{51}, d_{42} and S_{44}, S_{55} was varied four times from its initial value with 0%, 25%, 50% and 75% respectively. Four simulations were run on ANSYS for the model in Figure 2.08 and the results showed no variations at all on the numerical impedance, neither the amplitude nor the peaks (number and frequencies) were affected. We got the exact plots of Figure 2.10. As a result, the variation of the coefficient S_{44} does not have any effect on the impedance. Hence, the coefficient S_{55} is not responsible for the errors between the numerical and the analytical models.

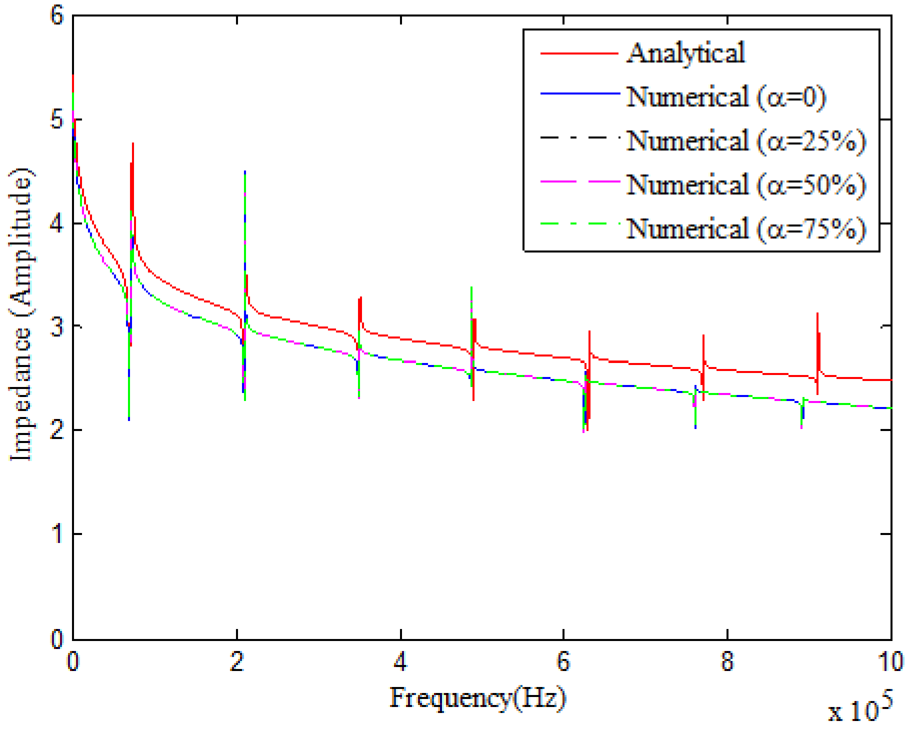

Figure 2.10: Effects of the coefficients d_{51}, d_{42}, S_{44} and S_{55} on the impedance of the PZT

❖ Variation of the piezoelectric strain coefficient d_{32}:

This section aims at studying the effect of variation of the coefficient d_{32} on the numerical impedance of the piezoelectric patch. For this purpose we run four different simulations using the model in Figure 2.08 where the initial negative value of the coefficient d_{32} was decreased by 0%, 25%, 50% and 75%. The variations are listed in Table 2.05.

	Initial value $(d_{32})_I$	New value $(d_{32})_N$	$\beta = \frac{(d_{32})_N - (d_{32})_I}{(d_{32})_I}$ (%)
Run 1	$-171\text{x}10^{-12}$	$-171\text{x}10^{-12}$	0%
Run 2	$-171\text{x}10^{-12}$	$-213.75\text{x}10^{-12}$	25%
Run 3	$-171\text{x}10^{-12}$	$-256.5\text{x}10^{-12}$	50%
Run 4	$-171\text{x}10^{-12}$	$-299.25\text{x}10^{-12}$	75%

Table 2.05: Variation of the Coefficient d_{32}

The electrical charge was extracted from ANSYS for each simulation and processed on Matlab. The plots of the numerical impedance for the four different simulations and the plot of the analytical impedance are presented in Figure 2.11.

➢ Interpretation:

Figure 2.11 shows that each of the four curves corresponding to the four numerical simulations is different from the curve of the analytical impedance both in amplitude and in frequencies of peaks of resonance and anti-resonance. However, the four curves of the numerical simulations have the same shape, same number of peaks but they present a slight difference in the amplitude of the impedance. The zoomed area shows that the amplitude of the impedance for the case of 75% is less than the impedance in the case of variation by 50% and both are less than the case of variation by 25%. So an increase in the percent variation of the coefficient d_{32} which, in fact, corresponds to a decrease in its negative initial value engenders a decrease in the amplitude of the impedance. Hence, the coefficient d_{32} has an effect on the numerical impedance of the PZT and the effect is manifested by only a decrease of the amplitude when the value of d_{32} decreases.

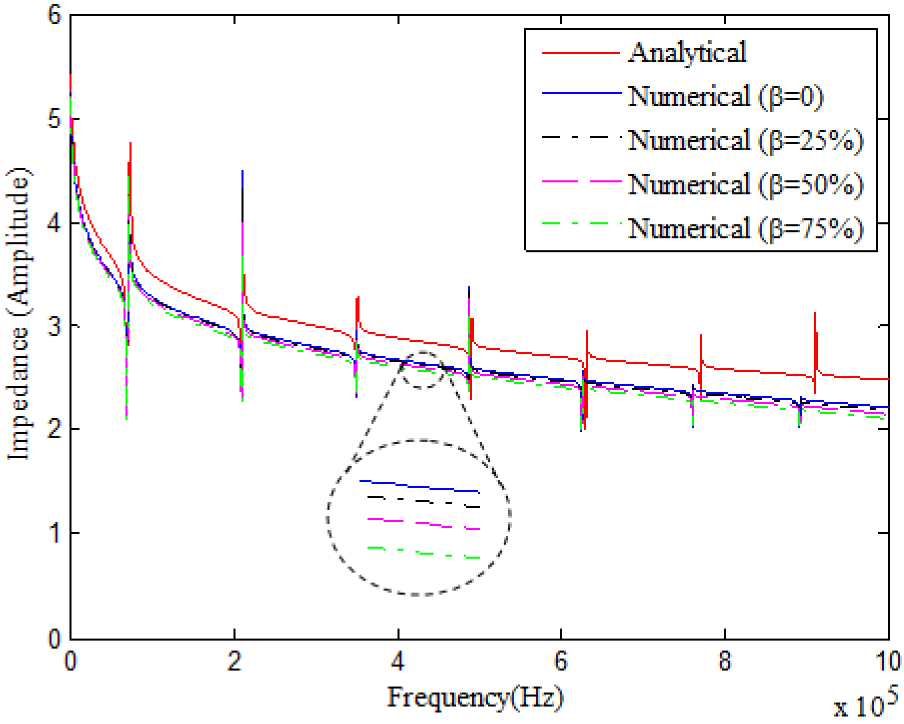

Figure 2.11: Effect of the strain coefficient d_{32} on the impedance of the PZT

❖ Variation of the piezoelectric strain coefficient d_{33}:

This section aims at studying the effect of the variation of the coefficient d_{33} on the numerical impedance of the piezoelectric patch. For this purpose we run four different numerical simulations using the FEM model in Figure 2.08 where the initial positive value of the coefficient d_{33} increased by 0%, 25%, 50% and 75%. The variations are listed in Table 2.06

	Initial value $(d_{33})_I$	New value $(d_{33})_N$	$\nu = \frac{(d_{33})_N - (d_{33})_I}{(d_{33})_I}$ (%)
Run 1	$374\text{x}10^{-12}$	$374\text{x}10^{-12}$	0%
Run 2	$374\text{x}10^{-12}$	$467.5\text{x}10^{-12}$	25%
Run 3	$374\text{x}10^{-12}$	$561\text{x}10^{-12}$	50%
Run 4	$374\text{x}10^{-12}$	$654.5\text{x}10^{-12}$	75%

Table 2.06.a: Variation of the Coefficient d_{33} (d_{33} increases)

The electrical charge was extracted from ANSYS for each simulation and processed on Matlab. The plots of the numerical impedance for the four different simulations and the plot of the analytical impedance are presented in Figure 2.12.

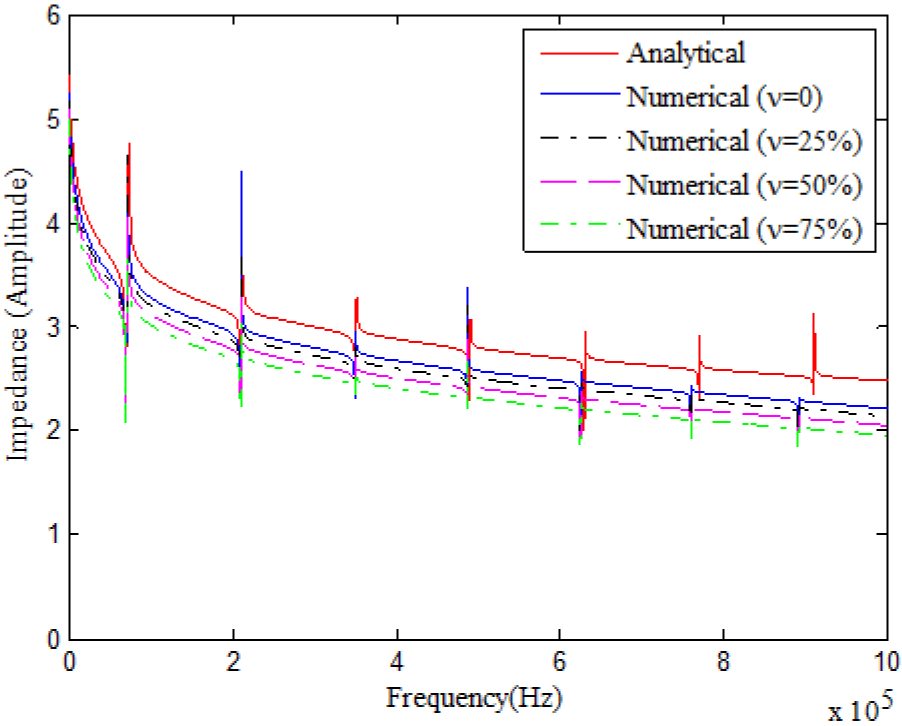

Figure 2.12.a: Effect of the coefficient d_{33} on the impedance of the PZT (d_{33} increases)

➢ Interpretation:

Figure 2.12.a shows a clear variation on the amplitude of the impedance between the four numerical curves. As shown in Table 2.06, when the percent variation on the initial value of the

coefficient d_{33} increases the value of d_{33} increases and this engenders a decrease in the amplitude of the impedance. In order to see if the error between the amplitudes of the numerical impedance and the analytical impedance reduces when we decrease the initial value of the coefficient d_{33}, we run four more runs where the initial positive value of d_{33} decreases by 25%, 50%, 75% and 100%. The variations are summarized in table

	Initial value $(d_{33})_I$	New value $(d_{33})_N$	$\nu = \frac{(d_{33})_N - (d_{33})_I}{(d_{33})_I}$ (%)
Run 1	$374x10^{-12}$	$374x10^{-12}$	0%
Run 2	$374x10^{-12}$	$280.5x10^{-12}$	-25%
Run 3	$374x10^{-12}$	$187x10^{-12}$	-50%
Run 4	$374x10^{-12}$	$93.5x10^{-12}$	-75%
Run 5	$374x10^{-12}$	0	-100%

Table 2.06.b: Variation of the Coefficient d_{33}

The plots of the different cases are presented in Figure 2.12.b.

- **Interpretation:**

From the plots of the numerical simulations for the five different runs were d_{33} was decreased by -0%, -25%, -50%, -75% and -100%, we see that the impedance first increased when a variation by 25% was applied to d_{33}, then slightly increased from the case of -25% to the case of 50% but decreased from the case of -50% to the case of -75% although remained slightly larger than the case -0%. When d_{33} was decrease by -100%, we see that the impedance further decreases and become less than the impedance in the case of no variation (0%). Runs for some other percentage variations (-60%, -55 %...) between -50% and -75% showed that the impedance does not decrease more than the case of 50% variation. No variation was recorded on the number and frequencies of the peaks.

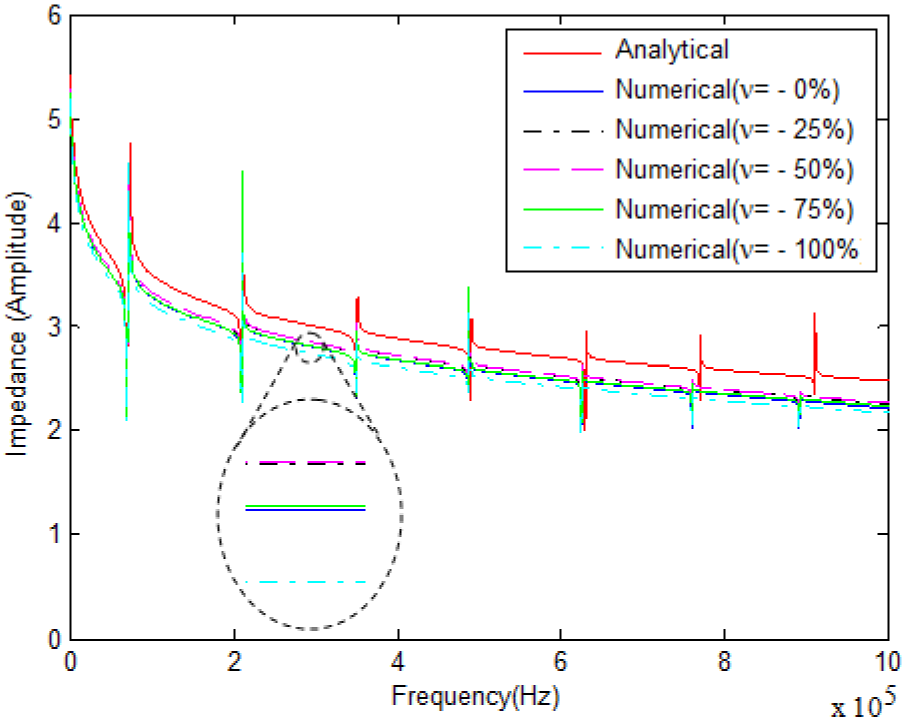

Figure 2.12.b: Effect of the coefficient d_{33} on the impedance of the PZT (d_{33} decreases)

To conclude, we can say that the coefficient d_{33} has a major effect on the numerical impedance of the PZT and the effect is manifested by only a clear variation of the amplitude.

❖ Variation of the compliance coefficient S_{12}:

This section aims at studying the effect of the variation of the coefficient S_{12} on the numerical impedance of the piezoelectric patch. For this purpose we run four different numerical simulations on the FEM model in Figure 2.08 where we decreased the initial negative value of S_{12} by 0%, 25%, 50% and 75% respectively. The variations are listed in Table 2.07.

	Initial value $(S_{12})_I$	New value $(S_{12})_N$	$\gamma = \frac{(S_{12})_N - (S_{12})_I}{(S_{12})_I}$ (%)
Run 1	$-5.74\text{x}10^{-12}$	$-5.74\text{x}10^{-12}$	0%
Run 2	$-5.74\text{x}10^{-12}$	$-7.175\text{x}10^{-12}$	25%
Run 3	$-5.74\text{x}10^{-12}$	$-8.61\text{x}10^{-12}$	50 %
Run 4	$-5.74\text{x}10^{-12}$	$-10.045\text{x}10^{-12}$	75%

Table 2.07: Variation of the Coefficient S_{12}

The plots of the numerical impedance for the four different simulations and the plot of the analytical impedance are presented in Figure 2.13

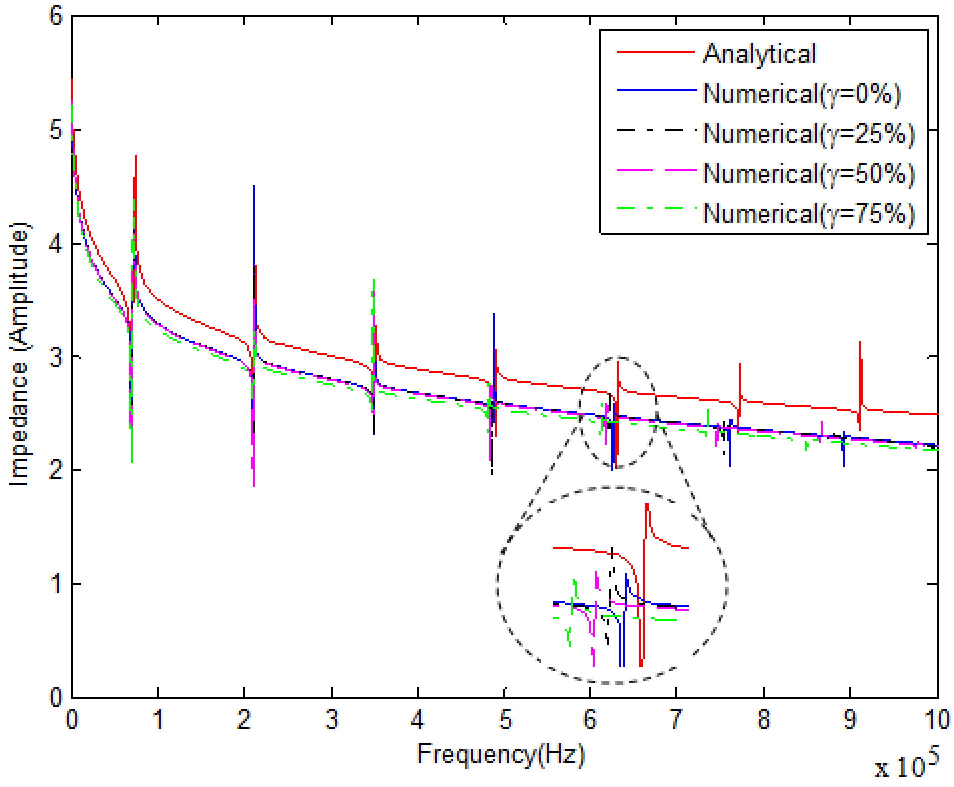

Figure 2.13: Effect of the Variation of the compliance coefficient S_{12}

➢ Interpretation:

Figure 2.13 shows that the curves of the numerical impedance, for the four cases, do not present any clear variation on the amplitude however it shows a variation on the frequencies of the peaks. In fact, the zoomed area in the plot shows that the peaks of resonance and anti-resonance are shifted more and more to the left when the value of the compliance coefficient S_{12} decreases by 25%, 50% and 75%. Hence, one way of reducing the errors between the peaks in the numerical model and the analytical model while keeping the amplitude unchangeable is by increasing the initial value of the compliance coefficient S_{12}.

❖ Variation of the compliance coefficient S_{13}:

This section aims at studying the effect of the variation of the coefficient S_{13} on the numerical impedance of the piezoelectric patch. For this purpose we chose to decrease the initial negative value of S_{13} by 0%, 25%, 50% and 75% as shown in Table 2.08. We could only run the cases of variations by 0%, 25% and 50% and collect the required data from ANSYS for each case. The case of variation by 75% could not be performed because the new value of S_{13} gave a non-positive definite compliance matrix and the finite element job aborted with error. The variations made on the coefficient S_{13} are presented in Table 2.08.

	Initial value $(S_{13})_I$	New value $(S_{13})_N$	$\xi = \frac{(S_{13})_N - (S_{13})_I}{(S_{13})_I}$ (%)
Run 1	$-7.22\text{x}10^{-12}$	$-7.22\text{x}10^{-12}$	0%
Run 2	$-7.22\text{x}10^{-12}$	$-9.025\text{x}10^{-12}$	25%
Run 3	$-7.22\text{x}10^{-12}$	$-10.83\text{x}10^{-12}$	50 %
Run 4	$-7.22\text{x}10^{-12}$	$-12.635\text{x}10^{-12}$	75%

Table 2.08: Variation of the Coefficient S_{13}

The plots of the numerical impedance for the four different simulations and the plot of the analytical impedance are presented in Figure 2.14

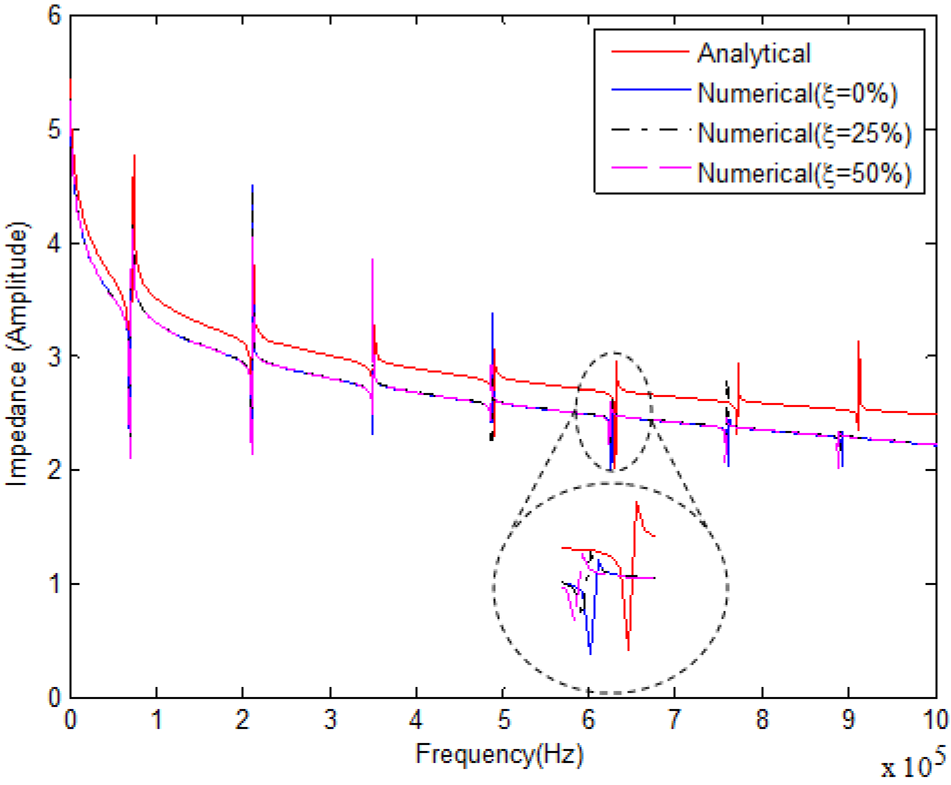

Figure 2.14: Effect of the Variation of the compliance coefficient S_{13}

➢ Interpretation:

Figure 2.14 shows that the curves of the numerical impedance for the four cases do not present any clear variation on the amplitude however it shows a variation on the frequencies of the peaks. In fact, the zoomed area in the plot shows that the peaks of resonance and anti-resonance are slightly shifted to the left when the value of the compliance coefficient S_{12} decreases by 25% and 50%. We remark that the effect of the compliance coefficient S_{13} on the numerical impedance is the same as the effect of the coefficient S_{12}. In fact, decreasing one of the two coefficients engenders a shift to the left of the peaks of resonance and anti-resonance but the effect of S_{12} is clearer than the effect of S_{13}. For both coefficients, we do not see any effect on the amplitude of the impedance.

❖ Variation of the compliance coefficient S_{23}:

This section aims at studying the effect of the variation of the coefficient S_{23} on the numerical impedance of the piezoelectric patch. For this purpose we chose to decrease the initial negative value of S_{23} by 0%, 25%, 50% and 75% as shown in Table 2.09. We could only run the cases of variations by 0%, 25% and 50% and collect the required data from ANSYS for each case. The case of variation by 75% could not be performed because the new value of S_{13} gave a non-positive definite compliance matrix and the finite element job aborted with error. The variations made on the coefficient S_{23} are presented in Table 2.09.

	Initial value $(S_{23})_I$	New value $(S_{23})_N$	$\eta = \frac{(S_{23})_N - (S_{23})_I}{(S_{23})_I}$ (%)
Run 1	-7.22×10^{-12}	-7.22×10^{-12}	0%
Run 2	-7.22×10^{-12}	-9.025×10^{-12}	25%
Run 3	-7.22×10^{-12}	-10.83×10^{-12}	50 %
Run 4	-7.22×10^{-12}	-12.635×10^{-12}	75%

Table 2.09: Variation of the Coefficient S_{23}

The plots of the numerical impedance for the four different simulations and the plot of the analytical impedance are presented in Figure 2.15.

➢ Interpretation:

Figure 2.15 shows that the curves of the numerical impedance for the four cases do not present any clear variation on the amplitude however it shows a variation on the frequencies of the peaks. In fact, the zoomed area in the plot shows that the peaks of resonance and anti-resonance are slightly shifted to the right when the value of the compliance coefficient S_{23} decreases by 25% and 50%. We remark that the effect of the compliance coefficient S_{23} on the numerical impedance is opposite to both the effects of the coefficients S_{12} and S_{13}. In fact, decreasing the coefficient S_{23} engenders a shift to the right of the peaks of resonance and anti-resonance whereas decreasing either S_{12} or S_{13} causes the peaks to shift to the left. For the three coefficients, we do not see any effect on the amplitude of the impedance.

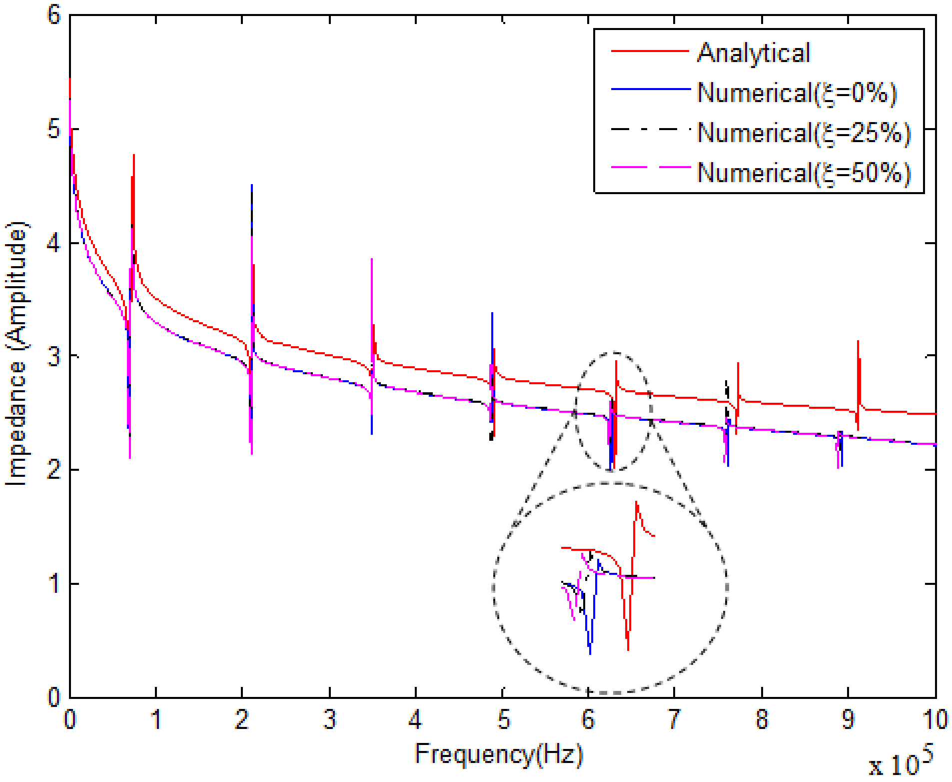

Figure 2.15: Effect of the Variation of the compliance coefficient S_{23}

❖ Variation of the compliance coefficient S_{22}:

This section aims at studying the effect of the variation of the coefficient S_{22} on the numerical impedance of the piezoelectric patch. For this purpose we run four different numerical simulations on the FEM model in Figure 2.08 where the initial positive value of the compliance coefficient S_{22} is increased by 0%, 25%, 50% and 75%. The variations on S_{22} are presented in Table 2.10.

	Initial value $(S_{22})_I$	New value $(S_{22})_N$	$\theta = \frac{(S_{22})_N - (S_{22})_I}{(S_{22})_I}$ (%)
Run 1	$16.4\ 10^{-12}$	$16.4\ 10^{-12}$	0%
Run 2	$16.4\ 10^{-12}$	$20.5\ 10^{-12}$	25%
Run 3	$16.4\ 10^{-12}$	$24.6\ 10^{-12}$	50 %
Run 4	$16.4\ 10^{-12}$	$28.7\ 10^{-12}$	75%

Table 2.10: Variation of the Coefficient S_{22}

The plots of the numerical impedance for the four different simulations and the plot of the analytical impedance are presented in Figure 2.16.

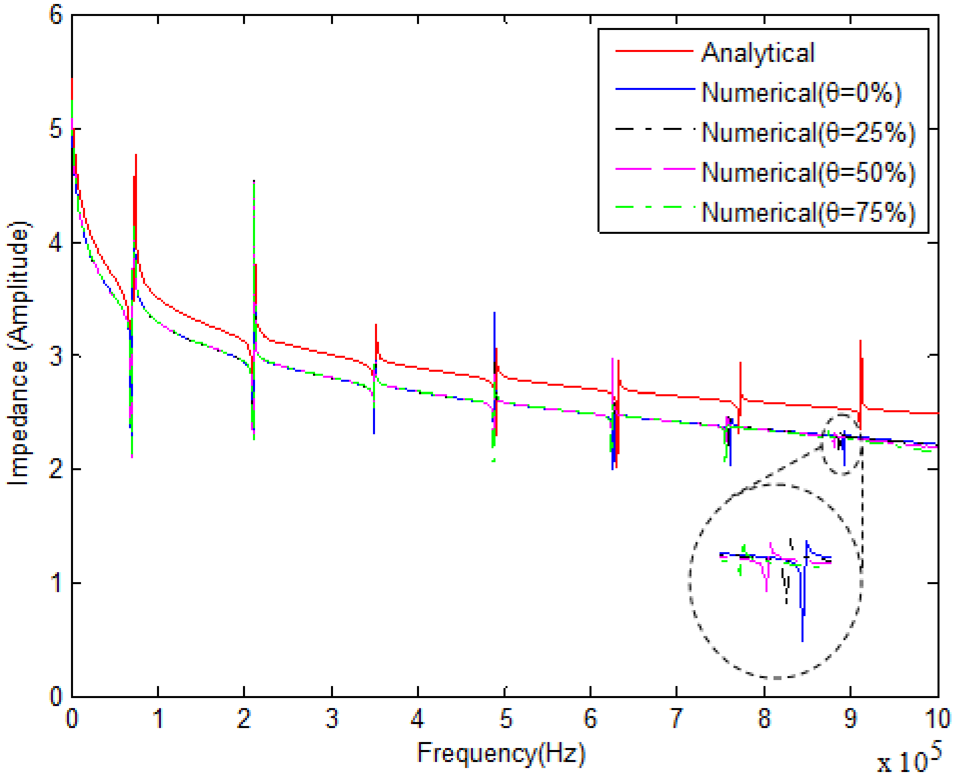

Figure 2.16: Effect of the Variation of the compliance coefficient S_{22}

➢ Interpretation:

Figure 2.16 shows that the compliance coefficient S_{22} has a very slight effect on the impedance of the PZT. We can barely see in the zoomed area a very slight shift of the peaks where the frequencies slightly decrease when the coefficient S_{22} is increased by 25%, 50% and 75%. The plot also does not show any variation on the amplitude of the impedance. To conclude, we can say that the coefficient S_{22} has a very small effect on the impedance of the PZT compared to S_{13}, S_{23} and especially to S_{12}.

❖ Variation of the compliance coefficient S_{33}:

This section aims at studying the effect of the variation of the coefficient S_{33} on the numerical impedance of the piezoelectric patch. For this purpose we run four different numerical simulations on the FEM model in Figure 2.06 where the initial positive value of the compliance coefficient is increased by 0%, 25%, 50% and 75%. The variations are summarized in Table 2.11.

	Initial value $(S_{33})_I$	New value $(S_{33})_N$	$\sigma = \frac{(S_{33})_N - (S_{33})_I}{(S_{22})_I}$ (%)
Run 1	$18.8\text{x}10^{-12}$	$18.8\text{x}10^{-12}$	0%
Run 2	$18.8\text{x}10^{-12}$	$23.5\text{x}10^{-12}$	25%
Run 3	$18.8\text{x}10^{-12}$	$28.2\text{x}10^{-12}$	50 %
Run 4	$18.8\text{x}10^{-12}$	$32.9\text{x}10^{-12}$	75%

Table 2.11: Variation of the Coefficient S_{33}

The plots of the numerical impedance for the four different simulations and the plot of the analytical impedance are presented in Figure 2.17.

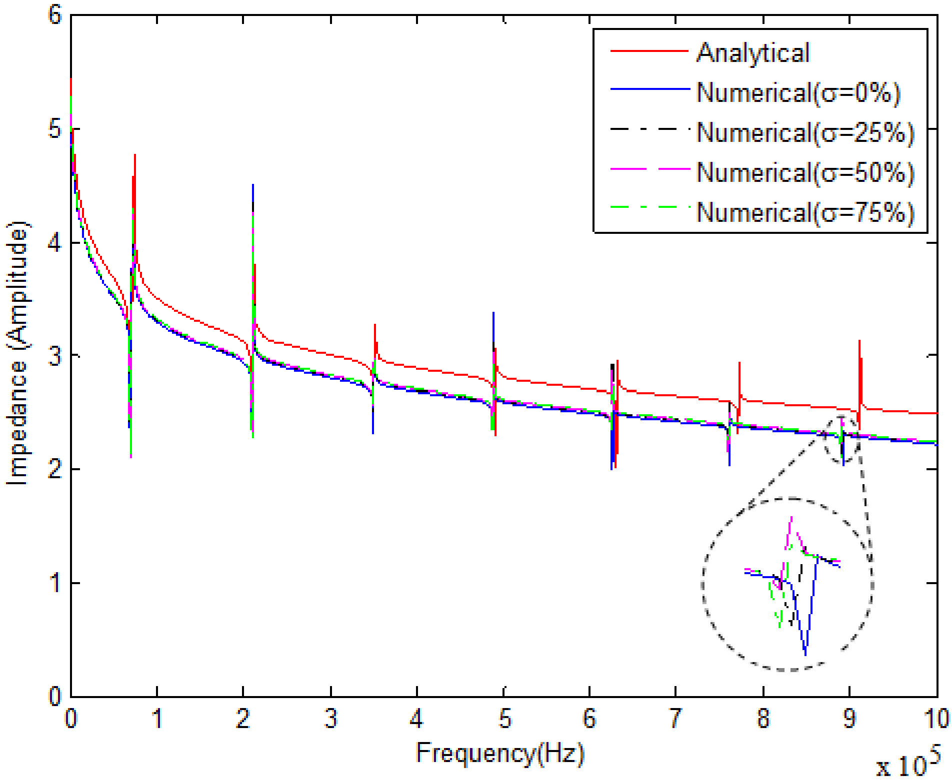

Figure 2.17: Effect of the Variation of the compliance coefficient S_{33}

➢ Interpretation:

Figure 2.17 shows that the compliance coefficient S_{33} has a very slight effect on the impedance of the PZT. Similarly as in Figure 2.16, we can barely see in the zoomed area a very slight shift of the peaks where the frequencies slightly decrease when the coefficient S_{33} is increased by 25%, 50% and 75%. The plot does not show any variation on the amplitude of the impedance. To conclude, we can say that the coefficient S_{33} has an effect on the impedance of the PZT similar to the effect of S_{22}.

❖ Variation of the damping coefficient:

This section aims at studying the effect of the damping coefficient on the numerical impedance of the piezoelectric patch. For this reason, we run three different simulations on the FEM model in Figure 2.08 where the damping coefficient ζ was given the values 0.01% in the first simulation, 1% in the second simulation and 10% in the third simulation. In the three simulations, no compliance coefficient or piezoelectric strain coefficient was varied. The data in the three simulations was also saved from the output of ANSYS in order to plot the curves of the numerical impedance for the three cases. The corresponding plots of the three simulations and the plot of the analytical impedance are presented in Figure 2.18.

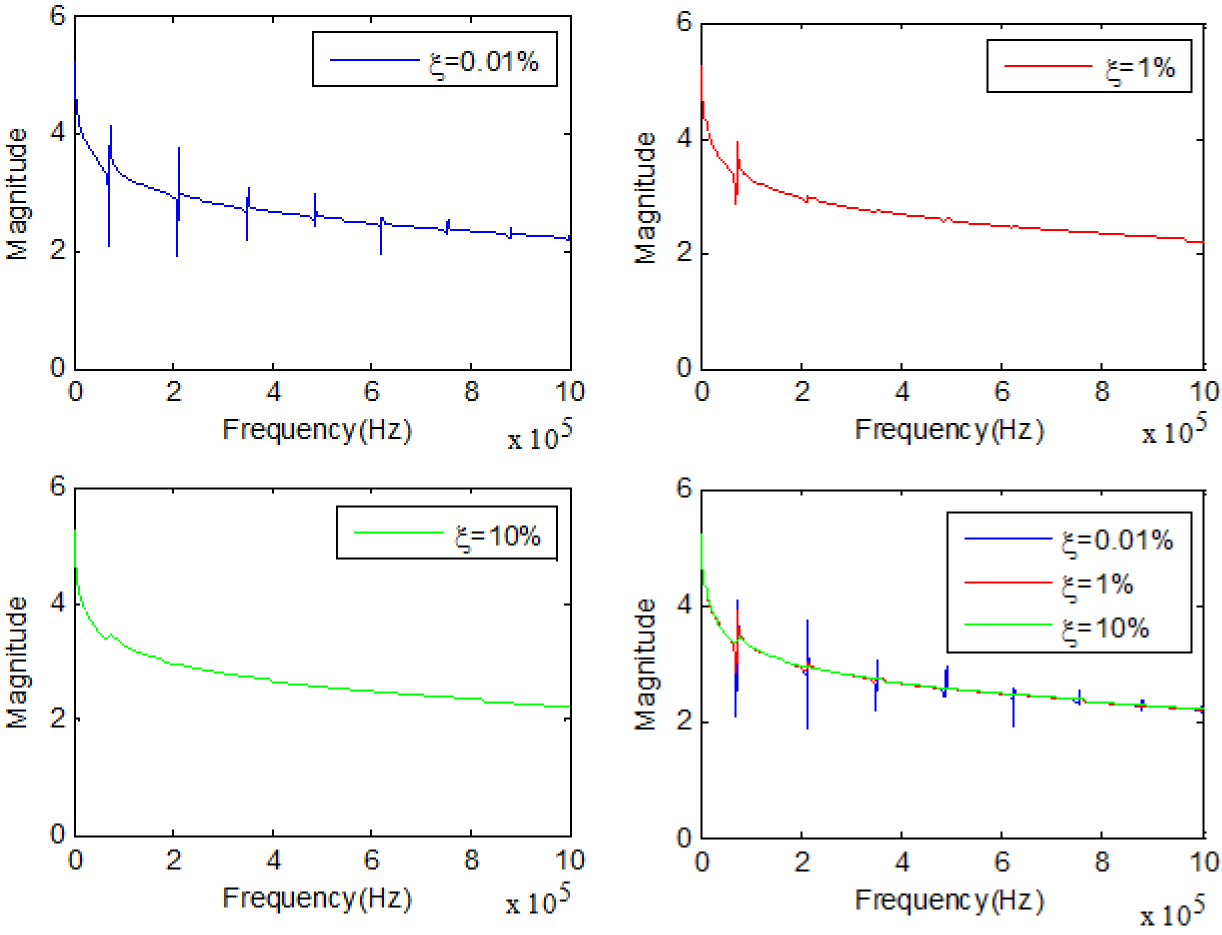

Figure 2.18: Effect of the variation of the damping coefficient ζ on the impedance of the PZT

➢ Interpretation:

Figure 2.18 shows that the number of peaks of resonance and anti-resonance decreases from the curve of the numerical impedance when the damping coefficient ζ increases. For a very light damping ζ=0.01%, we count 7 different peaks of resonance and anti-resonance. This number decreases to only two peaks when the damping coefficient ζ was increased to 1% and to only one peak when ζ was increased to 10%. So the variation of the damping coefficient has a direct effect on the number of peaks of resonance and anti-resonance but not on the amplitude of the impedance. In fact, as we can see in the fourth subplot (three cases together), the impedance curves perfectly match and no variation is recorded on the frequencies of occurrence of the peaks (this can be clearly seen for the first and second peaks). As a result, we can conclude that the variation of the damping coefficient ζ has no effect on the frequency shift between the analytical and numerical curves.

❖ Variation of the meshing module:

In this part of the work, the numerical model was tested for two different cases; case of a coarse meshing and case of a refined meshing. In both cases, the geometrical and mechanical properties of the piezoelectric patch were kept constant. A light damping ζ=0.01% was applied to the model. The two conducted simulations aim at studying the effect of the meshing module on the numerical impedance of the PZT patch. For the coarse mesh, the model was meshed into 640 cubic elements each of edge length equal to 0.25 mm however for the refined mesh, the model was meshed into 10000 cubic elements each of edge length 0.1 mm. The plots showing the impedance curves for the two cases are presented in the Figure 2.19.

➢ Interpretation:

The plots in Figure 2.19 show that both the coarse mesh and the refined gave very similar results. No major effect can be seen on the numerical impedance. We only see very small shifts on the frequencies of the peaks especially at higher frequencies. Concerning the number of peaks and the amplitude of the impedance, they were not affected by the variation of the number of elements in the model. So the refinement of the model did not have a big effect on the numerical impedance.

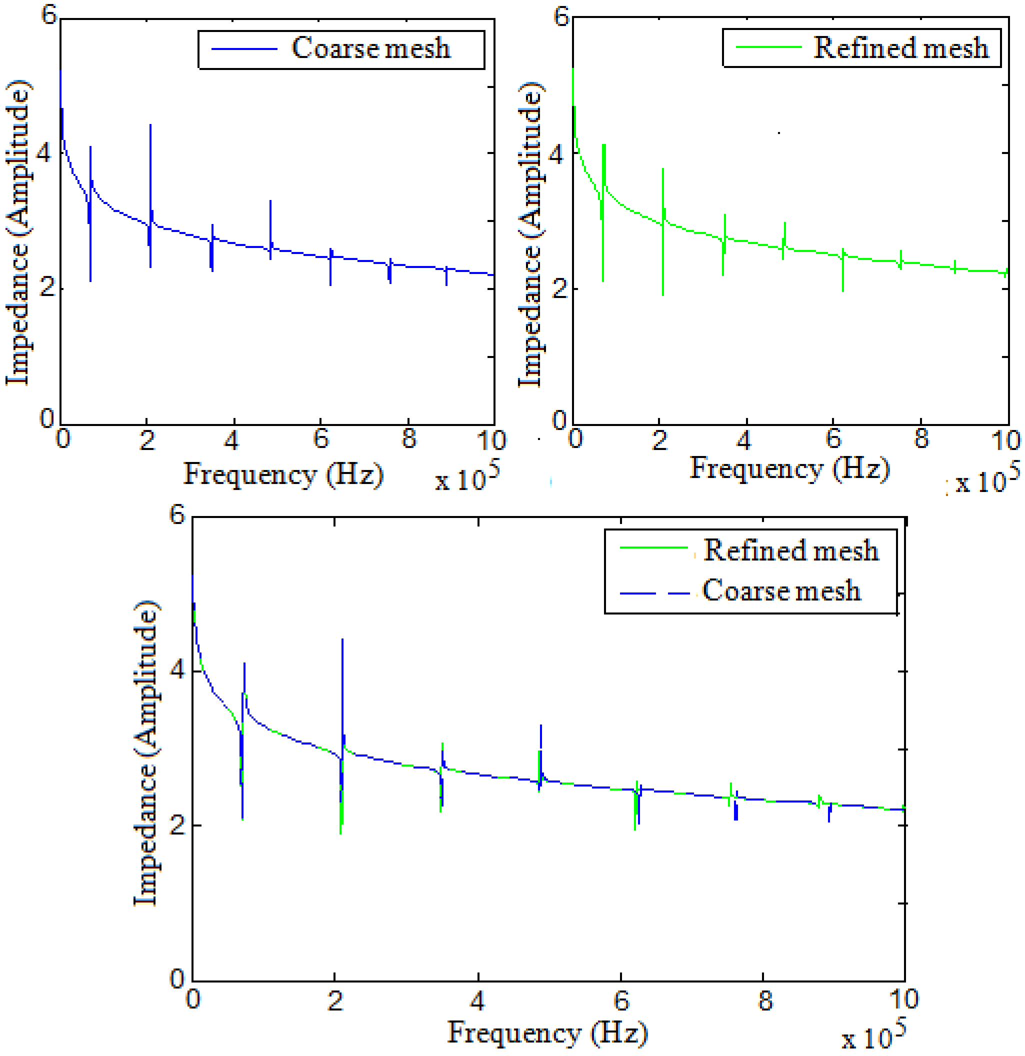

Figure 2.19: Effect of the variation of the meshing (number of elements)

❖ Summary of the parametric study.

The parametric study conducted in this work showed that many coefficients (compliance coefficients, strain coefficients, damping coefficient) have variable effects on the numerical impedance of the PZT. Some coefficients have a direct effect on the amplitude, some others affect the number of peaks and some other coefficients affect the frequencies of occurrence of the peaks. Table 2.12 gives a detailed summary of this parametric study.

Type of the effect on the impedance	Parameters	Nature
Effect only on the amplitude	d_{32}, d_{33}	Strain Coefficients
Effect only on the number of peaks	ζ	Damping Coefficient
Effect only on the frequencies of the peaks	S_{12}, S_{13}, S_{23}, S_{22},	Compliance Coefficients
No effects	d_{42}, d_{51}, S_{44}, S_{55}	Mixed

Table 2.12: Parametric Study and effects on the numerical impedance of the PZT

In order to find a best configuration that minimizes the error between the numerical impedance and the analytical impedance, we run several finite element simulations on the FEM model in Figure 2.08 where in each simulation we vary at least two different coefficients and keep the rest unchanged. The best case was obtained when we increase the strain coefficient S_{12} by 40% of the initial value and set all the strain coefficients equal to zero except d_{13} which remains constant. A light damping of 0.01% was applied to the model. The curve of the impedance for this case (Best case) is plotted with both the curve of the analytical impedance and the curve of the numerical impedance where no variations are made on all the coefficients (Initial case). The curves are presented in Figure 2.20.

We can see that the selected numerical configuration gives results very comparable to the analytical ones. In fact, the error on the amplitude between the analytical curve and the new numerical curve (green) reduced considerably and the peaks of both curves have now almost the same frequencies and no shifts can be seen even at higher frequencies.

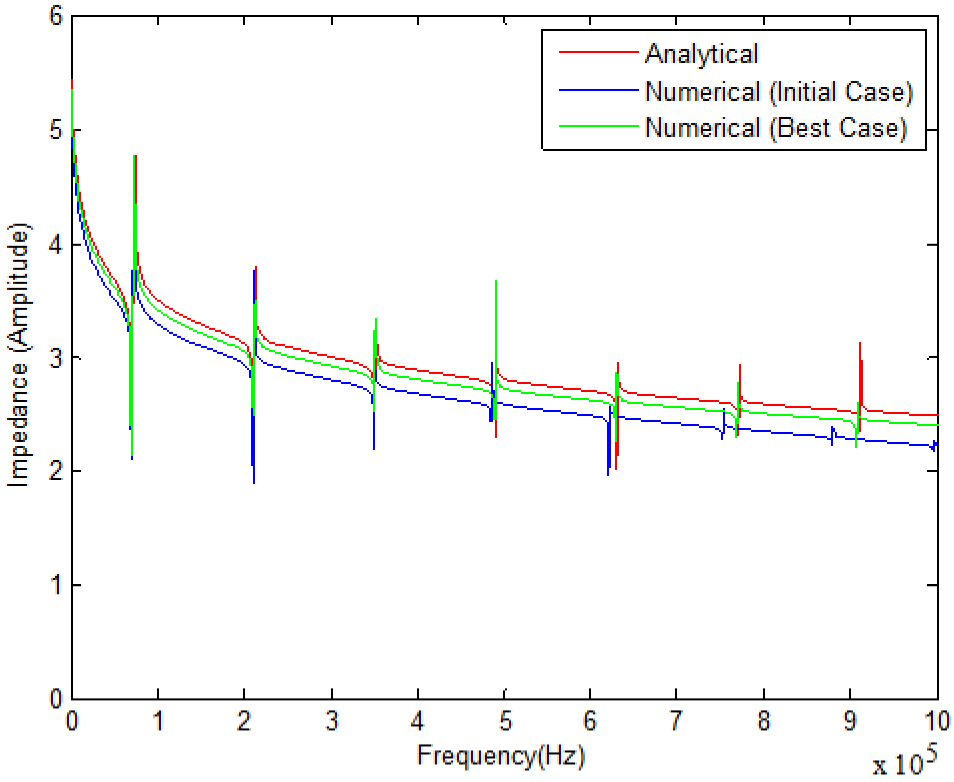

Figure 2.20: Reduction of the error between the analytical and numerical results

Conclusion:

This work was conducted in order to study the electrical impedance of an unbounded piezoelectric patch driven by a constant electric voltage applied on its surface electrodes. Two models are proposed and compared in this study; an analytical model found in the literature for which the displacement motions are assumed uncoupled and the piezoelectric patch was supposed to experience a one dimensional motion along its length and a numerical model built using the finite element software ANSYS. The two models have the same mechanical and geometrical characteristics. The comparison between the curves of impedance of the two models shows clear errors. A parametric study was conducted in order to see the causes of those errors. It is found that the compliance coefficients affect the impedance by shifting the peaks of resonance and anti-resonance and that the piezoelectric strain coefficients have a direct effect on the amplitude of the impedance. Those interpretations were successfully used to find a better configuration where the error between the analytical model and the numerical model reduced considerably.

Chapter 3

Lamb Waves: General Overview

1. Introduction to Lamb Waves:

Waves are disturbances (perturbations) that propagate through or on the surfaces of material media (solid, liquid, and gas) at variable speeds functions of the elastic and internal properties of the media. They represent ideal means of transportation of the information which made them at the center of preoccupation of many researchers.

Waves are classified into different categories based on their natures, their origins and their modes of propagation in elastic media. We distinguish:

1.1. Elastic Waves in Solids and Structures:

- **Longitudinal Waves:**

Represent a common type of elastic waves that can propagate through solids, liquids and gases. They are called longitudinal waves because they induce vibration of particles in the direction of propagation. Those waves are also known as P-waves which stand for primary waves (fastest to be recorded) or for pressure waves (result from an alternation of compressions and rarefactions).

The velocity of P-waves in elastic homogeneous solid media is given by:

$c_p = \sqrt{\frac{\lambda + 2\mu}{\rho}}$. For a 3-dimentionnal free solid media

$c_p = \sqrt{\frac{1}{1-v^2}\frac{E}{\rho}}$. For a 2-dimentionnal plate with free top and bottom surfaces

$c_p = \sqrt{\frac{E}{\rho}}$. For a 1-dimentionnal slender bar

$$\left.\begin{aligned} \lambda &= \frac{vE}{(1-2v)(1+v)} \\ \mu &= \frac{E}{2(1+v)} \end{aligned}\right\}: \text{ Lamé constants} \qquad \begin{cases} E: \text{Young`s Modulus} \\ v: \text{ Poisson`s ratio} \\ \rho: \text{ Density} \end{cases}$$

- **Shear Waves:**

Represent another common type of elastic waves. A shear wave, or also S-wave, occurs in an elastic medium when it is subjected to a periodic shear and results in alternating transverse motion of particles (displacement of particles is perpendicular to the direction of propagation of the wave). The velocity of s-waves in elastic homogeneous solid media is given by:

$$c_s = \sqrt{\frac{\mu}{\rho}}$$

- **Flexural Waves:**

Flexural waves are deformations that propagate in bars and in flat or curved plates due to the presence of bending actions. On their propagations, flexural waves subject the bar or plate to vibrational movements that induce a motion perpendicular to the axis of the bar or to the plane of the plate. The speed of flexural waves in a simple beam is given by:

$$c_F = \sqrt{w\left(\frac{h}{2}\sqrt{\frac{E}{3\rho}}\right)}$$

where:

$w=2\pi f$: angular frequency and h: height of the beam

The expression above shows a dependence of the velocity of the flexural wave on the frequency of vibration of the beam. This property is inherent for flexural waves and is known as Dispersion.

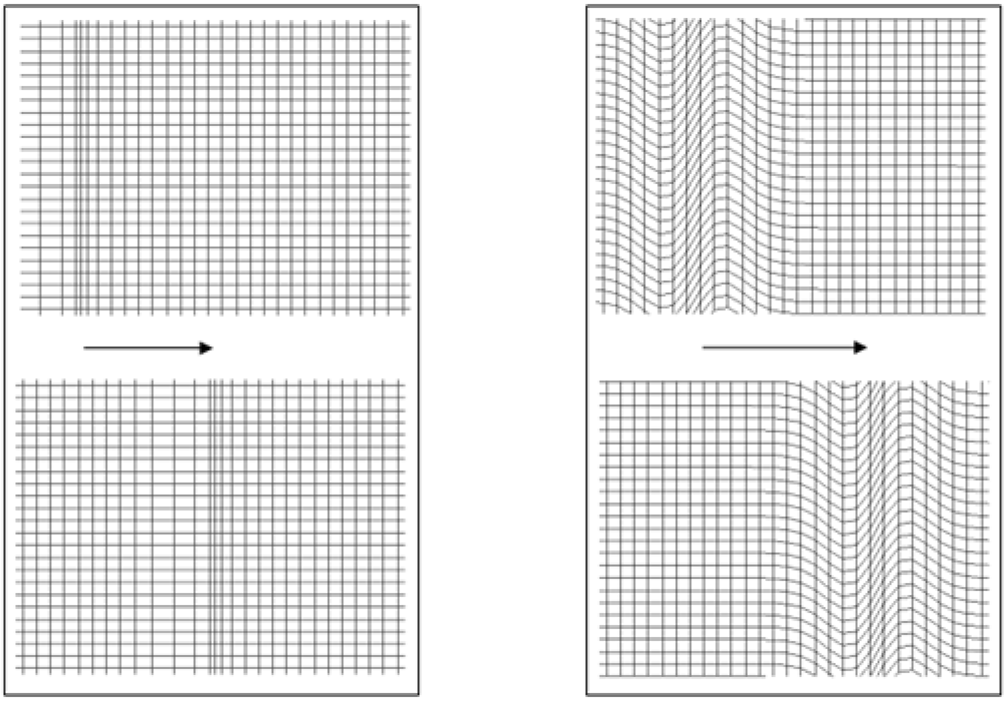

(a) Longitudinal waves,

(b) Shear waves

Figure 3.01: Propagation of (a) Longitudinal waves, (b) Shear waves

❖ Rayleigh Waves:

Rayleigh waves are a common type of surface waves. They propagate near the surface of a solid media and result in elliptical motions of the particles in a vertical plane parallel to the direction of propagation. The existence of these waves was predicted by John William Strutt (Lord Rayleigh) in 1885. The amplitude of vibration decreases with an increase in the thickness of the media.

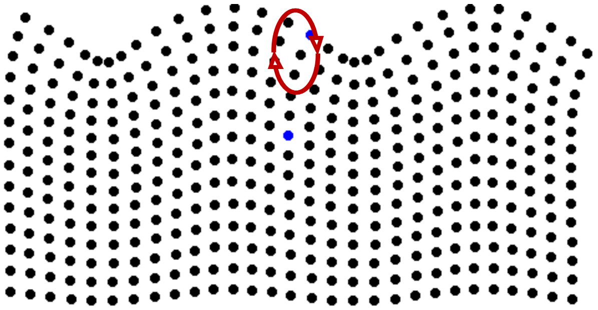

Figure 3.02: Propagation of Rayleigh waves.

2. Lamb Waves:

2.1. Historical Overview:

Lamb waves are elastic perturbations capable of propagating relatively long distances in solid plates and laminated structures. They are also known as guided plate waves because they remain guided between two free parallel surfaces. Horace Lamb [30] presented, in an outstanding paper, his work on elastic waves. He was the first one to formulate the dispersion equations of waves propagating in elastic infinite plates. In homage to his person, those waves are now called “Lamb waves”. Since then, many researchers have showed a big endeavor for studying these particularly important elastic waves and great contributions have been achieved leading to very promising technologies. Lamb waves have several enabling capabilities which made them, in an early stage, a hub in both research and applications. One among the earliest uses of lamb waves was to verify the homogeneity of materials. Researchers realized later the sensitivity of lamb waves to the presence of damages in structures and components and started to use them for the detection of possible flaws and cracks. Worlton [55] conducted the first ultrasonic testing using lamb waves in order to investigate on the presence of possible damages in a surface. He used two transducers, one as actuator and the other as receiver. Worlton used the hypothesis of infinite surface because the formulation of lamb waves for semi-infinite and finite plates were not developed yet at that time. It was until a decade later when such an assumption was proposed by Torvik [49] who paved the way for other researchers interested in lamb waves to study the reflection from boundaries and the conversion of modes.

The massive amount of research devoted to the understanding of the behavior of lamb waves when propagating in elastic media has led to prominent and reliable inspection techniques. Their use in engineering applications has been growing considerably, especially in the area of structural health monitoring. A Main reason is that their propagation in damaged structures is altered by the presence of defects (attenuation of the amplitude, reflection from the defect…). By analyzing the output signals and comparing them to baseline data, one can locate, qualify and quantify all the flaws and imperfections (disbands, corrosion, fatigue cracks, misalignment, delaminations, etc.) in any structure to evaluate re. Another important reason is that the use of lamb waves will not subject the structure to any harm and the evaluation is totally nondestructive. Many other reasons also made from lamb waves an ideal tool in structural health monitoring.

2.2. Theoretical Backgrounds:

2.2.1. Governing Equation:

A fundamental grasp of the theory of lamb waves and their basics is given here in order to achieve better understanding of their concepts and their fundamental characteristics (frequency, wave speed, wavelength, etc.) and to, later, ease the interpretation of experimental and numerical results. Historical drafts show that, the English mathematician Horace Lamb was the first researcher who developed the equations for the dispersion of elastic waves in elastic media.

After Sir Lamb`s outstanding breakthrough, the theory of lamb waves has been extensively studied and completely documented in several scientific references (journals, books, etc.).

Lamb wave can be described in terms of two scalar potentials ϕ and ψ. The potentials satisfy the wave equation as follows:

$$\begin{cases} \dfrac{\partial^2\phi}{\partial x^2}+\dfrac{\partial^2\phi}{\partial y^2}=\dfrac{1}{c_p^2}\dfrac{\partial^2\phi}{\partial t^2} \\ \dfrac{\partial^2\psi}{\partial x^2}+\dfrac{\partial^2\psi}{\partial y^2}=\dfrac{1}{c_p^2}\dfrac{\partial^2\psi}{\partial t^2} \end{cases} \quad \text{where: } \begin{cases} c_p^2=\dfrac{\lambda+2\mu}{\rho} \\ c_s^2=\dfrac{\mu}{\rho} \end{cases}$$

The propagation of lamb waves in an isotropic and homogeneous plate assumes the general governing equation (Eq. 3.1) ([Su and Ye] [48]).

$$\frac{\tan(qd)}{\tan(pd)}=\frac{4k^2pq\mu}{\left(\lambda k^2+\lambda p^2+2\mu p^2\right)\left(k^2-q^2\right)}=0 \qquad \text{Eq 3.1}$$

Where: $$p^2=\frac{w^2}{c_p^2}-k^2\ ;\ q^2=\frac{w^2}{c_s^2}-k^2$$

λ, k, w, c_L and c_T represent respectively the wavelength, the wavenumber, the angular frequency, the longitudinal and the shears wave velocities.

The equation above equation describes the motion of the particles in the elastic media due to perturbations caused by the input waveform (elastic displacement). The restoring forces between particles (Han *et al*) [25] will cause the wave to propagate through the whole media. Lamb waves propagate in different modes which are classified based on the arrangement of the general governing equation. This equation is split into two sub-equations: one equation describes the motion of particles in symmetric modes and the other describes their motion in antisymmetric modes.

2.2.2. Symmetric Modes:

Symmetric modes are designated S0, S1, S2, etc., they propagate through the thickness in a symmetrical way about the median plane of the structure as illustrated in Figure 3.03.

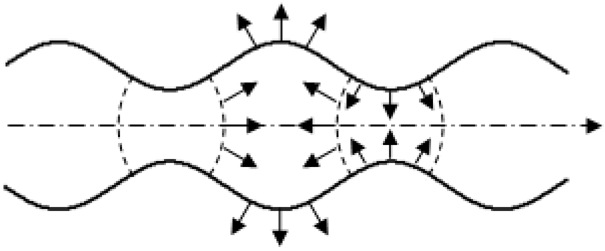

Figure 3.03: Schematic of Lamb wave propagation in symmetric mode

The equation that governs the motion of particles in symmetric modes is given by:

$$\frac{\tan(qh)}{\tan(ph)} = -\frac{\left(k^2 - q^2\right)}{4k^2 pq}$$

2.2.3. Antisymmetric Modes:

Antisymmetric modes are designated A0, A1, A2, etc., they propagate through the thickness but in an asymmetrical way about the median plane of the structure as shown in Figure 3.04

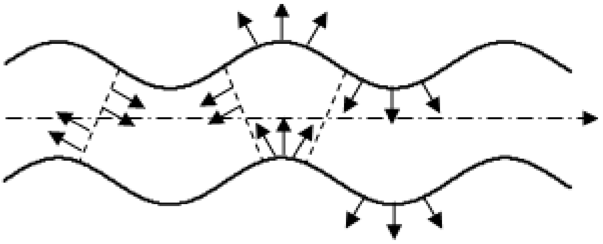

Figure 3.04: Schematic of Lamb wave propagation in antisymmetric mode

The equation that governs the motion of particles in antisymmetric modes is given by:

$$\frac{\tan(qh)}{\tan(ph)} = -\frac{4k^2 pq}{\left(k^2 - q^2\right)}$$

During propagation, lamb waves are subjected to various parametrical modifications (changes in direction due to reflection from boundaries and cracks, attenuation in amplitudes, etc.), such modifications are not very important in the wave analysis and are easy to interpret. Lamb waves are also known to be dispersive waves: the speed of the wave depends on the input frequency as well as the on the thickness of the elastic medium the wave propagates through.

2.2.4. Dispersion of Lamb waves:

In digital signal processing, any signal that can be represented as time-varying amplitude has an equivalent frequency spectrum in the frequency domain. The signal in Figure 3.05 (a) represents the shape of a Morlet wave in the time domain, its corresponding frequency spectrum shown in Figure 3.05 (b) was obtained using the technique of Fast Fourier Transform.

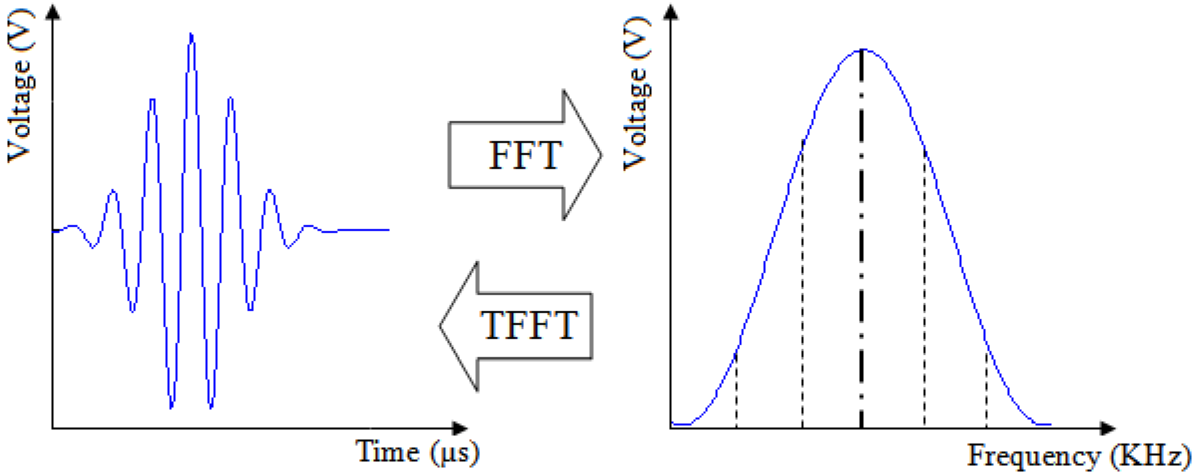

Figure 3.05: Presentation of a Morlet wave in the time and frequency domains

It shows that the wave is made of a central frequency with many side frequencies. If each frequency propagates at the same constant velocity when the wave propagates through an elastic medium, the medium is non-dispersive and the propagation of the wave is non-dispersive which means that the wave is not subjected to any deformation. However, when each frequency propagates at a different velocity when the wave propagates in an elastic medium, the elastic medium is dispersive and the propagation of the wave is dispersive which means that the wave is subjected to deformation while propagating. This phenomenon is called dispersion.

Almost all waves in nature are dispersive (light, sound, sea waves, etc.). Lamb waves are also very dispersive; they propagate in elastic media with different velocities. The wave speed depends on the frequency as well as on the thickness of the medium the wave propagates through. Such dependence can be seen in plots called dispersion curves which represent, for both symmetric and antisymmetric modes, the variation of the phase and group velocities as function of the product of the frequency of vibration times the thickness of the structure on which lamb waves are to be actuated. As we can see from the dispersion curves for both symmetric modes (Figure 3.06) and antisymmetric modes (Figure 3.07), an increase either on the frequency of vibration or on the thickness of the elastic medium will result in an increase on the number of excited modes. Usually, it is advisable to pick a range of frequencies and a range of thicknesses for which only the two fundamental modes S0 and A0 are excited, this helps considerably the interpretation of output signals. If more modes are considered, the analysis of output signals will be cumbersome and more complicated as modes can overlap easily, can be converted and can generate new different modes when interacting with defects, etc.).

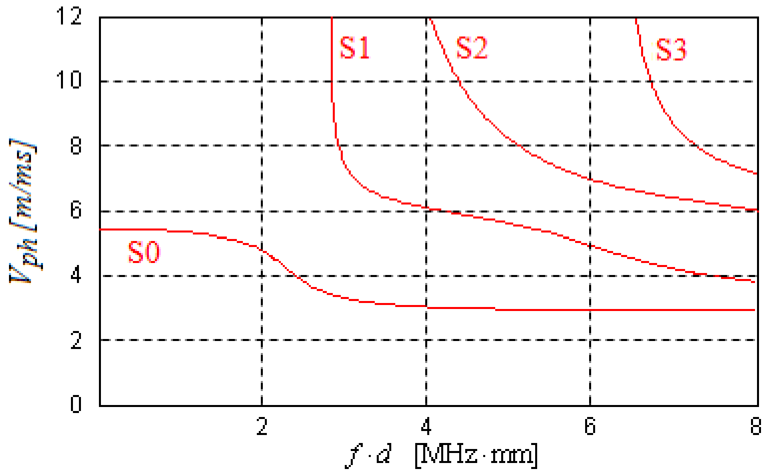

Figure 3.06: Phase velocity in aluminum plates for symmetric lamb wave modes

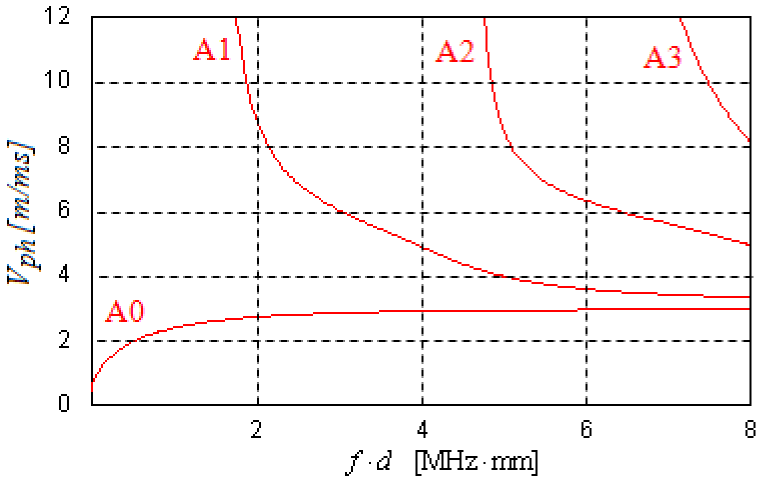

Figure 3.07: Phase velocity in aluminum plates for antisymmetric lamb wave modes

2.3. Lamb waves in Structural Health Monitoring:

Lamb waves have received great attention since they were discovered and have been extensively used in several engineering and industrial applications. In structural health monitoring, lamb waves have gained a special interest as good alternative for techniques that rely on conventional ultrasonic transducers. In fact, compared to conventional techniques which are tedious and time-consuming, use of lamb waves has reduced considerably the time of inspection of structures by offering the advantage of scanning very large surfaces in very short times and the ability to scan curved, hidden and hard to reach areas. Due to these enabling capabilities, lamb waves have been used for detection of all kinds of damages (cracks, delaminations, corrosion, etc.). Alleyne and Cawley (1990 [01], 1991 [02], and 1992 [03]) used conjointly the 2-dimensional Fourier transform and the finite element method in order to study the interaction of lamb waves with simulated damages. They showed that the sensitivity of lamb waves to the presence of notches depends on many factors such as the thickness frequency product and the geometry of the notch. Guo et al. [24] studied the interaction of the fundamental symmetric mode S0 with a horizontal delamination in a composite material. Lowe *et al* [35], [36] studied the behavior of the lamb wave mode A_0 in the presence of notches of different lengths and depths and in the presence of vertical cracks. Later Lowe and Diligent [37] studied the case of S0. These studies paved the way for research on the two fundamental modes. Many researchers used different other numerical techniques (Finite difference, Boundary Element method, etc.) in order to characterize the behavior of lamb waves when interacting with different types of damages in different structures. Grondel [23] contributed to the optimization of inspection techniques based on lamb wave base for structural health monitoring of aircrafts. Bourasseau [08] studied the propagation of lamb waves in sandwich structures. Tua *et al* [50] proposed a comprehensive method based on the time of flight in order to locate and determine linear cracks on homogeneous aluminum plates. They showed that the method which consists on sweeping systematically a square grid of PZT transducers and analyzing recorded signals based on times of flight is good in detecting linear cracks and ascertain their locations.

3. Conclusion:

In this chapter, focus was placed on the presentation, description and understanding of the theory of lamb waves. An in-depths review about the history, the formulations and the use of lamb waves as an efficient tool for the assessment of several structures in, both, engineering and industrial fields was also given. It appears through the literature review presented that the lamb waves have been gaining much interest due to the capabilities they present in the technological developments of new reliable techniques for nondestructive inspection.

Chapter 4

Damage Detection in Aluminum plates

1. Introduction:

Plates and plate-like structures are extensively used in all fields of engineering because of the distinct advantages they present (high load-carrying capacities, light weights, effectiveness in structural engineering, reduced prices, etc.). They are used in aircrafts, missiles, machines, civil infrastructures (bridges, pavements, hydraulic structures, buildings, etc.). Due to the importance of such structures, full inspection of plates and plate like structures before use (following manufacturing process) and during use (under normal working conditions) is a necessity in order to avoid any detrimental damages due to failure of one or more parts. For this reason, many inspection techniques have been used in order to detect all possible forms of damages in plates (cracks, delaminations, disband, etc.). Shang *et al* [46] used the technique of double-exposure holography for the inspection and assessment of plates containing locally thinned regions as artificial defects. Kannappan *et al* [27] developed an analytical solution based on the variation of natural frequencies in order to detect and characterize damage in simply supported plates. They used values of stored strain energies computed from the deformed mode shapes in order to locate and characterize the damage. Many other schemes have been used for the characterization of damages in plates and plate-like structures.

During the last two decades, inspection schemes based on structural health monitoring have been extensively adopted for the detection of damages in plates and plate like structures. Ultrasonic techniques (pitch-catch, pulse-echo, time reversal, etc.) based on the use of piezoelectric actuated lamb waves have been among the leading ones. In this work, a brief description of the concept of pulse-echo and the concept of pitch catch will be presented and attention will be specifically given to technique of pitch-catch. Analysis of experiments conducted on aluminum plates using piezoelectric mounted transducers will be discussed in depth.

2. Ultrasonic Health Monitoring Techniques:

2.1. Pulse-Echo Technique:

The pulse-echo is an ultrasonic nondestructive technique that involves the use of one transducer as pulser/receiver to actuate signals through a medium and sense reflected signals in order to detect flaws and cracks in simple and composite structures. The concept is straightforward: a high frequency sound is actuated into a medium to evaluate, which generates a wave that propagates through the material. When the wave interacts with a discontinuity, a part of the energy will reflect back from the surface of the discontinuity. The receiver detects the reflected energy and transforms it to an electric signal that can be analyzed in order to detect damages.

2.2. Pitch-Catch Technique:

The pitch catch technique is an ultrasonic method that involves a set-up of a transmitter and receiver located in the same side of the structure within a distance from each others. This technique has been widely used to detect many types of defects (delaminations, inclusions, in-homogeneities, flaws, etc.). It is based on a simple concept; waves actuated by the transmitter propagate through the material at a velocity c and reach the receiver after traveling for a time t=d/c, known as the time of flight. Reflections from the boundaries and from defects will also reflect back and reach the receiver at different times. Many researchers used the pitch-catch configuration for several purposes. Bar-Cohen *et al* [07] used leaky Lamb waves in a pitch-catch arrangement in order to detect and characterize flaws and defects in a composite material. Park *et al* [43] introduced a sensor network system using four pairs of sensors in a pitch catch configuration in order to identify possible cracks in a welded zone of a steel truss member. They focused on the generation of the fundamental mode A0.

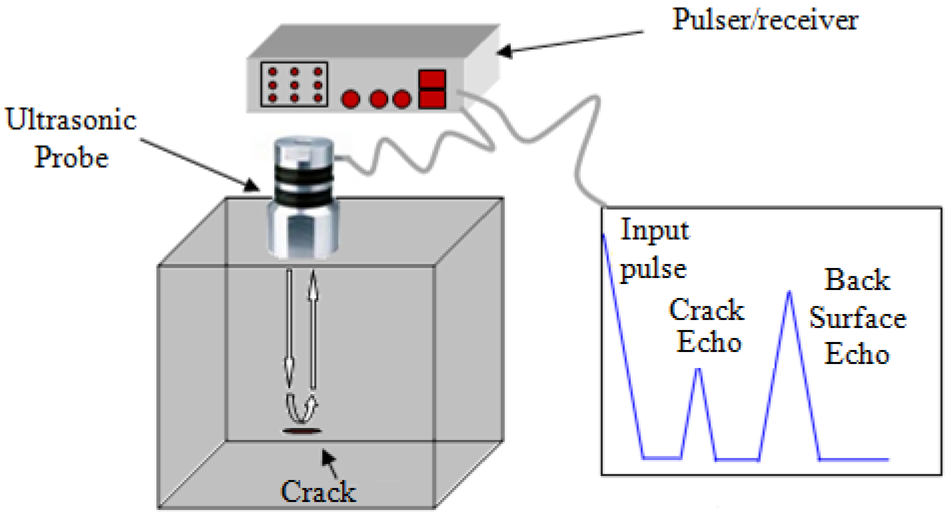

Figure 4.01: Schematics of the pulse-echo technique

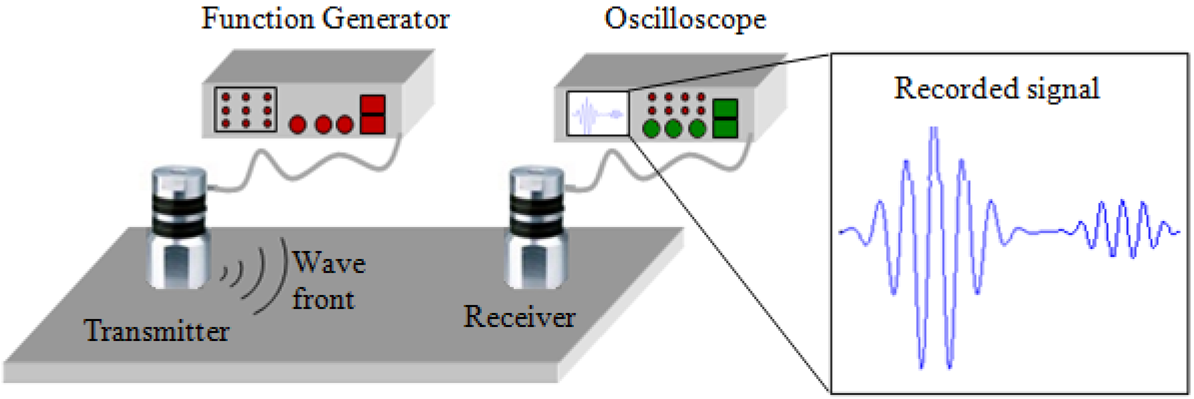

Figure 4.02: Schematics of the pitch-catch technique

3. Ultrasonic Health Monitoring of Finite Aluminum Plates:

This part of the chapter details experiments carried in the nondestructive testing lab at Michigan State University for the health monitoring of finite aluminum plates. Assessment was based on the technique of pitch catch with surface-mounted lead zirconate titanate (PZT) piezoelectric wafers. All the experiments conducted involved the use of the following equipments:

1. Arbitrary Function Generator
2. Digital Oscilloscope
3. Computer
4. Piezoelectric patches
5. Aluminum plate
6. Permabond 910

In each experiment, the aluminum plate was cleaned and then mounted on a table. Second, piezoelectric patches were cut to custom dimensions and then bonded to the surface of the plate in predefined configurations. Third, an input signal, with appropriate shape, frequency and amplitude, was generated using the function generator and sent to the transmitter. Finally, the digital oscilloscope attached to the sensor was used to record the output signal and store it in the computer. The figure below summarizes the experimental set-up followed in all the experiments.

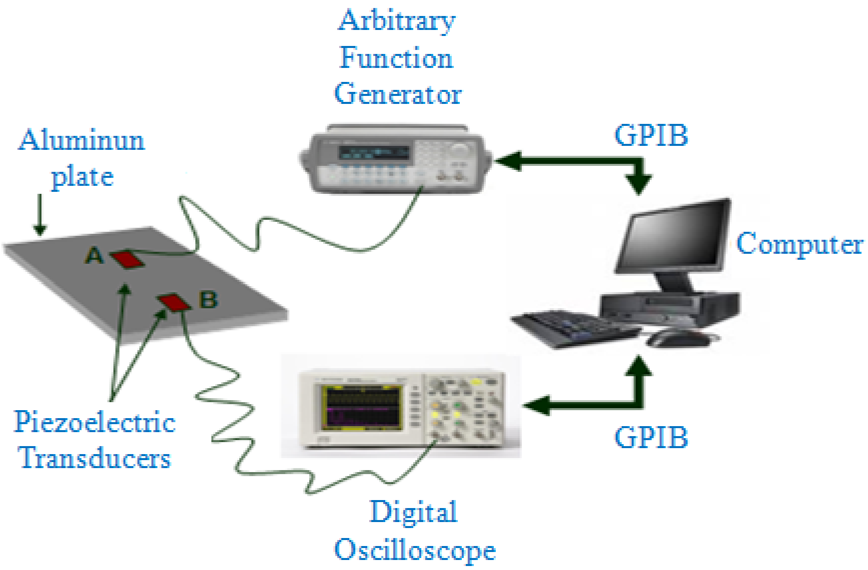

Figure 4.03: Experimental set-up of a standard pitch-catch configuration

3.1. Geometrical and Electro-mechanical Properties:

The Lead Zirconate Titanate (PZT) piezoelectric patches used in the experiments were purchased from STEMINC (STEINER & MARTINS, INC), they have the following properties:

- **Geometry:** square PZT patches of dimensions**:** 10x10x0.55 mm^3

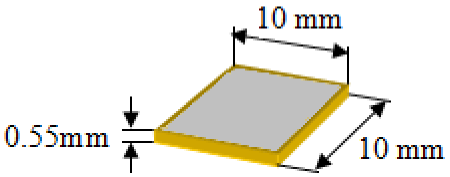

Figure 4.04: Piezoelectric wafer used in the experiments

❖ Electro-mechanical properties:

The piezoelectric patches used in all the experiments are made of the ceramic material SM410 with the Electro-mechanical properties summarized in Table 4.01.

Property	Unit	Symbol	Value
Electromechanical coupling coefficient		K_p	0.64
		K_t	0.45
		K_{31}	0.36
Piezoelectric constant	10^{-12} m/v	d_{33}	500
		d_{31}	-210
	10^{-3} Vm/N	g_{33}	23.3
		g_{31}	-10.3
Elastic Constant	10^{10} N/m^2	Y_{33}	5.6
		Y_{11}	6.5
Mechanical Quality Factor		Q_m	60
Dielectric constant	@1Khz	$\varepsilon_{33}/ \varepsilon_0$	2000
Curie temperature	^oC	T_c	320
Density	g/cm^3	R	7.7

Table 4.01: Electromechanical properties of the SM410 material

3.2. Aluminum Plate of Thickness 2mm:

Aluminum is a commonly used material in engineering and industrial applications (aerospace, civil, mechanical, etc.). It has specific chemical, mechanical and physical properties much like any other metal (steel, zinc, copper, etc). It is very light, with a weight of 2.7 g/cm^3 which represent approximately the third of the weight of steel. The use of aluminum in manufacturing applications reduces the weight of structures and components hence the energy consumption while maintaining high load capacities (for example in aircrafts design, less weight results in less fuel consumption). Aluminum presents also many others properties; it is highly resistive to corrosion, electrically and thermally conductive, adaptable to different applications (easy modification of the compositions of its alloys) and environment friendly (easily recycled). Moreover, wave propagation in aluminum is easily understood.

For all above reasons, we selected aluminum testing sample plates for our experiments. In this experiment, we used a 2mm thick aluminum plate with length and width both equal to 600mm. The plate is free of any visible crack.

3.2.1. Experimental Set-up:

Two piezoelectric wafers were bonded to the surface of the plate distant of 20 cm center-to-center using the Cyanoacrylate glue Permabond 10. The arbitrary function generator was used to generate and send an input signal to one of the wafers (acting as transmitter) in order to generate a mechanical lamb wave in the plate. The digital oscilloscope was directly connected to the second piezoelectric wafer (acting as a receiver) in order to visualize and record the output signal. Once the wave is sensed and captured by the oscilloscope, data was transferred to the computer via GPIB and gathered for further signal processing.

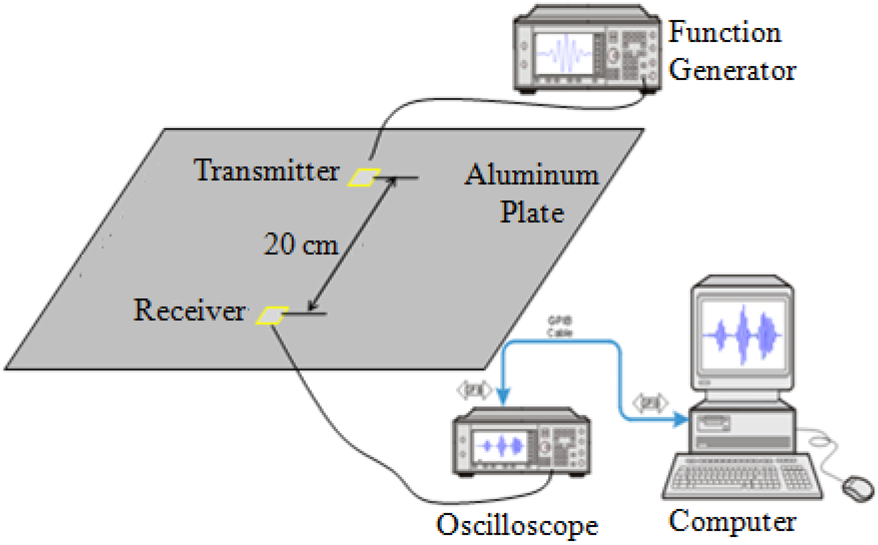

Figure 4.05: Experimental setup

A Morlet wavelet is used in this experiment as an input signal (Figure 4.06). The wavelet was built up in the computer, fed to the function generator and saved in the memory for further uses. The wavelet is centered at a frequency of 500 KHz. The frequency was chosen such that minimum number of modes is activated with sufficient amplitudes to propagate for the required distance. Due to the limitation of the arbitrary function generator, a peak to peak voltage of 10V was applied to the transmitter.

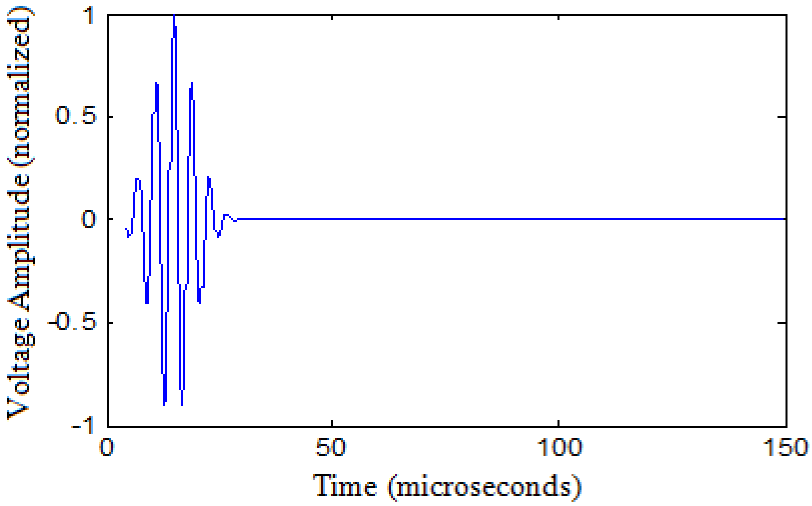

Figure 4.06: Input signal for lamb wave actuation: Morlet wavelet

3.2.2. Results and Discussions:

Lamb waves were generated in the 2 mm plate in a standard pitch-catch technique. After the wave propagates for a 20 cm, it reaches the receiver where it is sensed saved and analyzed. The Figure 4.07 shows the output signal sensed by the receiver.

The analysis of the output signal shows the presence of the two first fundamental modes S_0 and A_0 with extra packets due to the reflection of the wave from the edges of the plate. At the frequency of 500 KHz, the symmetric mode S_0 appears to be more dominant than the antisymmetric mode A_0.

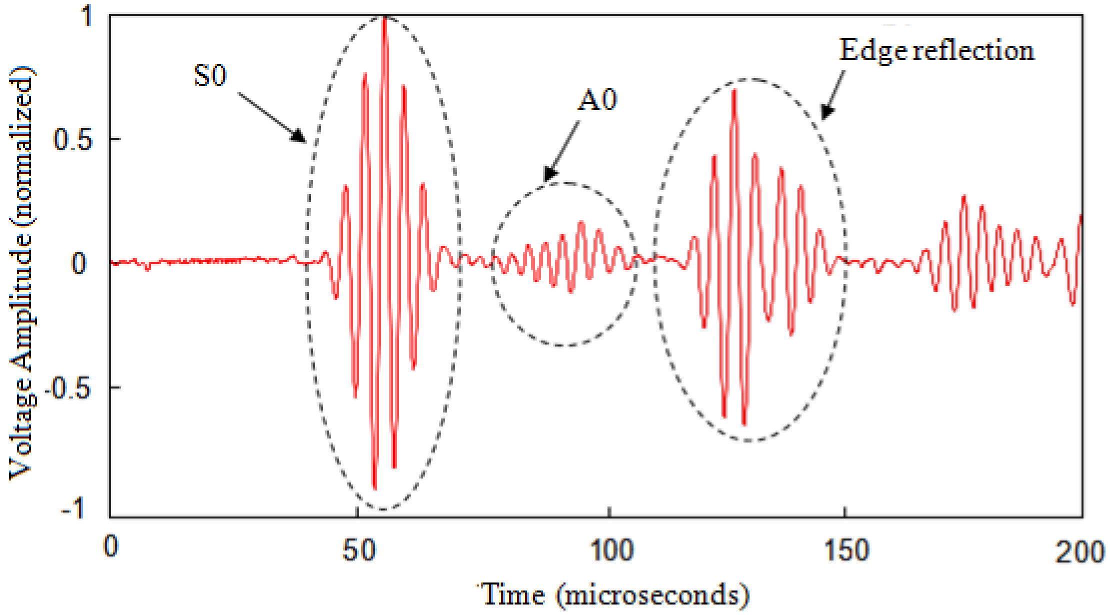

Figure 4.07: Output signal sensed by the receiver

The result confirms a fact related to lamb waves in thin structures: at higher ranges of frequency, S0 is dominant however at lower ranges of frequency A0 is dominant. Such property of lamb waves is important as it helps deciding which mode is to be used for the detection of cracks in a structure. Figure 4.07 shows also that the symmetric mode reaches the sensor earlier than the antisymmetric mode A0 which means that S0 is faster than A0. This actually can be seen on the dispersion curves for any thickness-frequency product (*f.d*). In fact, for a given thickness-frequency product, correspond two values of the velocities V_{ph}^{S0} and V_{ph}^{A0} for respectively S0 mode and A0 mode. Since we know the distance between the two piezoelectric patches, we can easily compute the time each packet of the wave takes to travel the required distance between the PZT actuator and the PZT sensor. This time is known as the time of flight.

3.3. Aluminum Plate of Thickness 4mm:

This part of the chapter is devoted to study the effect of the presence of cracks in aluminum plates on the propagation of lamb waves. For this reason, four aluminum plates of grade 3003-0 - SH were used in the experiments. One plate is healthy (without any defect) and the three other plates with predefined notches. The notches are of rectangular shape with similar lengths, similar widths but with different depths. The table below summarizes the dimension of the plates and the notches.

	Plate Dimensions			Notch Dimensions		
	Length	width	thickness	length	width	depth (d)
Plate 1	600 mm	600 mm	4 mm	20 mm	2 mm	0
Plate 2						1.6 mm
Plate 3						2.4 mm
Plate 4						3.2 mm

Table 4.02: Geometrical properties of the aluminum plates

The notches were introduced with depths equal to 40%, 60% and 80% of the plate thickness respectively for plates 2, 3 and 4

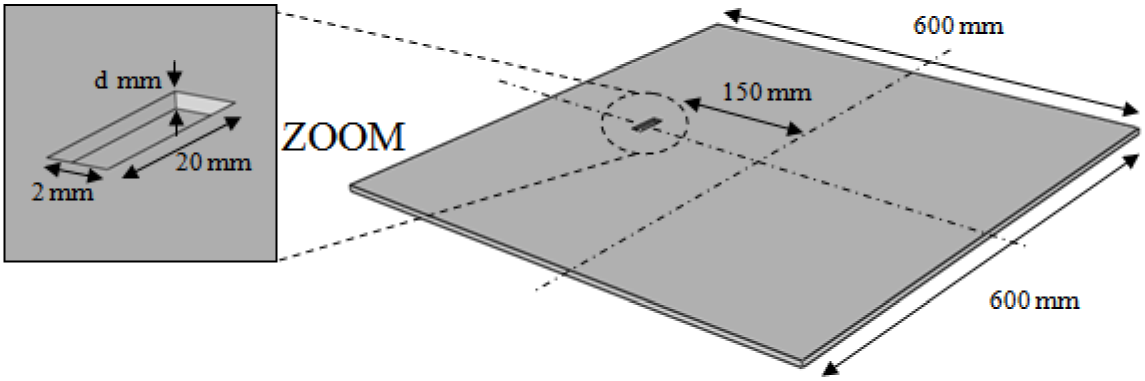

Figure 4.08: Geometry of an aluminum plate containing a predefined notch

3.3.1. Experimental Set-up:

Similar to the case of the 2mm plate described above, piezoelectric wafers were bonded to the surface of each plate using the Cyanoacrylate glue Permabond 10. The arbitrary function generator was used to generate and send an input signal to the piezoelectric transmitter in order to generate elastic lamb waves. The digital oscilloscope was directly connected to the piezoelectric receiver in order to visualize and record the output signal. Once the wave is sensed and captured by the oscilloscope, data is transferred to the computer via GPIB and gathered for further signal processing.

All the experiments in this section are based on the ultrasonic technique of pitch-catch. Two piezoelectric patches were attached on each plate, one acting as a receiver and the other as a sensor. The piezoelectric transducers were placed in the same positions for the four plates and two configurations (based on the location of the piezoelectric patches with respect to the location of the notch) were tested.

3.3.2. Actuator-Sensor-Notch Configuration:

In this configuration, the sensor was placed between the notch and the actuator at a distance of 15 cm. This configuration aims at studying the reflection of the incident lamb waves from the notch. A sketch of the experiment is shown in Figure 4.09.

Measurements were performed on the four aluminum plates at variable frequencies (frequency of the input signal). A range of frequencies from 100 KHz to 300 KHz with an increment of 25 KHz was selected in order to see, the behavior of lamb waves when interacting with the introduced notches.

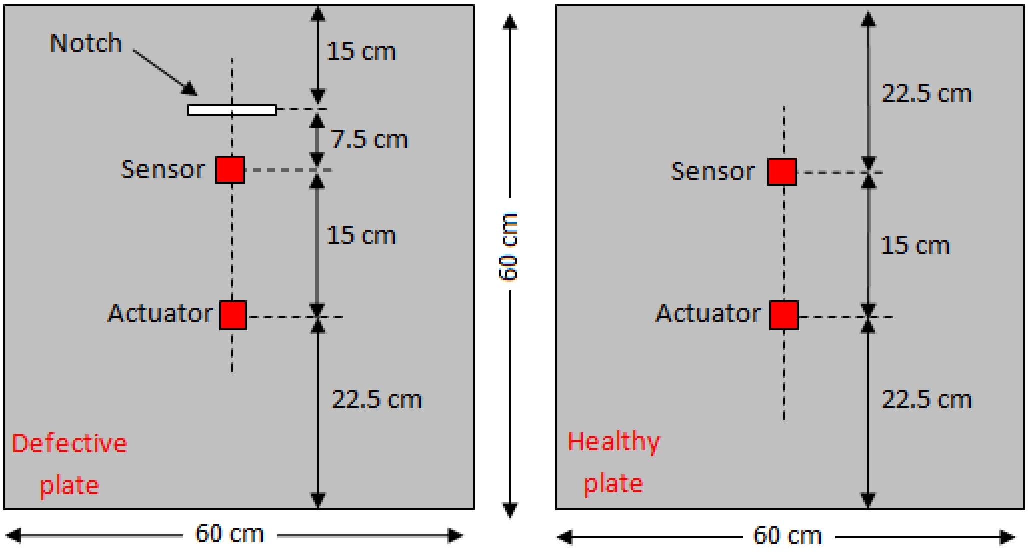

Figure 4.09: (a) Defective plates and (b) Healthy plate in an Actuator-Sensor-Notch configuration

❖ Results and discussions:

The data gathered from all the plates at different frequencies, are saved in the computer, and are presented in form of plots showing the output signals collected from the piezoelectric sensors. Using group velocity dispersion curves for aluminum; we extract the velocities of S0 and A0 modes at each frequency. The table below summarizes the computed velocities.

Frequency (KHz)	100	125	150	175	200	225	250	275	300
Velocity of S0 (ms^{-2})	5320	5300	5270	5200	5170	5100	5050	4950	4850
Velocity of A0 (ms^{-2})	2850	2950	3000	3050	3080	3100	3105	3110	3112

Table 4.03: Velocities of the fundamental modes S0 and A0 in the aluminum plates.

The velocities were used to determine times of flights of the different packets of the signal

- Incident symmetric wave: S0
- Incident asymmetric wave: A0
- Reflection of S0 from the crack
- Reflection of A0 from the crack
- Reflection of S0 from the close edge
- Reflection of A0 from the close edge

In the next plots, the following notations are used:

- T_{S0}: Time of flight of the incident S0
- T_{A0}: Time of flight of the incident A0
- T_{S0} (Defect): Time of flight of the scattered S0
- T_{A0} (Defect): Time of flight of the scattered A0
- T_{S0} (Edge): Time of flight of S0 reflected from the edge of the plate
- T_{A0} (Edge): Time of flight of A0 reflected from the edge of the plate.

The time of flight of the lamb wave is equal to the ratio of the distance travelled by the wave to reach the sensor to the velocity of the wave: $t_f = \frac{d}{V}$

The experimental configuration described above was tested at nine different frequencies (100 to 300 KHz with an increment of 25 KHz. The Output Data for each excitation frequency was gathered from the oscilloscope, processed in Matlab and presented in form of signals showing the response of the sensors on the four sample plates at that excitation frequency. Figure 4.10 shows the plot of the signals sensed in the four plates when the actuators were excited by a 250 KHz Morlet wave. Plots of all the others frequency cases can be seen in Appendix B. In all the plots, the region that correspond to the defect is limited by $T_{S0(Defect)}$ which marks the time when the incident signal reflects back from the defect and $T_{S0(Edge)}$ which corresponds to the time when the signal reflects from the closest edge of the plate.

Figure 4.10 shows that the signal in the region of the defect becomes more intense and its amplitude increases when the percent defect increases. This is explained by the fact that the defect reflects more energy when it is deeper and only a smaller part of the wave can propagate.

❖ Plots in the Time-Frequency Domain.

Analysis of the signals at different frequencies was also carried out in the time-frequency domain. Plots showing the intensity of the lamb wave were presented in order to interpret the influence of the crack on the propagation of the wave. Figure 4.11 shows the time-frequency plot of the signals sensed in the defected plates at 250 KHz excitation frequency. The plots of the others frequency cases can be seen in Appendix B.

The box in Figure 4.11 delimits the region of the signal where the input signal interacts with the defect. It can be seen in this region that the colors become more intense and more spread in the plot when the percent depth of the defect increases. This can be explained by the fact that the defect reflects more energy of the incident signal when its depth increases.

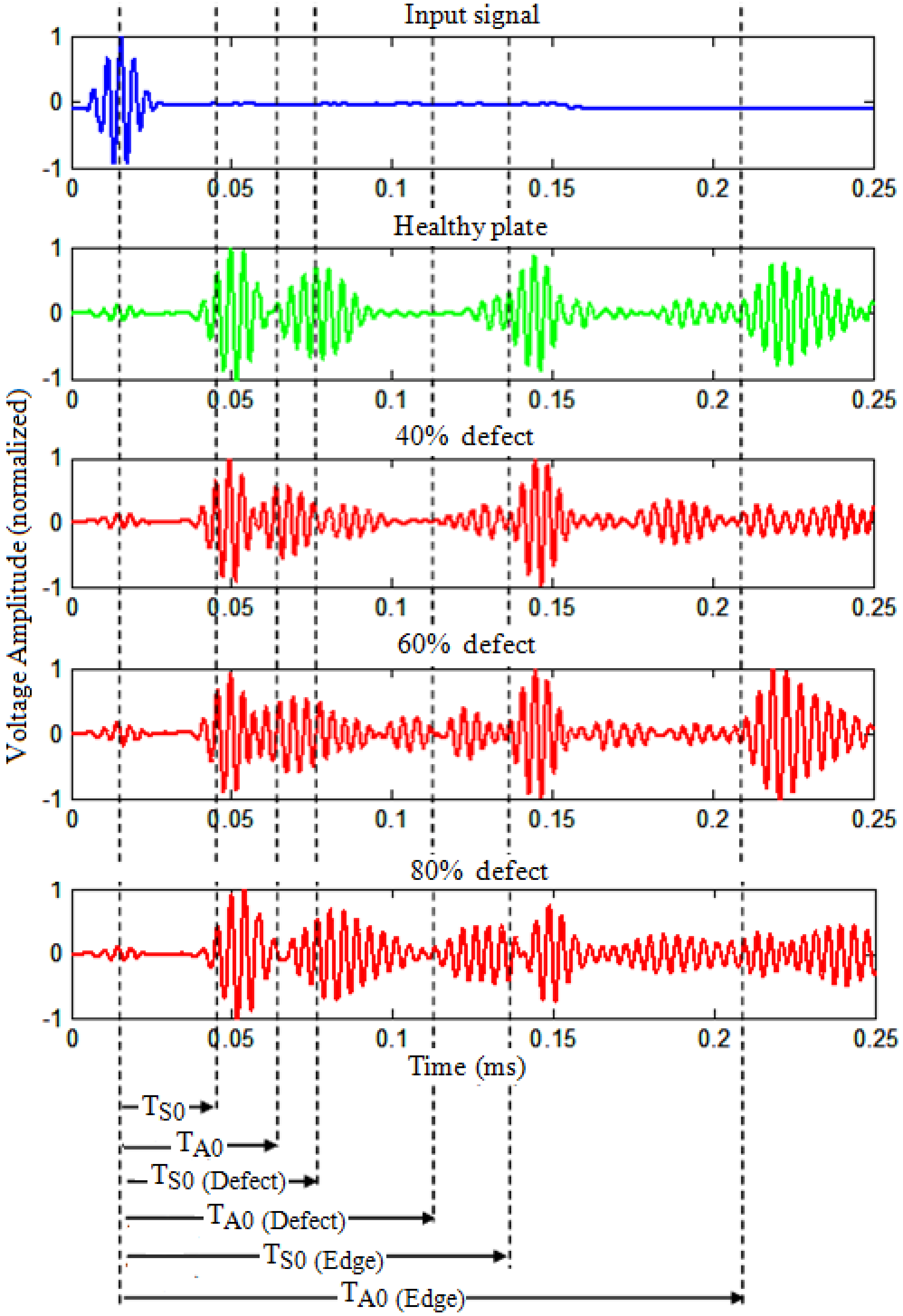

Figure 4.10: Input signal and Sensed signals at 250 KHz.

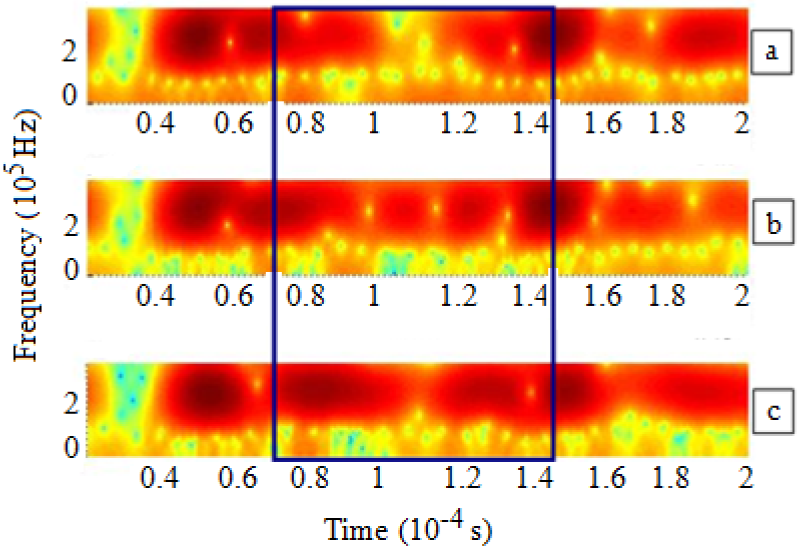

Figure 4.11: Time – Frequency plot at 250 KHz for different crack depths

(a) 40% T (b) 60% T (c) 80% T

3.3.3. Actuator-Notch-Sensor Configuration:

In this configuration, the notch is located between the actuator and the sensor. This aims at studying the effect of the notch depth on the amplitude of the incident wave. A sketch of the experiment is represented in Figure 4.12 where the actuator is placed at the center of the aluminum plate in order to avoid undesirable reflections from close edges and get clear incident signals without interference with backscattered waves.

Measurements on this experiment were also performed on the four aluminum plates in a frequency range ranging from 100 KHz to 300 KHz with an increment of 25 KHz. For all the frequency cases, focus was only placed on the symmetric mode S_0 of incident wave. The idea is to study the effect of the defect depth on the amplitude of the signal.

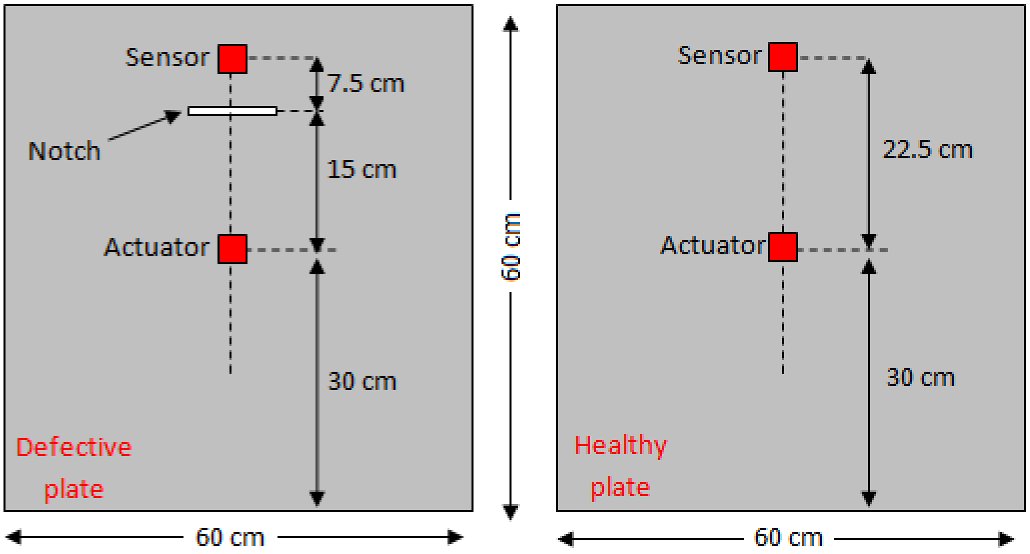

Figure 4.12: (a) Defective plates and (b) Healthy plate in an Actuator -Notch-Sensor configuration.

❖ Results and Discussions:

The experiment sketched in Figure 4.12 was carried out at different frequencies. The output data was gathered from the digital oscilloscope, saved in the computer then processed for use purposes. Only the region of the signal resultant from the propagation of the incident wave in the symmetric mode S0 is of concern. For this reason, the output signals sensed on the plates were chopped, in each frequency case, and regions of interest saved for further use.

Figure 4.13 illustrates the result of this experiment for the case of an exciting frequency equal to 250 KHz. It shows the variation of the amplitude of the signal as function of the defect depth. The coefficient R represents the depth of the notch measured in percent of the plate thickness. R takes the values 0, 40%, 60% and 80% which corresponds to the depths 0 mm (pristine plate), 1.6 mm, 2.4 mm and 3.2mm respectively. We clearly see that the amplitude decreases when the depth increases. The interpretation of this finding is based on the fact that the amplitude of the signal is proportional to the amount of energy transmitted through the defect. In fact, the defect transmits less energy of the incident wave when its depth increases and a weaker signal with smaller amplitude is obtained. The figures corresponding to the other frequency cases are appended in Appendix B

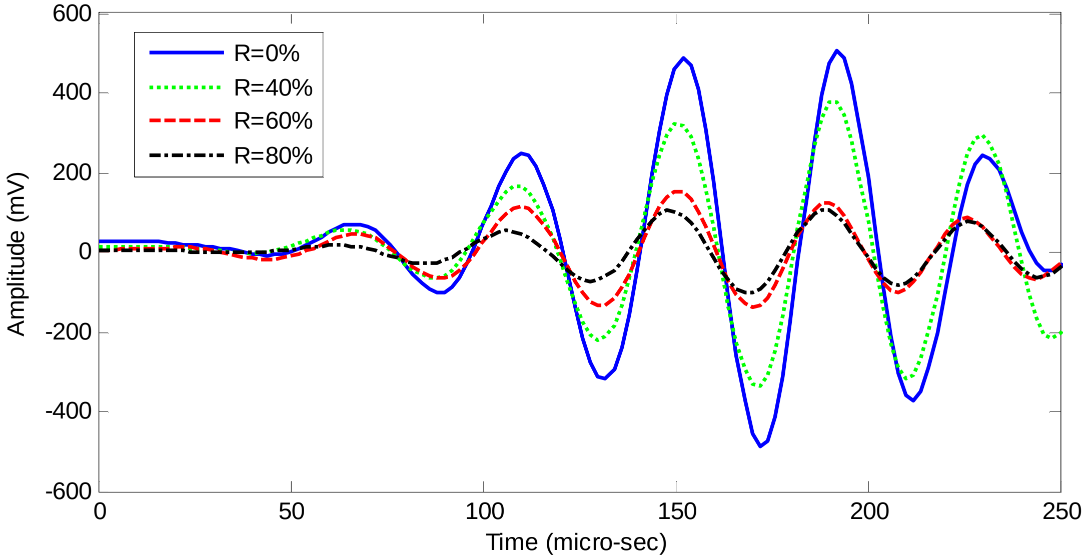

Figure 4.13: S0 mode at 250 KHz for deferent crack depths

4. Conclusion:

In this chapter, experiments based on the ultrasonic technique of pulse-echo were conducted on four aluminum plates with manufactured notches of variable depths in order to characterize the effect of defects on the behavior of piezoelectric actuated lamb. First, a simple experiment used as proof of concept was conducted on a 2 mm thick aluminum plate in order to check the quality of the piezoelectric patches and to ease the understanding of lamb waves before conducting the major experiments. Second, experiments were carried out on 4 mm thick aluminum plates in order to study the effect of the notch depth on the behavior of lamb waves. Results show that for notches with same lateral dimensions and different depths, the energy of the transmitted signal decreases when the depth of the notch increases.

Chapter 5

Phased Array Health Monitoring

1. Introduction:

Piezoelectric materials have been of great advantages in Structural health monitoring applications. They enable quick, efficient and less costly inspection operations. During the last few years, piezoelectric materials have been combined with more advanced nondestructive techniques in order to enhance the assessment of structures and solve inspection problems that traditional techniques could not solve. As a result, many smart techniques have been developed and successfully used in diverse applications.

In ultrasonics, the technique of phased arrays stands among the best advanced techniques that rely on the use of smart piezoelectric elements in emission and sensing applications for inspection of structures. It is based on a concept and principles similar to the radar, sonar, seismology, oceanography and medical imaging (Lines *et al* [33]): a set of probes made of the same material and arranged in a desired form (linear, circular, matrix, etc.) are driven either independently or simultaneously in order to emit and receive focused waves that can be used to inspect a structure. The probes used in the phased array are actuated in different manners (different modifications of the directivity pattern of the array) in order to form moving beams, focused beams and or deflected beams that propagate in desired directions. This procedure is known as beam forming and it aims at steering the maximum sensitivity of the array in a desired direction of particular interest in order to obtain the maximum amplitude of the received signal.

Phased arrays technique has gained wide interests in both the industrial and the research communities and has been successfully applied as an alternative for ultrasonic conventional techniques. In fact, the phased array ultrasonic technique presents major advantages over ordinary and conventional ultrasonic techniques. For example, it helps reducing the inspection times by performing fast electronic scanning and eliminating the need for mechanical scanning. As a result the reliability of measurements is considerably improved and variations and changes due to losses of the contact between the probe and the structure are decreased. Phased arrays technique has also the ability to control the ultrasonic beam and steer it in a desirable direction which helps optimizing inspection operations whereas in conventional technique, the wave cannot be steered and it has only one orientation.

Due to its enabling capabilities, the phased array ultrasonic technique has been the subject of research for many scientists. Deutsch *et al* [09] presented one of the earliest works which investigates on the use of the phased array technique for lamb wave. They developed a time reversal based method in order to focus a uniform linear array on a defect. Wilcox *et al* [54] proposed an array approach using ceramic disc of circular shape in order to inspect large areas of thick plates. Giurgiutiu *et al* [17] developed a new approach of health monitoring using phased array technique. They proposed an experimental set up which they called “embedded-ultrasonic structural radar” (EUSR). This setup involves the use of a linear array of piezoelectric wafer actuated sensor (PWAS) fired in round-bond manner so that to produce a virtual beamforming in order to detect two manufactured defects in a thin aluminum plate. Hong *et al* [52] conducted a numerical study on which they successfully implement a virtual lamb wave phased array using 16 piezoelectric patches for damage detection purposes. Many others works have been performed in order to study the applicability of the ultrasonic method phased array in health monitoring tasks.

2. Ultrasonic Method of Phased Array:

2.1. Concept:

In ultrasonics, a phased array is a set of probes driven independently or simultaneously with variable time delays in such a way that the directivity or the propagation pattern of the array is altered. This aims at intensifying the propagation in a desired direction (Figure 5.01) and suppressing it in unwanted directions.

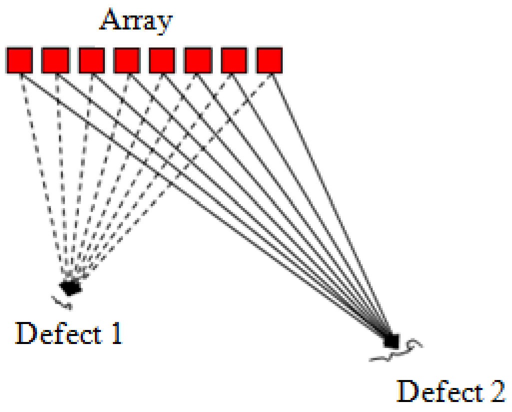

Figure 5.01: Beam focusing on misoriented cracks

2.2. Principles:

In a phased array experiment, the probes are fired independently or simultaneously with variable time delays so that to steer the beam in a desired direction Figure 5.02. When the incident wave front resulting from the constructive beam forming reaches a defect, a part of the energy will reflect back to the array and reach the elements at different times. In order to get the total scattered signal due to the actuating array, appropriate time delays should be applied to the signals sensed at each element.

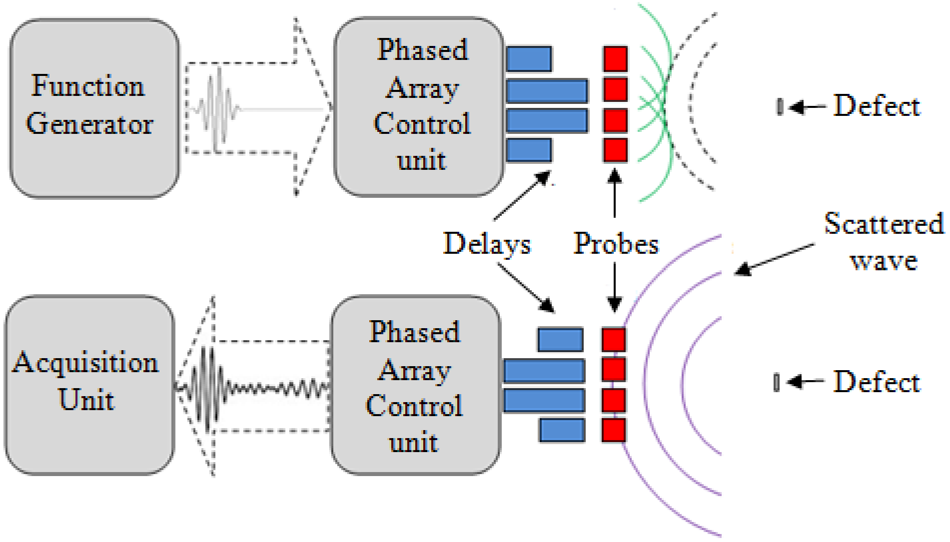

Figure 5.02: Beam forming technique

3. Piezoelectric Array for Inspection of Aluminum Plates:

3.1. Description:

Giurgiutiu *et al* [17] developed the technique of Embedded-ultrasonics structural radar (EUSR) by which they proved that a linear array of piezoelectric wafer active sensors permanently attached to an aluminum plate can perform as good as any conventional ultrasonic phased array apparatus in the detection of cracks and flaws in an aluminum plate. This technique is easy to implement, cheap (available and cheap piezoelectric materials), efficient and rapid.

The technique is based on a virtual scan of the structure on which the array of piezoelectric wafer active sensors is mounted or embedded. The virtual scan is achieved by activating the elements of the array independently in a round-robin fashion and collecting the data from all the elements. An assembly of the gathered data is then generated and analyzed using signal processing methods in order to synthesize the virtual transmitted and received waves and apply beamforming theory for the detection of cracks and damages.

In this thesis, a method based on the same concept of the EUSR technique was used for the inspection of aluminum plates with variable crack depths. The method uses also a linear array of piezoelectric wafers active sensor in order to actuate and sense lamb waves in the four aluminum plates. The difference, in this thesis, is that the assumption of far field and Omni-directional wave in Girgiutiu’s work was not followed. Rather, a different formulation for time delays was adopted.

3.2. Experimental Setup:

Ultrasonic Phased arrays experiments were conducted on the four aluminum plates used in the previous experiments. Each plate was implemented with an array of 6 piezoelectric elements of length, width and thickness equal to 10 mm, 10 mm and 0.5 mm thick respectively. For the Healthy plate, the objective was to focus the beam on a point located at one of the edges (Figure 4.04). The beam was steered at an angle of 90 degrees from the axis of the array.

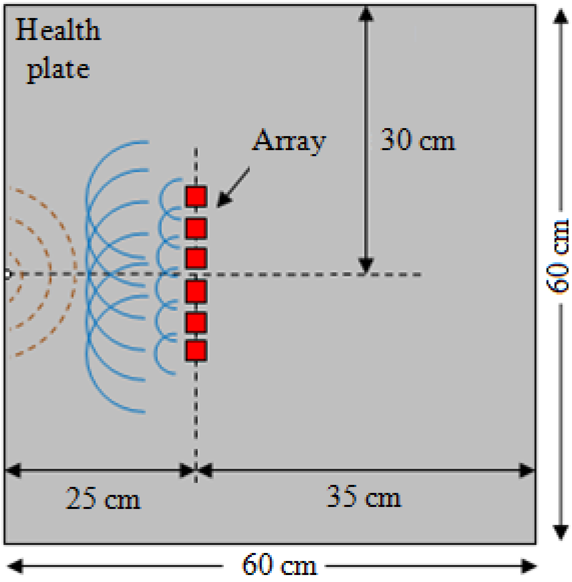

Figure 5.03: Sketch of the phase array on the healthy plate

For the defective plates, the objective was to focus the beam on the manufactured defect located at a focal distance d=20 cm from the axis of the array (Figure 5.04)

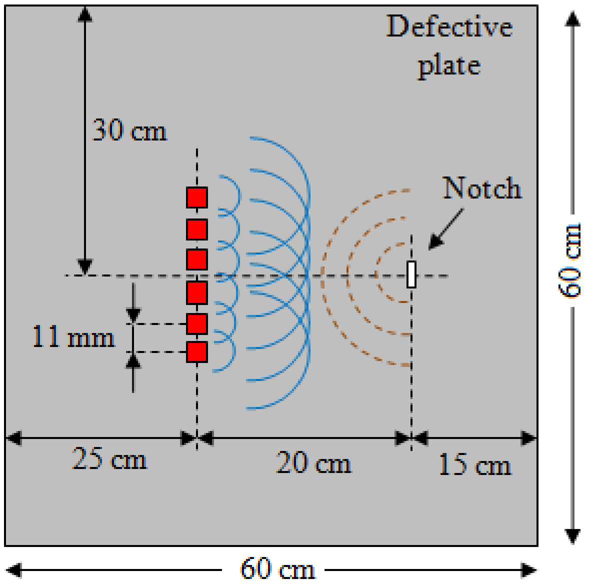

Figure 5.04: Sketch of the phase array on a defective plate

In order to generate a virtual phased array signal, all the elements of the array were actuated separately in a round-band fashion (Giurgiutiu and Bao 2004) which means we actuate only one element each round and receive signals from all the others element. At the end we collect all the signals and arrange them in a matrix form in order to apply the necessary delays.

	T_0	T_1	T_2	T_3	T_4	T_5
R_0		T_1R_0	T_2R_0	T_3R_0	T_4R_0	T_5R_0
R_1	T_0R_1		T_2R_1	T_3R_1	T_4R_1	T_5R_1
R_2	T_0R_2	T_1R_2		T_3R_2	T_4R_2	T_5R_2
R_3	T_0R_3	T_1R_3	T_2R_3		T_4R_3	T_5R_3
R_4	T_0R_4	T_1R_4	T_2R_4	T_3R_4		T_5R_4
R_5	T_0R_5	T_1R_5	T_2R_5	T_3R_5	T_4R_5	

Table 5.01: Matrix of signals collected from each plate

In the Table 5.01, the cell in row *i* and column *j* contains the signal $T_i R_j$ recorded by the element receiver 'R_j' when the element transducer 'i' is fired.

3.3. Time Delays:

In a traditional phased array experiment, all the probes in the array are fired simultaneously with different time delays in order to steer the beam at a specific direction. In this experiment, we actuated the elements of the array separately and without delays. So, we applied appropriate time delays in order to focus the beam on the notch.

The required time delays were computed using a general focusing technique proposed by Azar *et al* [05]. The expression was successfully used by Hong *et al* [52] to numerically implement a virtual phased piezoelectric array

$$t_i = \frac{D}{c}\left\{\left[\left(\frac{Nd}{D}\right)^2 + 2\frac{Nd}{D}\sin\theta_s\right]^{\frac{1}{2}} - \left[\left(\frac{(i-N)d}{D}\right)^2 - 2\frac{(i-N)d}{D}\sin\theta_s\right]^{\frac{1}{2}}\right\}$$

t_{i}: required time delay for the i th element of the array.

D: distance from the center of the array to the point where the beam is to be focused at.

c: is the wave speed, θ_{S}: steering angle

N: number of actuating elements in the array.

n=0, …, N-1: array index, $N = (N-1)/2$

Using the proposed equation we compute the required time delays for the elements of the array on the healthy plate and the time delays for the elements of the arrays on the defective plates.

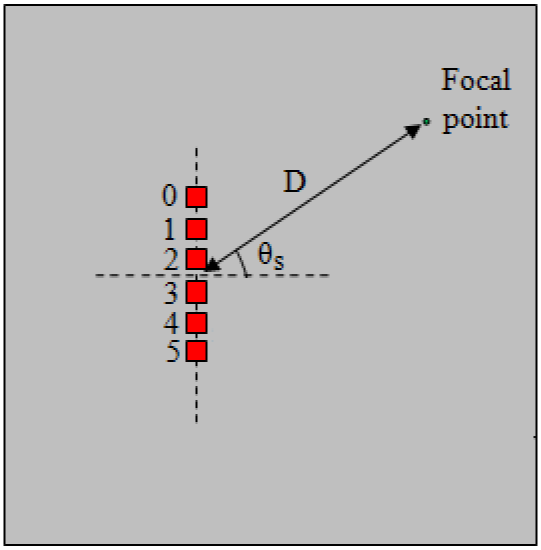

Figure 5.05: Sketch of the phased array for a random location (D, θ_S)

3.4. Healthy Plate:

The beam was focused on one edge of the plate at the distance *D*=25 cm and a steering angle θ_S=0. The experiment and the corresponding timing delays are shown on Figure 5.06.

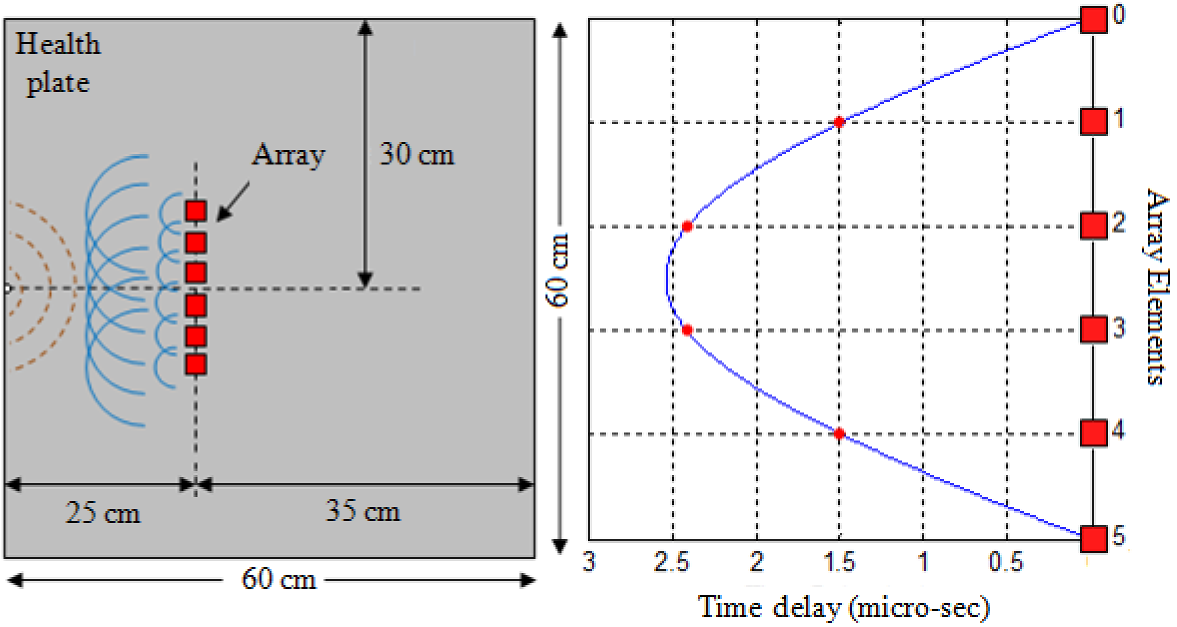

Figure 5.06: Sketch of the phased array and corresponding time delays for the healthy plate

3.5. Defective Plates:

The beam on the defective plates were focused on the defect located on a focal distance D=20 cm and a steering angle θ_S = 0 degrees. The sketch of the experiment and the corresponding timing delays are shown on Figure 5.07.

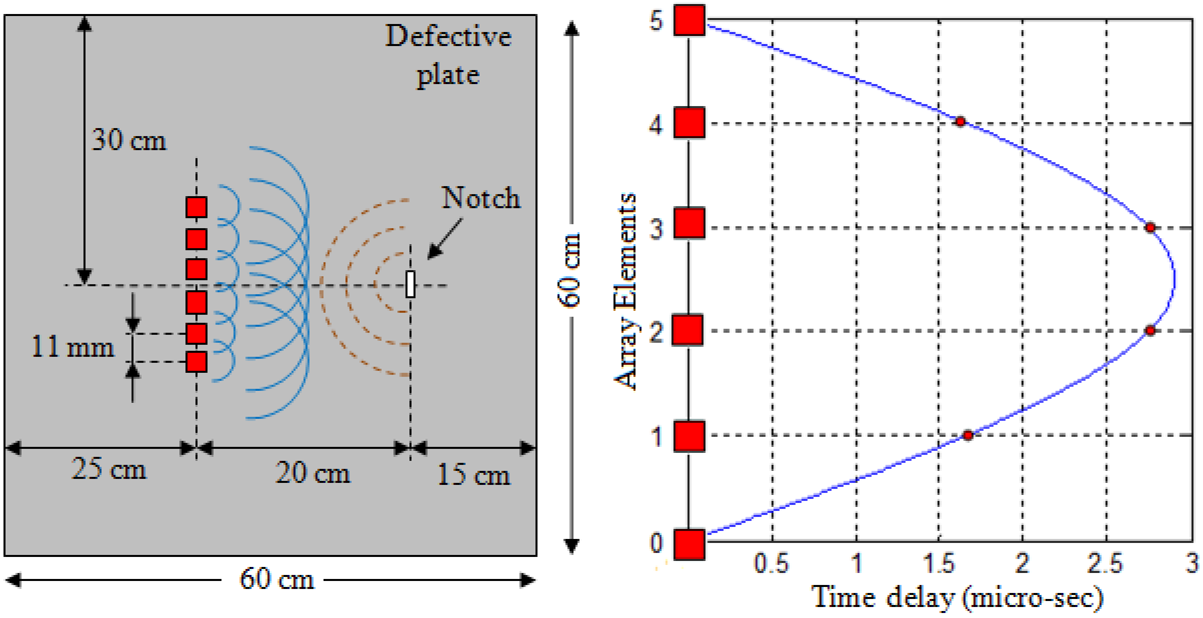

Figure 5.07: Sketch of the phased array and corresponding time delays for a defective plate

3.6. Results and Discussions:

Once all the elements of the array fired and the signals sensed, we proceed to the construction of the virtual beamforming by applying the appropriate time delays to the signals received by each piezoelectric element.

The total signal R_j received by the element j; $j \in \{0,1,2,3,4,5\}$ is given by the expression:

$$R_j = \sum_{\substack{i=0\\ i\neq j}}^{5} T_i R_j$$

The summation is computed for each element of the array after all the necessary time delays are applied to the corresponding signals T_iR_j. The plots in Figures 5.08, 5.09, 5.10 and 5.11 illustrate the total signals received by the elements of the array for the healthy plate, the plate with 40% defect, the plate with 60%defect and the plate with 80% defect respectively.

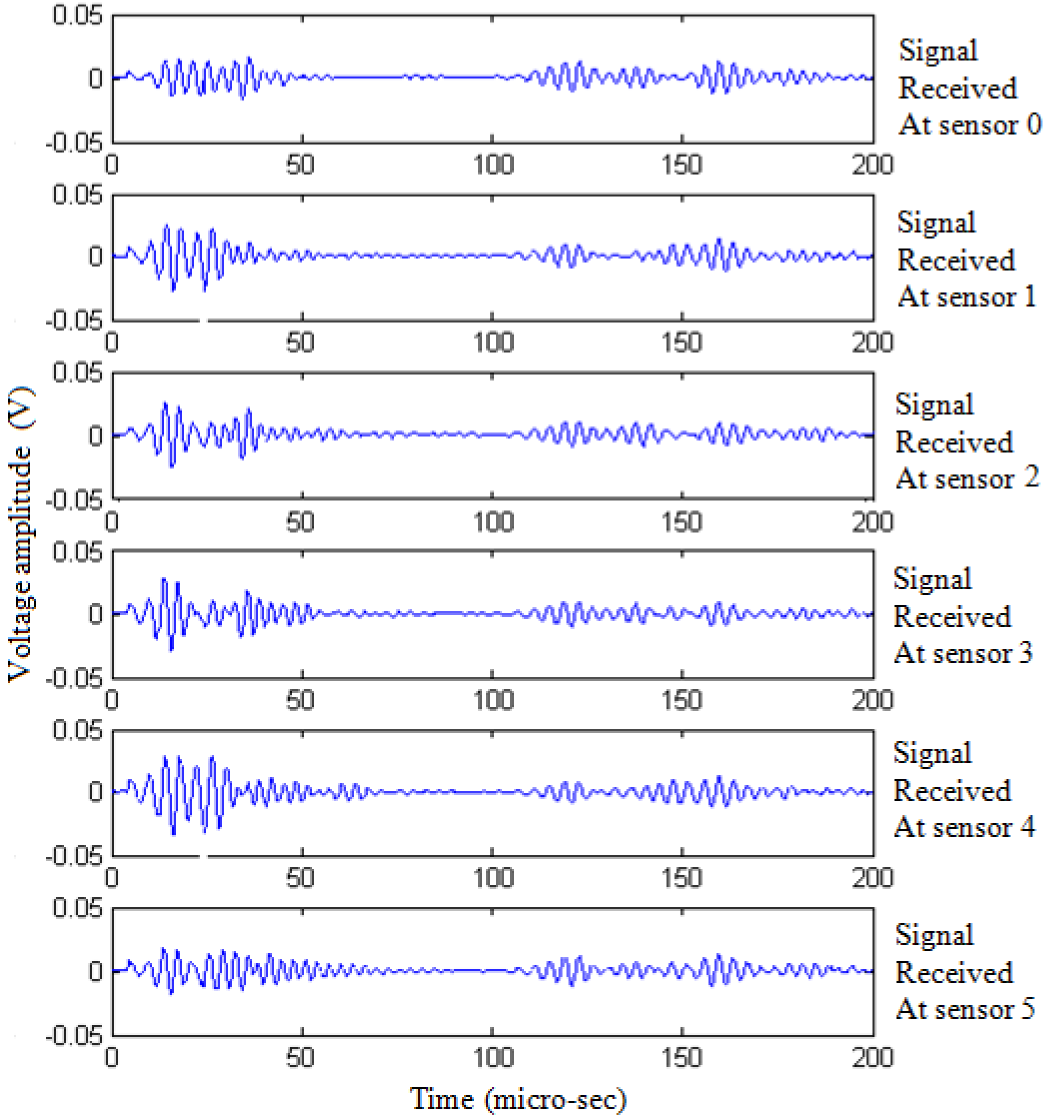

Figure 5.08: Signals Received by the Sensors on the healthy plate

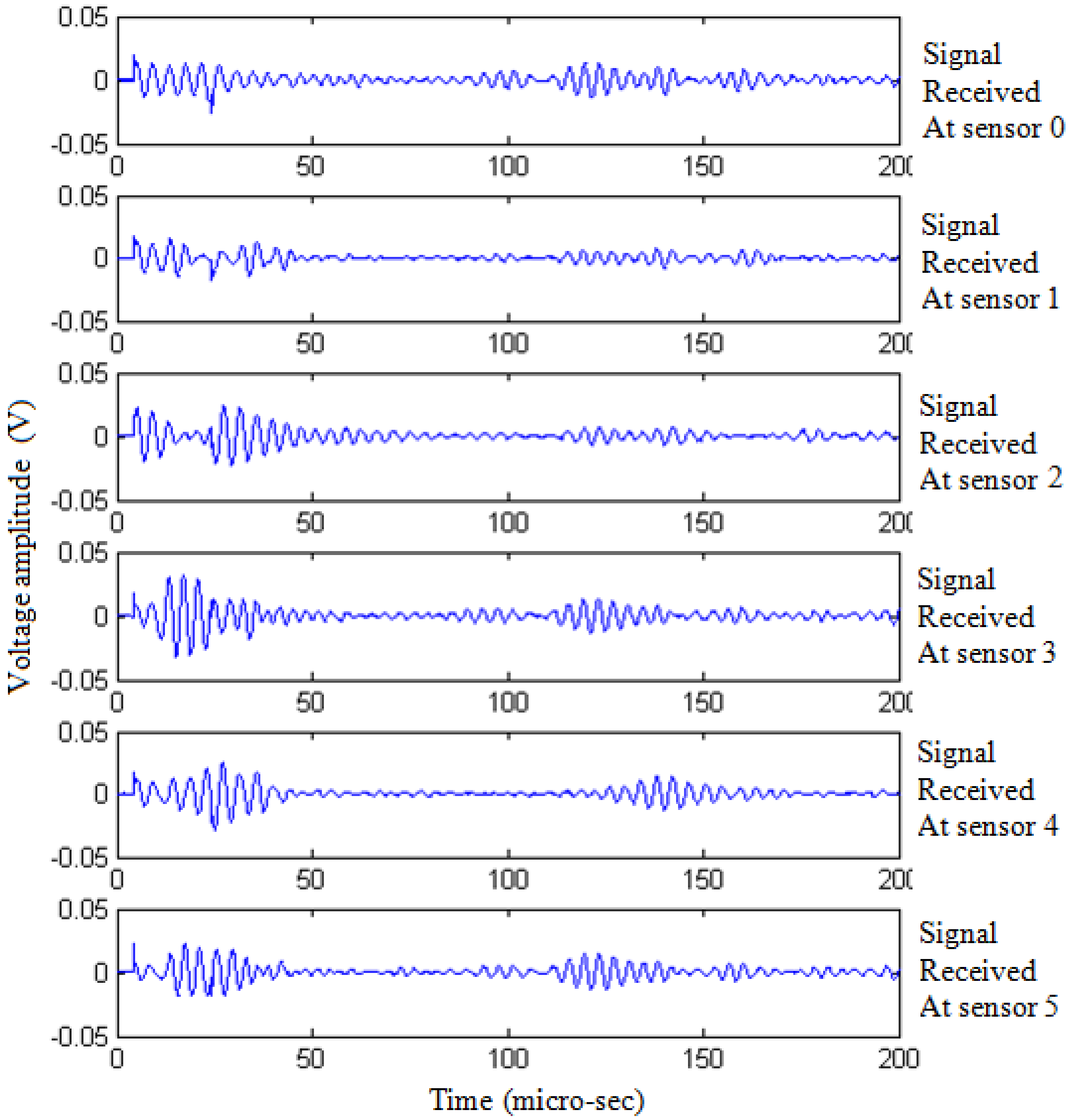

Figure 5.09: Signals Received by the Sensors for the plate with 40% defect depth

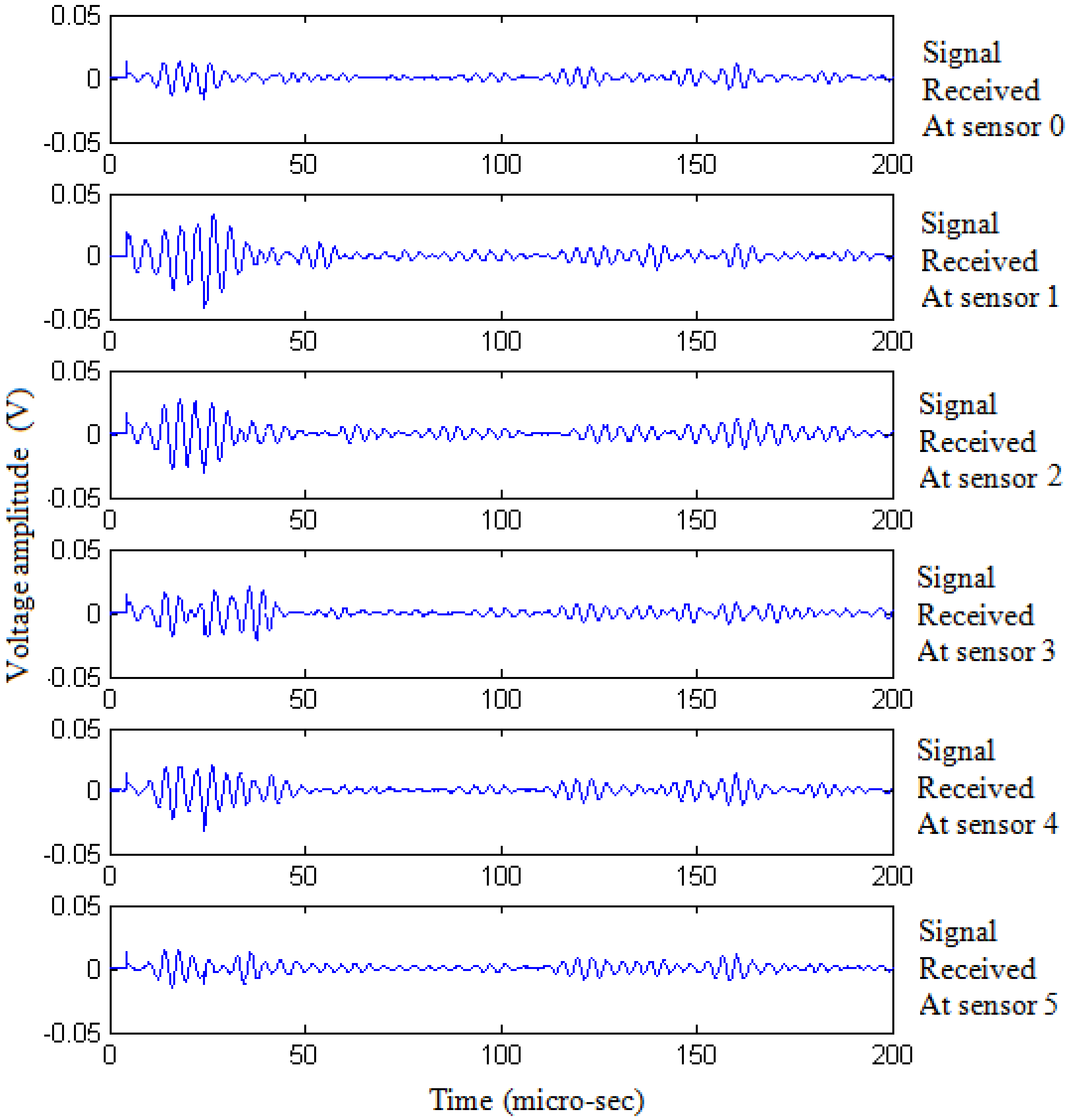

Figure 5.10: Signals Received by the Sensors for the plate with 60% defect depth

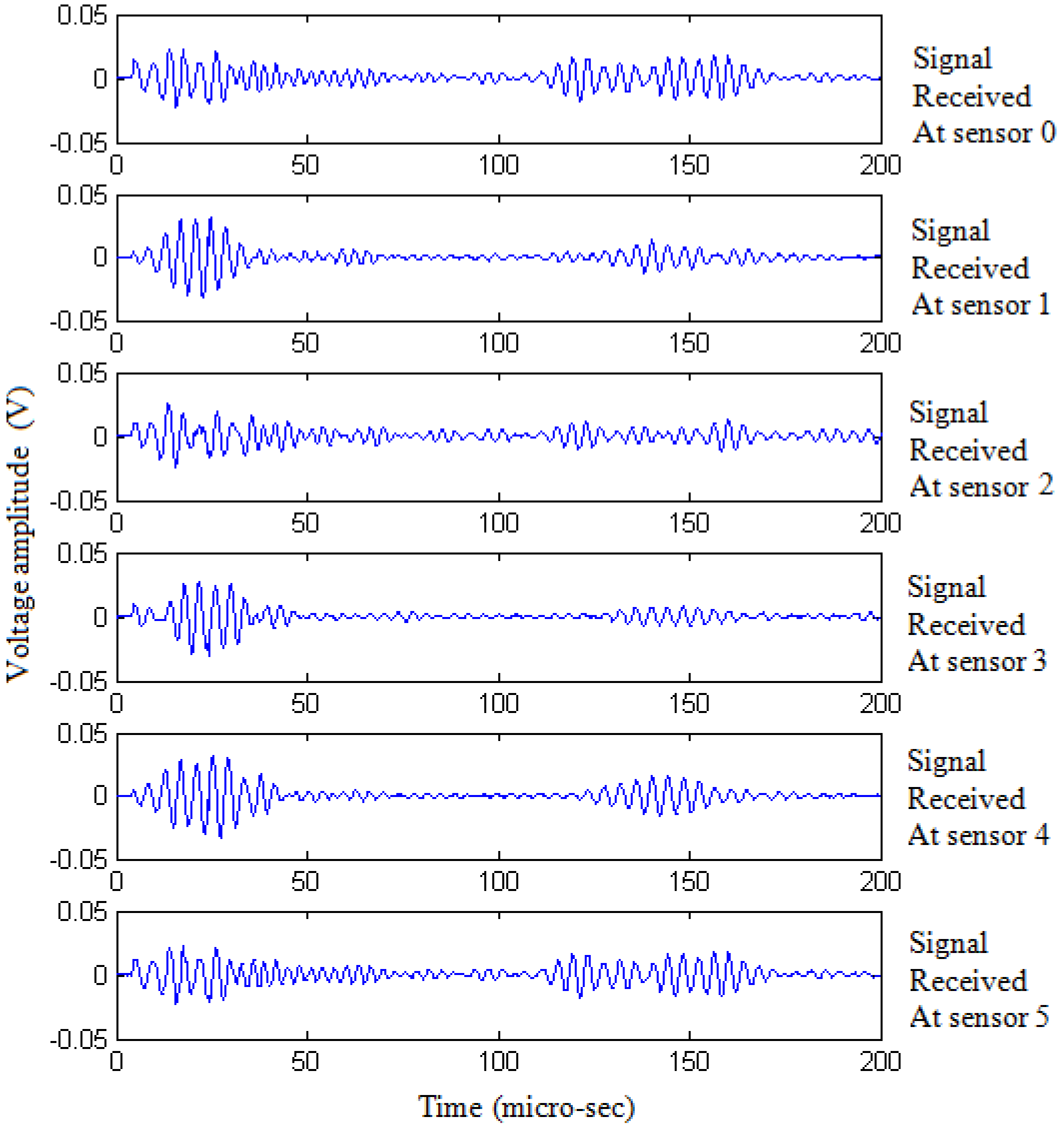

Figure 5.11: Signals Received by the Sensors for the plate with 80% defect depth

After applying the time delays and obtaining the total signal in each element of the array, it is now easy to find the final signal sensed by the array. This can be easily done by simply adding all the tolal signals obtained on the elements of the array. For example, for the case of the healthy plate, all the signals in Figure 5.08 summed up together form the final signal sensed by the array on the plate (Figure 5.12). Similar procedure was applied for three the defective plate.

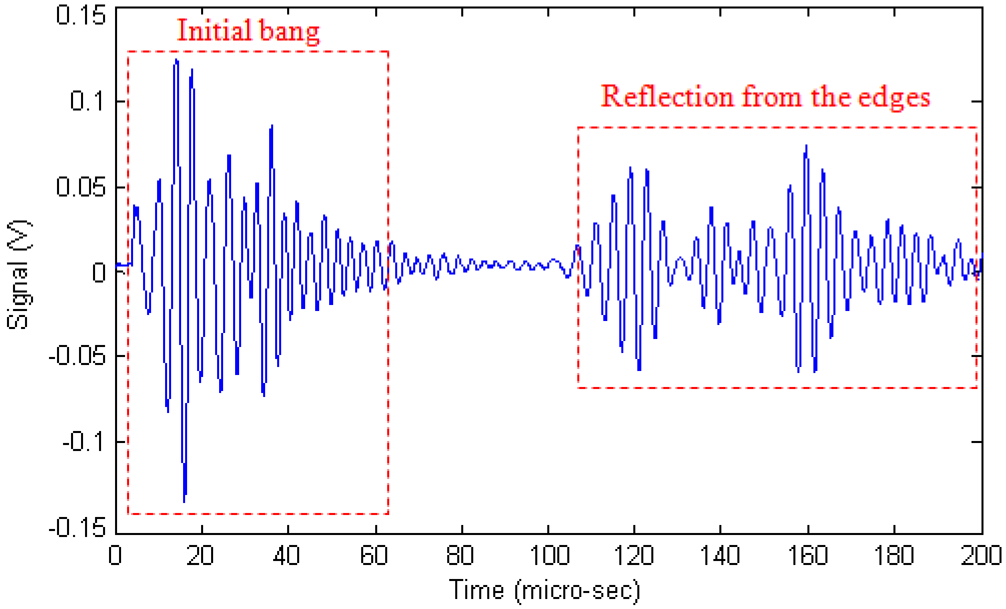

Figure 5.12: Total Signal Received by the array on the healthy plate

The plot in figure 5.12 shows that the total signal on the healthy plate is formed of two main wave packets: a first packet represented by an initial bang in which are included both the symmetric mode S0 and the anti-symmetric mode A0 of the incident wave and a second region which contains the reflection of the incident wave from the edges of the plate. Those packets can also be seen on the signals of the defective plates but the main difference is that each signal sensed on a defective plate contains one more packet which represents the reflection of the incident wave from the defect. Those packets are depicted by the plots in Figures 5.13, 5.14 and 5.15.

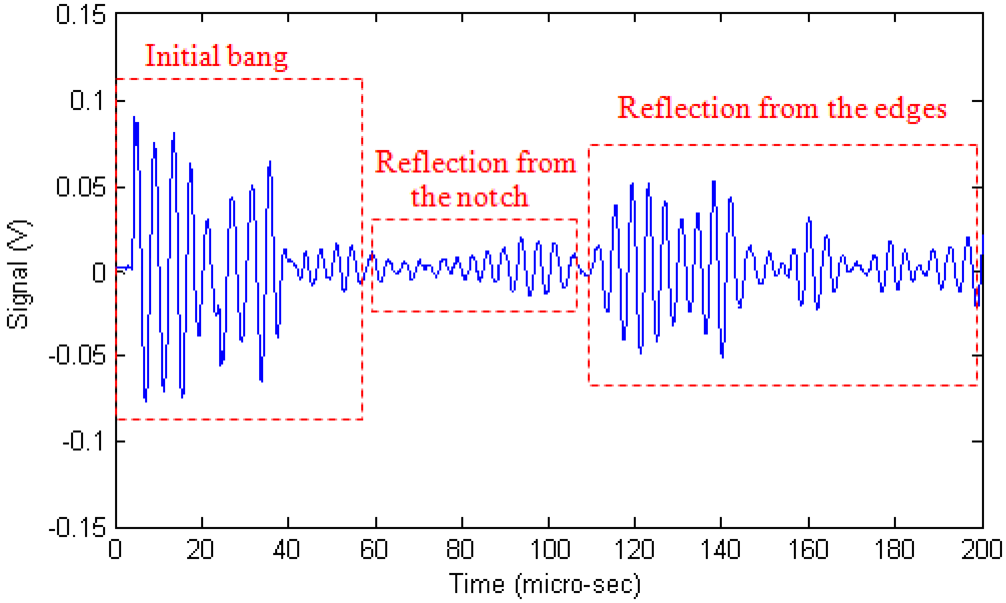

Figure 5.13: Total Signal Received by the array (40% defect depth)

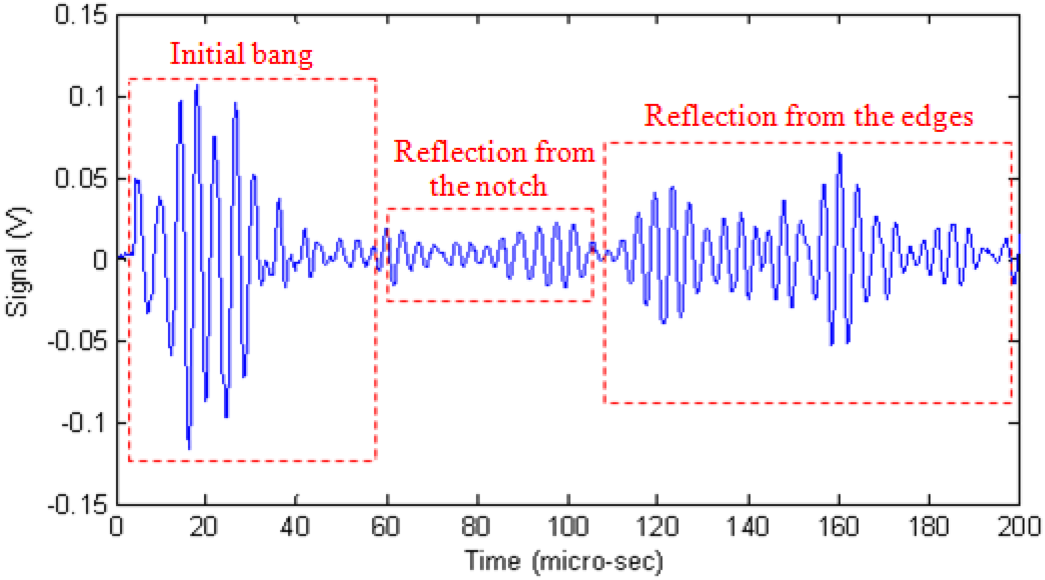

Figure 5.14: Total Signal Received by the array (60% defect depth)

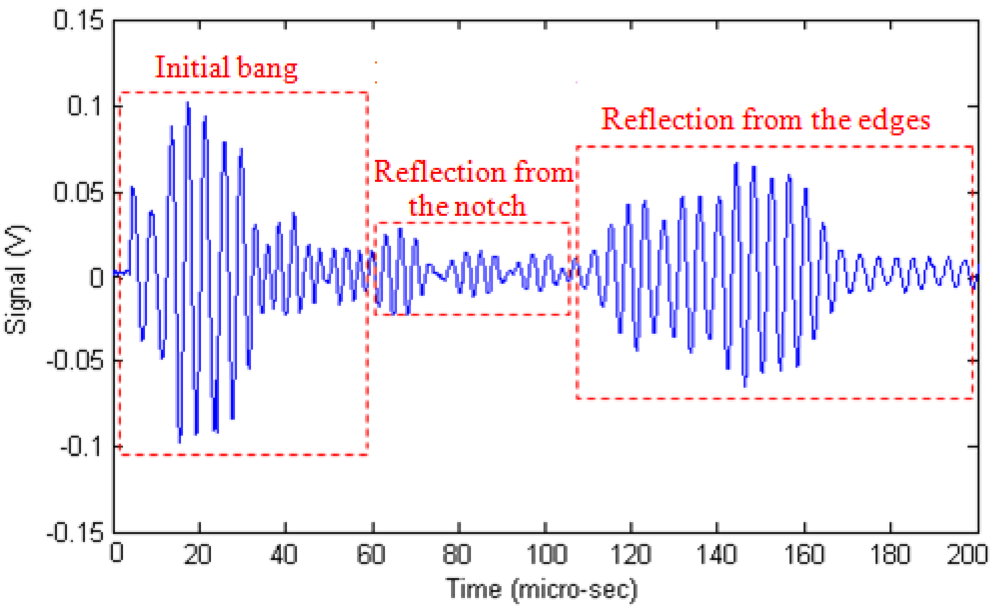

Figure 5.15: Total Signal Received by the array (80% defect depth).

4. Conclusion:

In this chapter, experiments based on the technique of ultrasonic phased arrays were conducted on four aluminum plates, one healthy and three defective plates with manufactured notches of variable depths. The idea was to illustrate the principle of phased arrays and see its efficiency in detecting the manufactured notches present on the plates. For this reason, a virtual beamforming method, for which an array of six piezoelectric transducers actuated in a round-bond manner, is applied in order to characterize the behavior of lamb waves in presence of the manufactured defects. Signals are collected separately and appropriate delays are applied in order to form the total signal sensed by the phased array. Results show that the phased array was successfully used to detect the manufactured damages on all the defective plates. This makes from the technique of virtual beamforming used with an array of simple piezoelectric transducers a good experimental alternative for the detection, the qualification and the quantification of more complex and misoriented damages present in different daily used structures.

Chapter 6

Conclusion

This thesis discusses some main properties and applications of piezoelectricity and lamb waves in structural health monitoring. In a first part, numerical and analytical simulations of an unbonded piezoelectric patch were conducted in order to plot the impedance and study its variation with the variation of the compliance and strain parameters of the patch. The results of the experiments showed that the compliance coefficients have an effect on the frequencies of peaks of resonance and antiresonance while the strain coefficients have an effect on the amplitude of the impedance. The comparison between the numerical results and the analytical results showed some differences between the curves of impedance. Those differences were considerably, but not fully, reduced when some variations were applied to some of the parameters. Such a study can be of good utility for the understanding of the electromechanical behavior of the patch and can also be useful for controlling its quality before using it in experiments.

In the second part of the thesis, experiments on the wave propagation in finite aluminum plates were conducted in order to show the efficiency of lamb waves in the detection of defects present in finite aluminum plates with predefined notches of different depths. For this reason small piezoelectric transducers have been used as both actuators and sensors in order to generate lamb waves in the aluminum plates. The idea behind this first experiment was to show the effect of the notch depth on the propagation of energy transported by the wave. It has been shown that the amount of energy transmitted through the notch decreases with the increase in the depth.

The propagation of lamb waves actuated by a phased array of piezoelectric transducers was also investigated in this thesis. The main idea behind the experiment was to focus the wave in a specific direction in order to detect defects manufactured on three aluminum plates. The results show that the technique of virtual beamforming used on an array of simple piezoelectric was successful in detecting the defects pre-installed on the aluminum plates.

APPENDIX A

\

- **ANSYS CODE USED FOR THE NUMERICAL SIMULATIONS:**

```
fini
/CLEAR,START                                  ! START NEW MODEL.
/FILNAME,Impedance
/TITLE,Impedance Analysis PZT-5A
/CONFIG,NRES,1e+6
/PREP7
csys,0
/UNITS,SI
! *******************************************************************************
/com USER DIMENTIONS OF PZT

L=20e-3                             ! length of the PZT
W=1e-3                              ! width of the PZT
thick=0.5e-3                        ! thickness of the PZT
mesh_size_l=200                     ! No of elements in length
mesh_size_w=10                      ! No of elements in width
mesh_size_thick=5                   ! No of elements in thickness
! a mesh of 0.1mmX0.1mmx0.1mm

/com    Compliance matrix
! *******************************************************************************
/com   PZT-5A PIEZO ELEMENT Z-POLARIZED STIFFNESS MAT PROP
/COM,   MATERIAL MATRICES (POLAR AXIS ALONG Z-AXIS)
/COM,
/COM,   [S11 S12 S13  0    0    0  ]         [  0    0  e31]          [eps11    0        0    ]
/COM,   [S12 S22 S23  0    0    0  ]         [  0    0  e32]          [    0    eps22    0    ]
/COM,   [S13 S12 S33  0    0    0  ]         [  0    0  e33]          [    0        0    eps33]
/COM,   [  0    0    0  S66   0    0  ]      [  0    0    0 ]
/COM,   [  0    0    0    0  S44   0  ]      [  0  e42  0 ]
/COM,   [  0    0    0    0    0   S55]      [e51  0    0 ]

TB,ANEL,1,1,21,1
TBDATA,1,16.4E-12,- 5.74E-12,-7.22E-12          ! S11,S12,C13
TBDATA,7, 16.4E-12, -7.22E-12                   ! S22,S23
TBDATA,12, 18.8E-12                             ! S33
TBDATA,16, 44.3E-12                             ! S66
TBDATA,19,47.5E-12                              ! S44
TBDATA,21, 47.5E-12                             ! S55

/com    PIEZO MATRIX PIEZOELECTRIC STRESS MATRIX [d], [C/N]
![d] matrix is associated with the compliance matrix [S]
TB,PIEZ,1,,,1                          ! DEFINE PIEZ. TABLE
TBDATA,3, -171E-12                     ! d31 PIEZOELECTRIC CONSTANT
TBDATA,6, -171E-12                     ! d32 PIEZOELECTRIC CONSTANT
```

```
TBDATA,9, 374E-12                                ! d33 PIEZOELECTRIC CONSTANT
TBDATA,14, 584E-12                               ! d42 PIEZOELECTRIC CONSTANT
TBDATA,16, 584E-12                               ! d51 PIEZOELECTRIC CONSTANT
!TBLIST

/com    PERMITTIVITY AT CONSTANT STRAIN
EMUNIT,EPZRO,8.85E-12       ! FREE-SPACE PERMITTIVITY 8.85E-12 F/M.
MP,PERX,1,173                ! PERMITTIVITY (X DIRECTION) relative permittivity
MP,PERY,1,1730               ! PERMITTIVITY (Y DIRECTION) relative permittivity
MP,PERZ,1,1700               ! PERMITTIVITY (Z DIRECTION) relative permittivity
/com    Density
MP,DENS,1,7750               ! Density for material 1
SAVE
!
*******************************************************************************
*****

! 3-D COUPLED-FIELD SOLID5,
ET,1,SOLID5,3
MAT,1
TYPE,1

/com START  BUILDING  THE  MODEL
BLOCK,0,L,0,W,0,thick,                           ! Define volume block,x1,x2,y1,y2,z1,z2

lsel,s,line,,1
LESIZE,1, , ,mesh_size_w, , , , ,1
lsel,s,line,,2
LESIZE,2, , ,mesh_size_l, , , , ,1
lsel,s,line,,9
LESIZE,9, , ,mesh_size_thick, , , , ,1

VMESH,1 ! mesh volume 1

lsel,all
NSEL,S,LOC,Z,0       ! SELECT NODES AT TOP ELECTRODE  nsel- select a subset of nodes
CM,bottom_elec,NODE     ! CREATE A COMPONENT FOR THE BOTTOM SURFACE
CP,1,VOLT,ALL              ! COUPLE VOLT DOF ON NODES OFF  BOTTOM SURFACE
*GET,N1,NODE,,NUM,MIN      ! GET NODE ON ELECTRODE i,e Pick a node in this group
ALLSEL

NSEL,S,LOC,Z,thick    ! SELECT NODES AT TOP ELECTRODE nsel-select a subset of nodes
CM,top_elec,NODE                ! CREATE A COMPONENT FOR THE TOP SURFACE
CP,2,VOLT,ALL                    ! COUPLE VOLT DOF ON NODES OFF  TOP SURFACE
*GET,N2,NODE,,NUM,MIN    ! GET NODE ON ELECTRODE i,e Pick a node in this group
ALLSEL
```

```
FINISH                          ! Finish pre-processing
! ******************************************************************************
!/STATUS,SOLU
/SOLU                                ! ENTER THE SOLUTION PROCESSOR

/COM, BOUNDARY CONDITIONS
D,bottom_elec,VOLT,0                 ! GROUND BOTTOM ELECTRODE
D,top_elec,VOLT,1.0                  ! APPLY 1 VOLT TO TOP ELECTRODE
ALLSEL

! ******************************************************************************
/SOLU
EQSLV,Sparse
ANTYP,HARMIC,NEW
HROPT,FULL
HROUT,ON
OUTRES,ALL,NONE
OUTRES,RSOL,ALL
HARFRQ,0,1e+6                     ! Frequency range
dmprat,0.0001                     ! damping coefficient
NSUBST,1000                       ! number of subsets for each set
KBC,1
ALLSEL

/STATUS,SOLU         ! Provide a solution status summary
SOLVE
SAVE
FINISH                ! Exit active processor
!/COM EXIT,NOSAVE

!
********************************************************************************
*****
/POST26                       ! Enter post processor
/UI,COLL,1                    ! Activates specified GUI dialog boxes
RFORCE,2,N2,AMPS              ! STORE CHARGES Q ON ELECTRODE,! reaction data
```

- **Matlab Code used to compare the numerical to the analytical results**

```
%% analytical and numerical impedance of a PZT (l>>b>>h): 1-D assumption
function [ ]=impedance
%% analytical impedance
clear all
clc
l=20e-3;                          %length of PZT
b=1e-3;                           %width of PZT
h=0.5e-3;                         %thickness of PZT
s11=16.4e-12;                     %compliance coefficient s11
d31=-171e-12;                     % piezoelectric coupling d31
ep0=8.854e-12;
ro=7750;                          %density
eps33=1700*ep0;                   % relative permittivity
Cap=(eps33*b*l)/h;                % Capacitance of the PZT
k31=sqrt((d31^2)/(s11*eps33));    % coupling factor
f=1000:1000:1e+6;                 %frequency range
w=2*pi*f;
c=sqrt(1/(ro*s11));               %wave speed
gamma=w/c;                        %wave number
phi=0.5*gamma*l;
Za=(1./(i*w*Cap)).*((1-(k31)^2*(1-(tan(phi)./phi)))).^(-1);   % analytical impedance
figure (1)
plot(f,log10(abs(Za)),'r')
title('IMPEDANCE')
xlabel('Frequency(Hz)')
ylabel('Magnitude');
legend('---')
hold on
%%  numerical impedance
load hong.txt            % save the output of ansys under the name imped.txt, edit it (delte the text part) and load it in matlab
f=hong(:,1);                  % frequency
rl=hong(:,2);                 % real part
im=hong(:,3);                 % imaginary part
Y=(2*pi*i).*f.*(rl+1i*im);    % admittance
Zn=1./Y;                      % impedance
plot(f,log10(abs(Zn)),'b')
h = legend('Analytical Impedance','Numerical Impedance',2);
end
%%
```

APPENDIX B

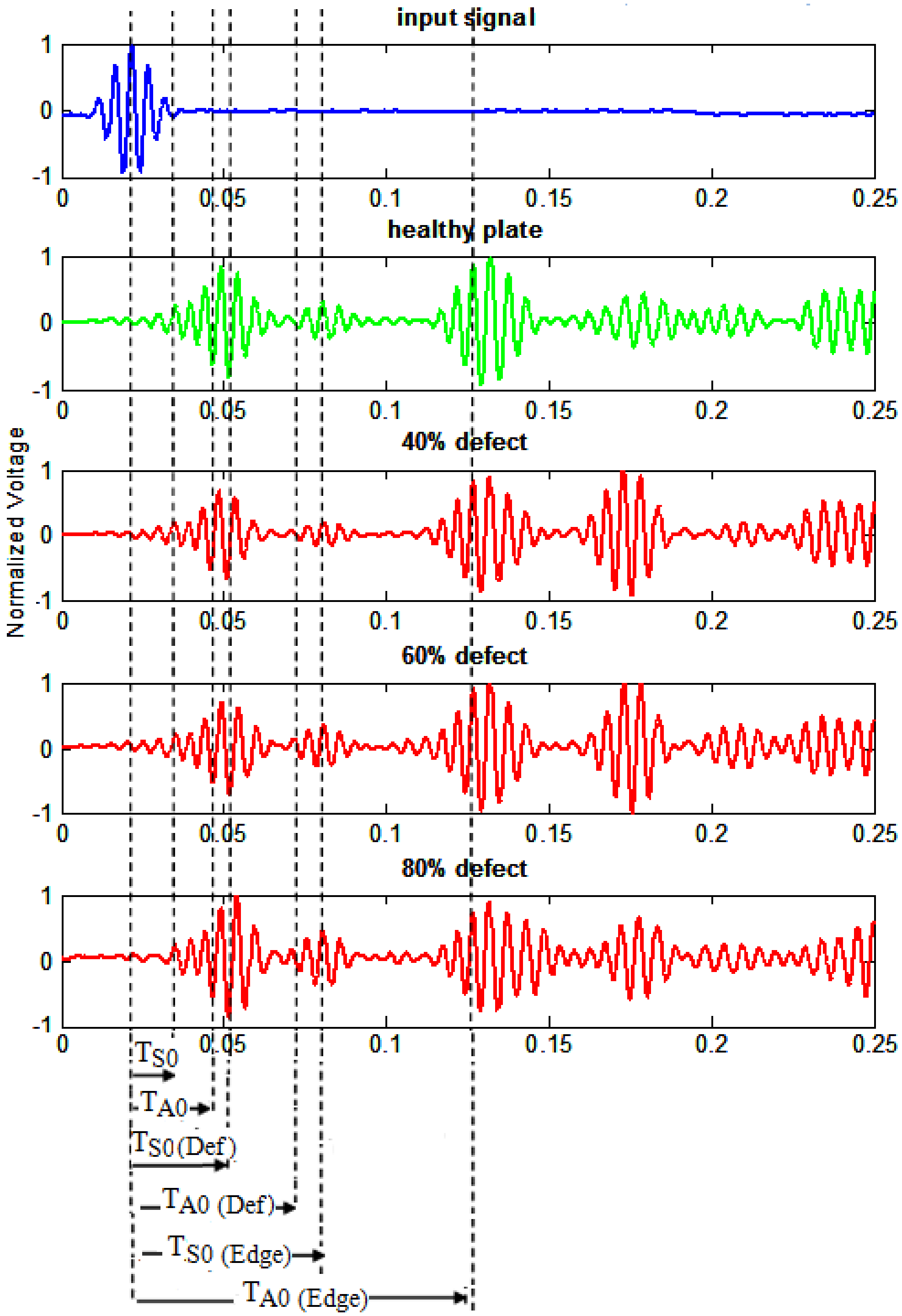

Figure B.01: Experimental signals at 100 KHz

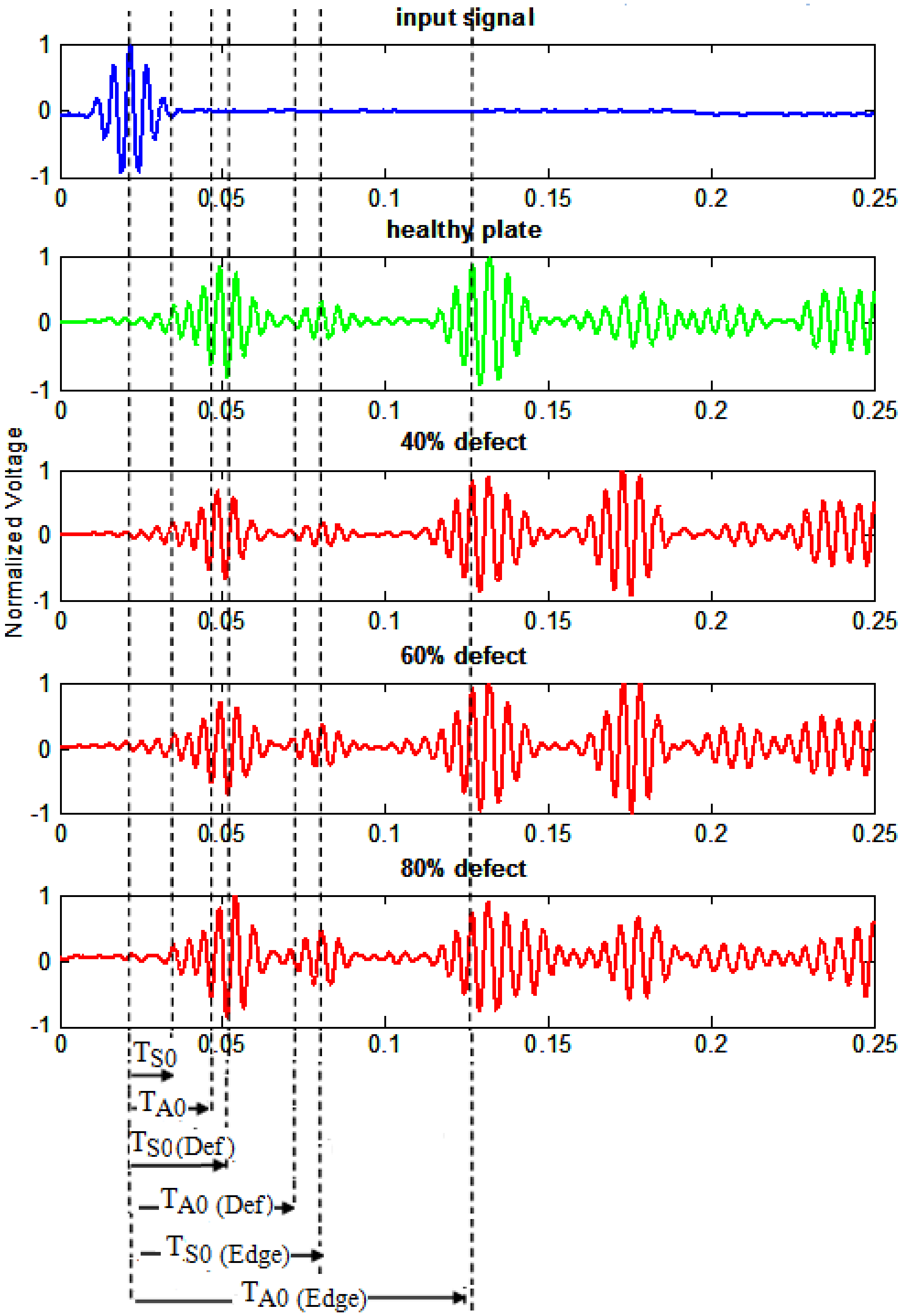

Figure B.02: Experimental signals at 125 KHz.

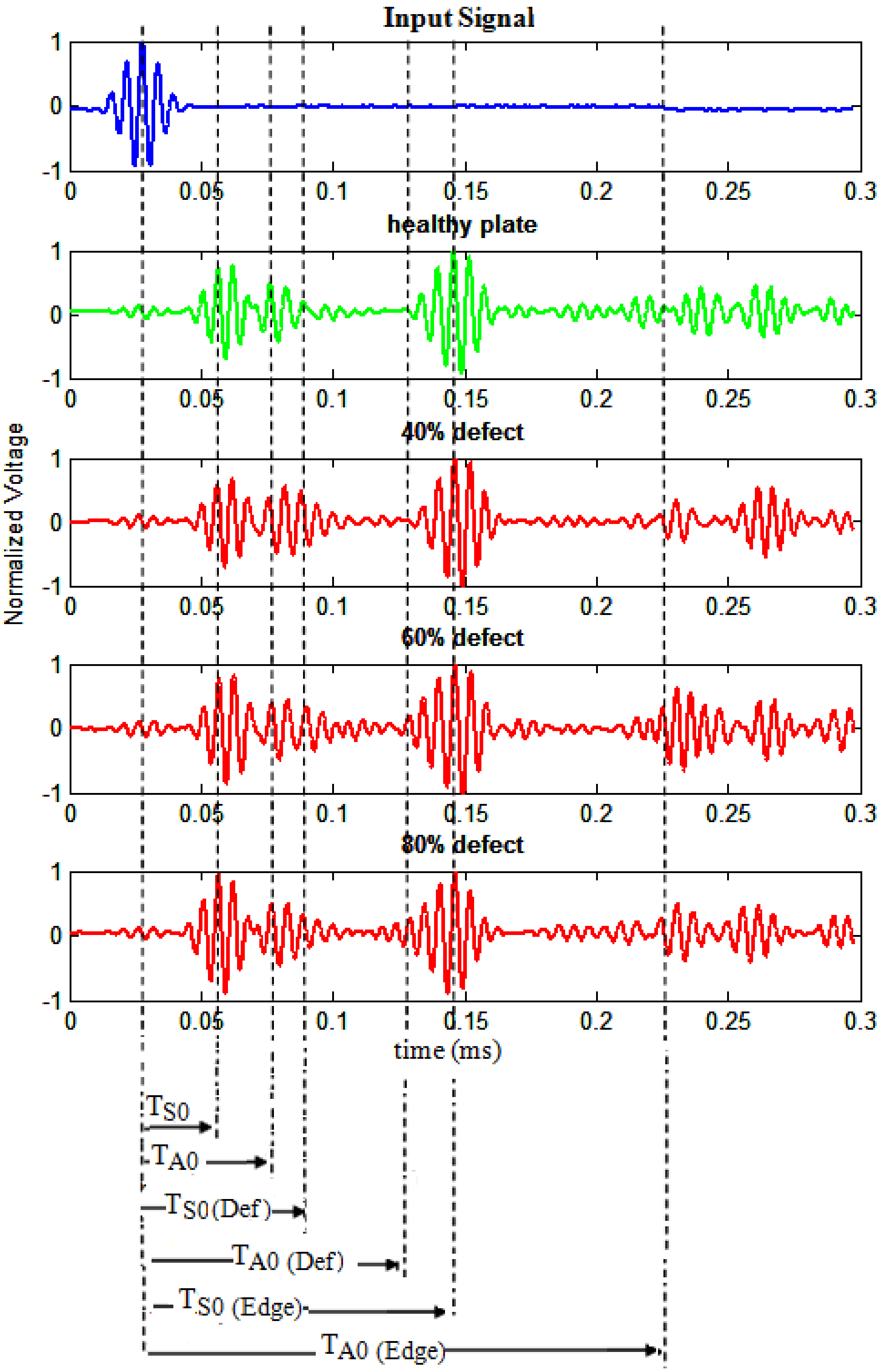

Figure B.03: Experimental signals at 150 KHz.

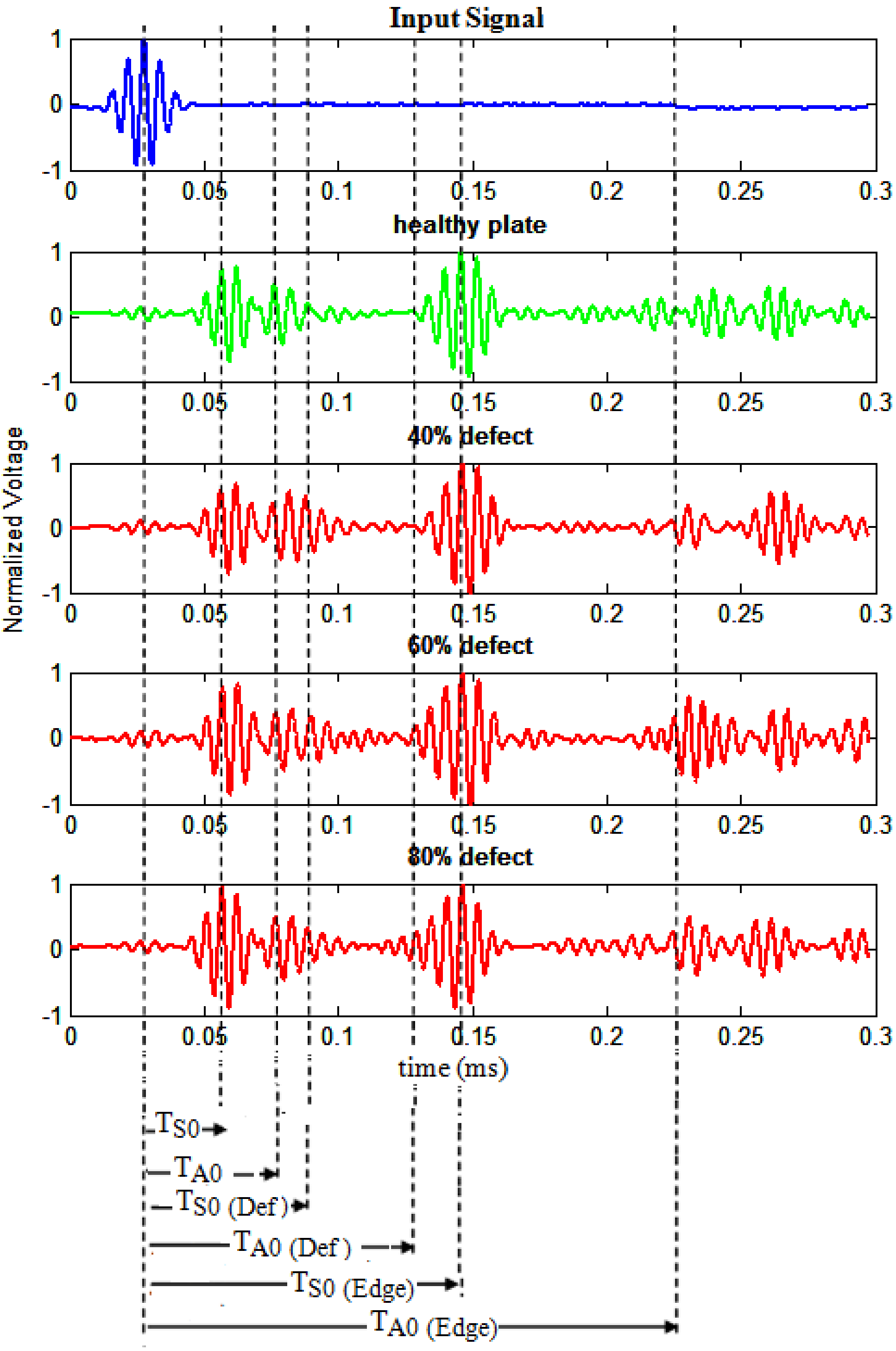

Figure B.04: Experimental signals at 175 KHz.

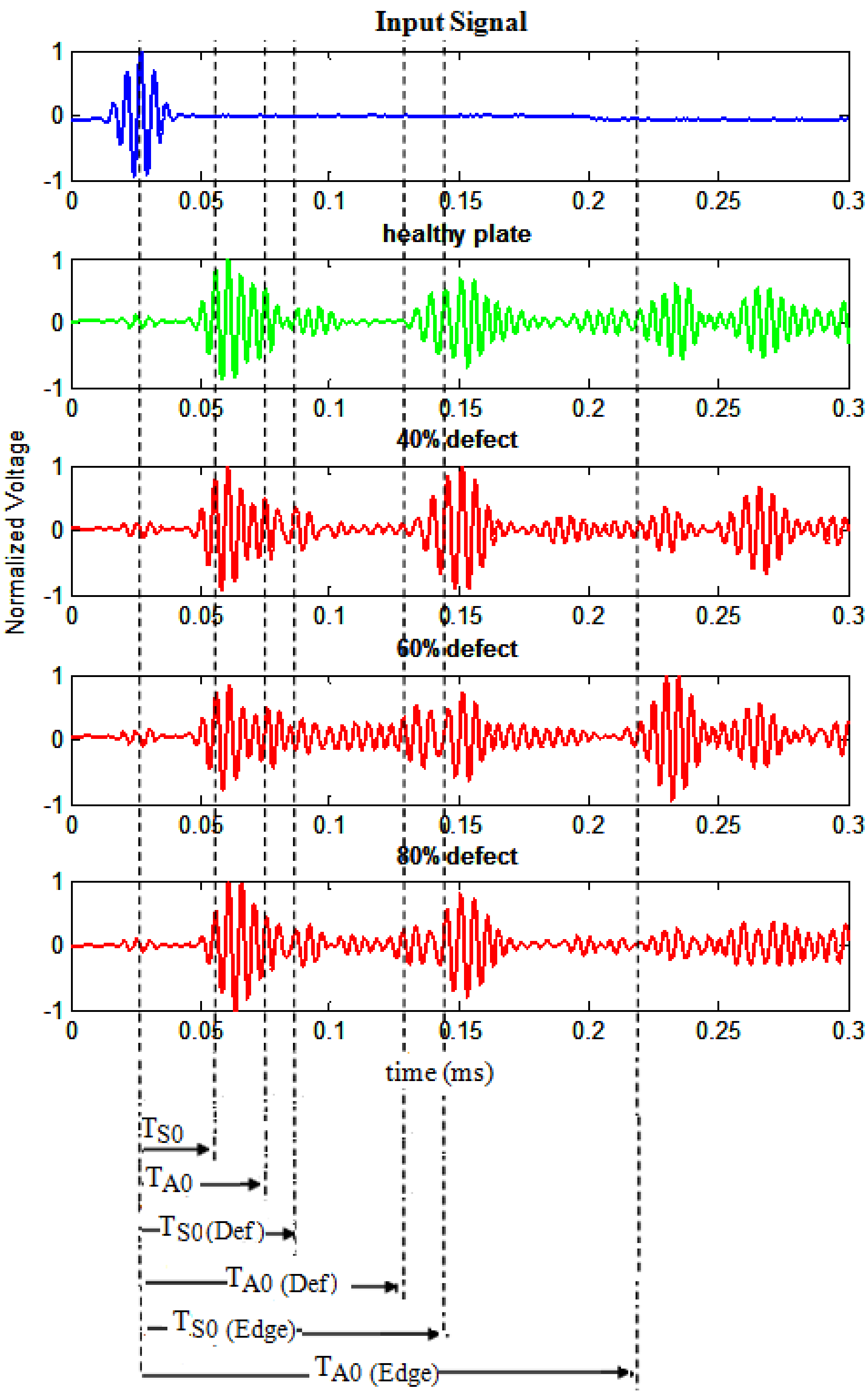

Figure B.05: Experimental signals at 200 KHz.

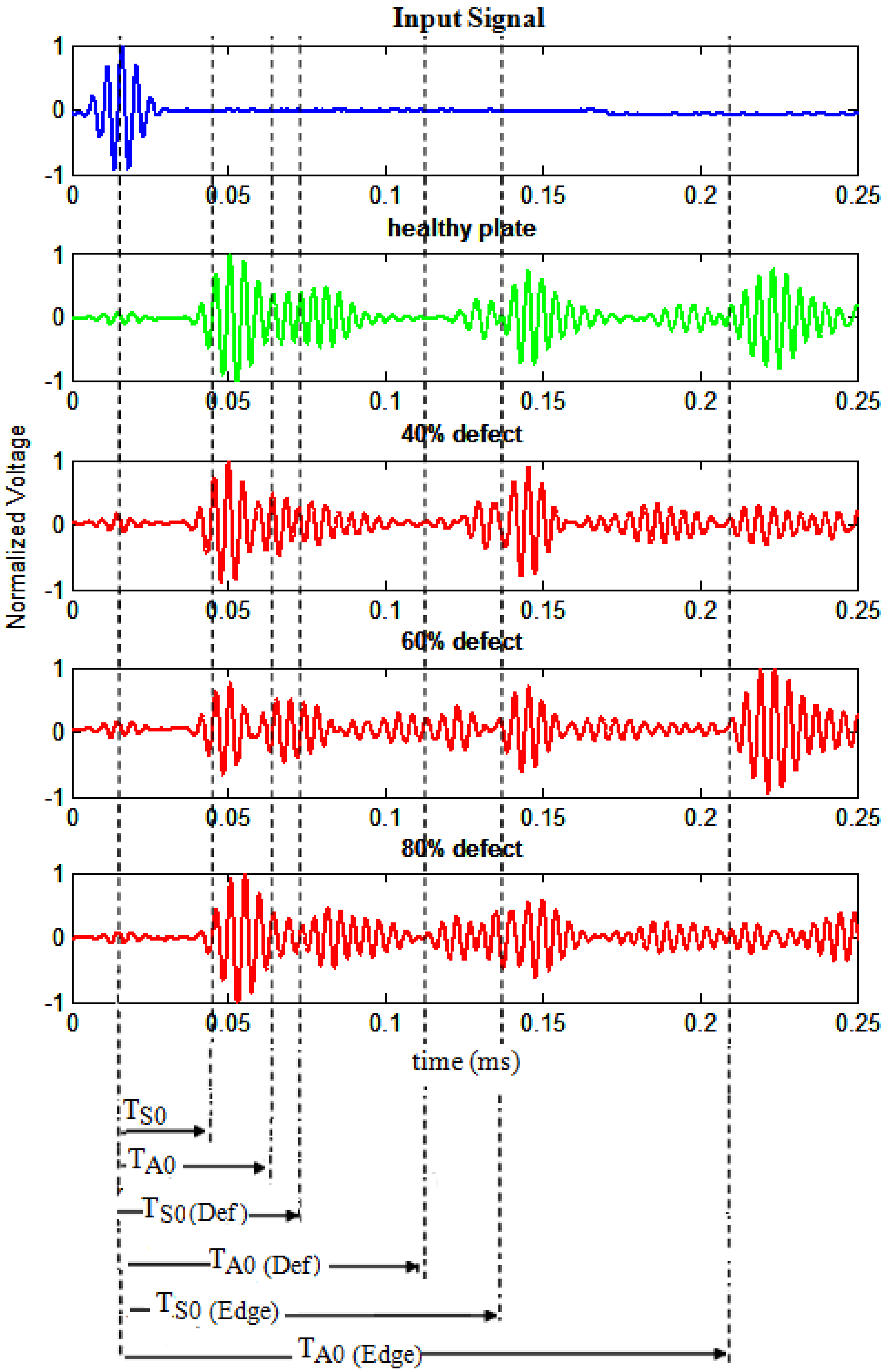

Figure B.06: Experimental signals at 225 KHz.

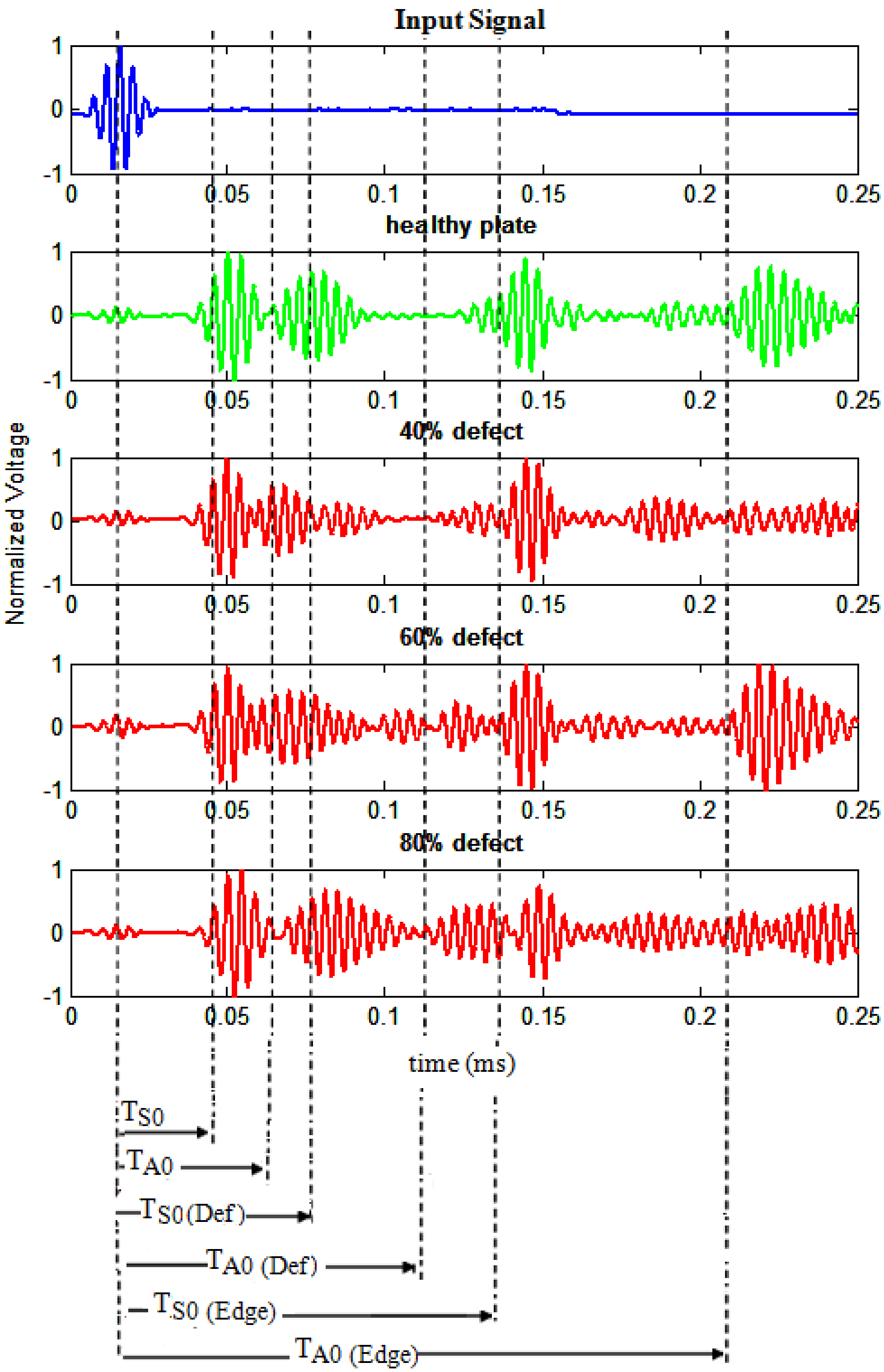

Figure B.07: Experimental signals at 250 KHz.

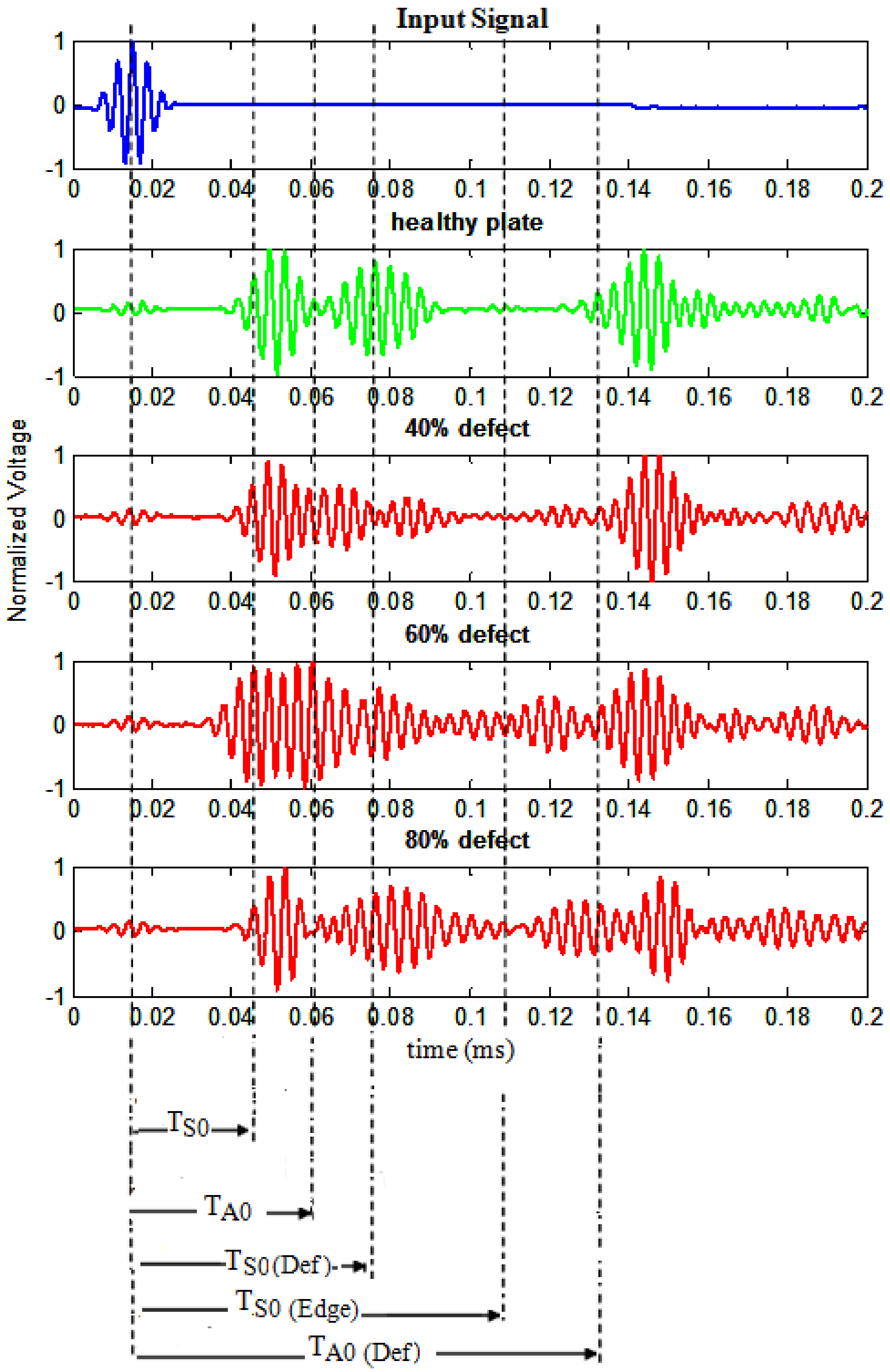

Figure B.08: Experimental signals at 275 KHz.

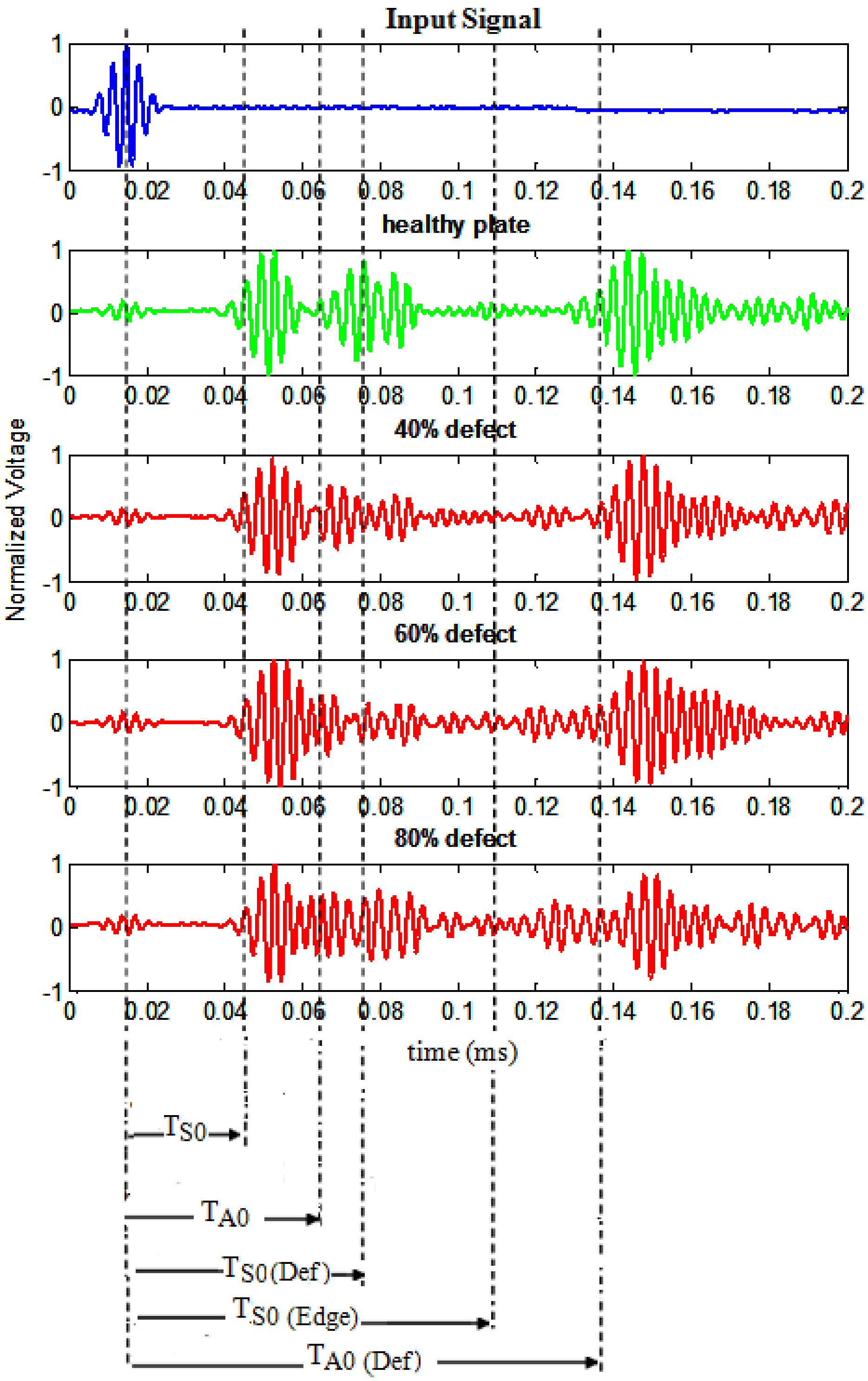

Figure B.09: Experimental signals at 300 KHz.

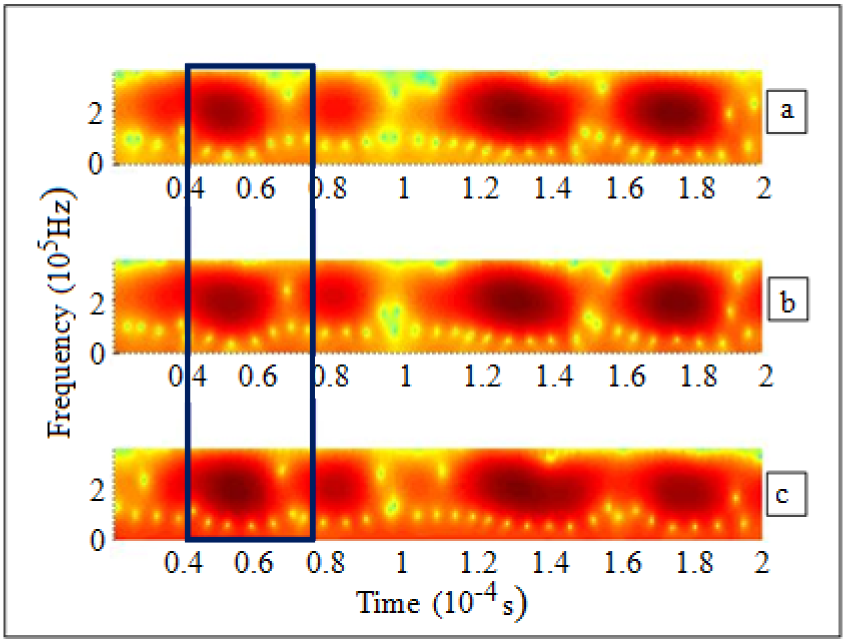

Figure B.10: Time– frequency representation at 100 KHz for deferent crack depths

(a) 40% TW (b) 60% TW (c) 80% TW

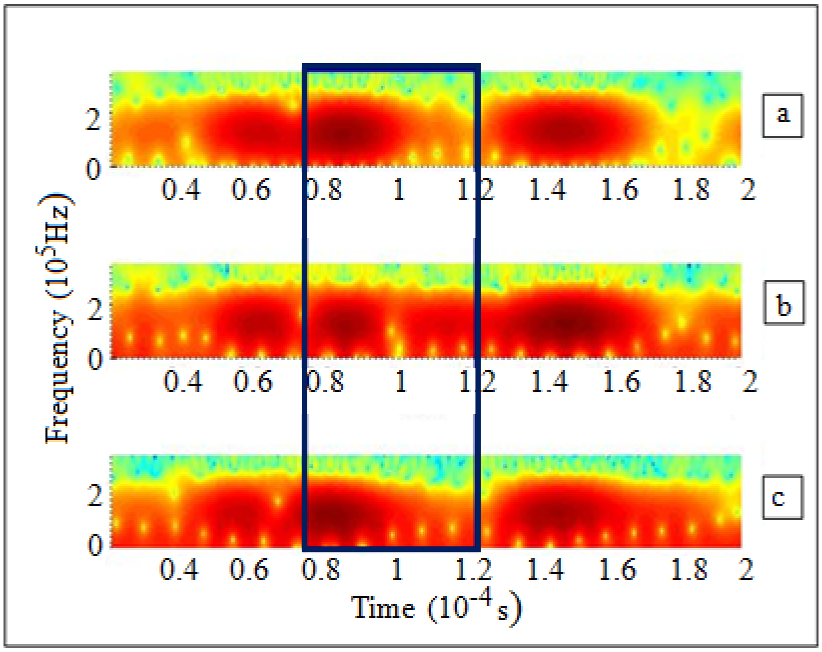

Figure B.11: Time – frequency representation at 125 KHz for deferent crack depths

(a) 40% TW (b) 60% TW (c) 80% TW

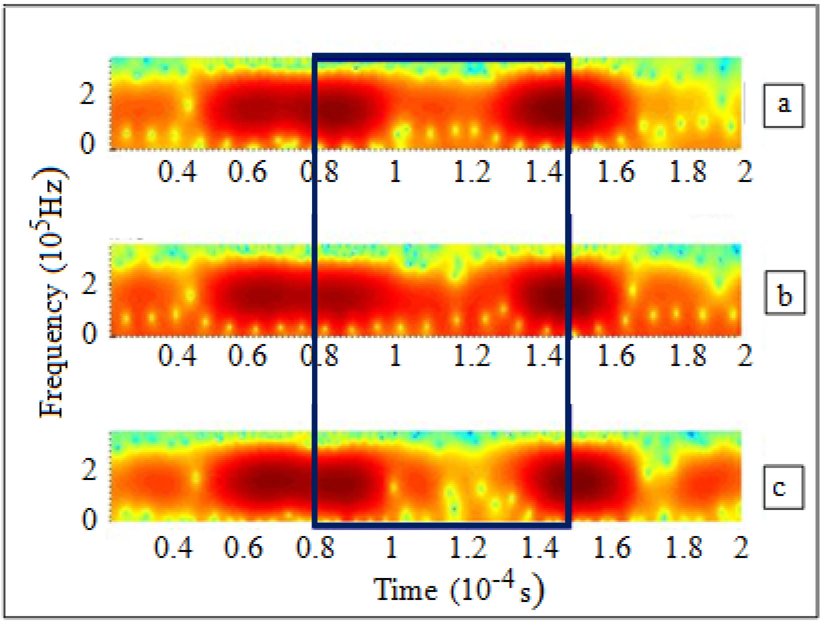

Figure B.12: Time – frequency representation at 150 KHz for deferent crack depths

(a) 40% TW (b) 60% TW (c) 80% TW

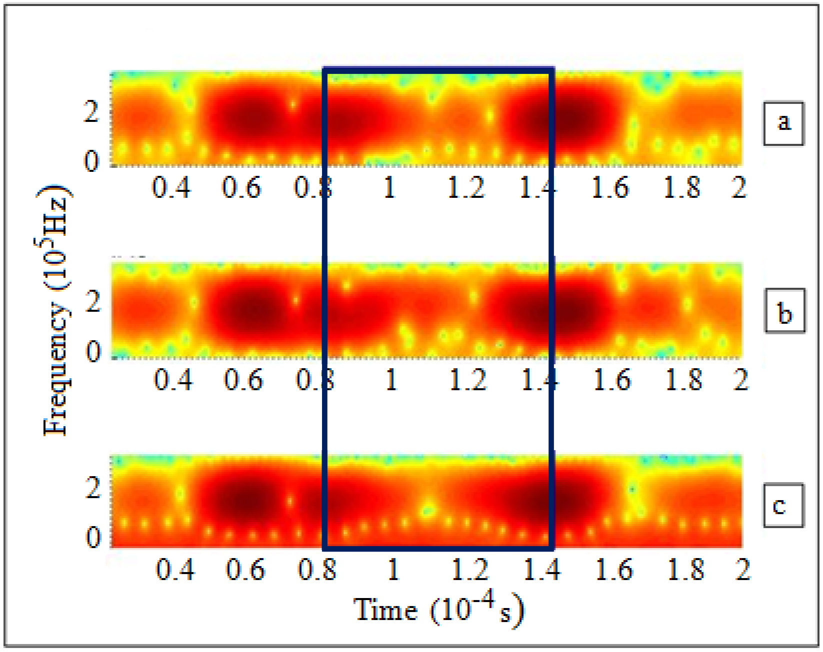

Figure B.13: Time – frequency representation at 175 KHz for deferent crack depths

(a) 40% TW (b) 60% TW (c) 80% TW

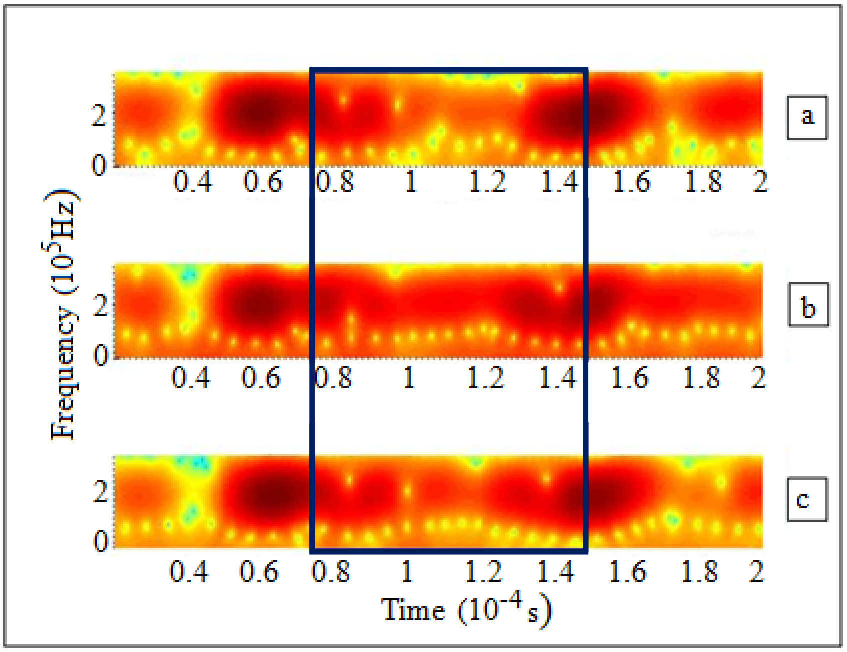

Figure B.14: Time – frequency representation at 200 KHz for deferent crack depths

(a) 40% TW (b) 60% TW (c) 80% TW

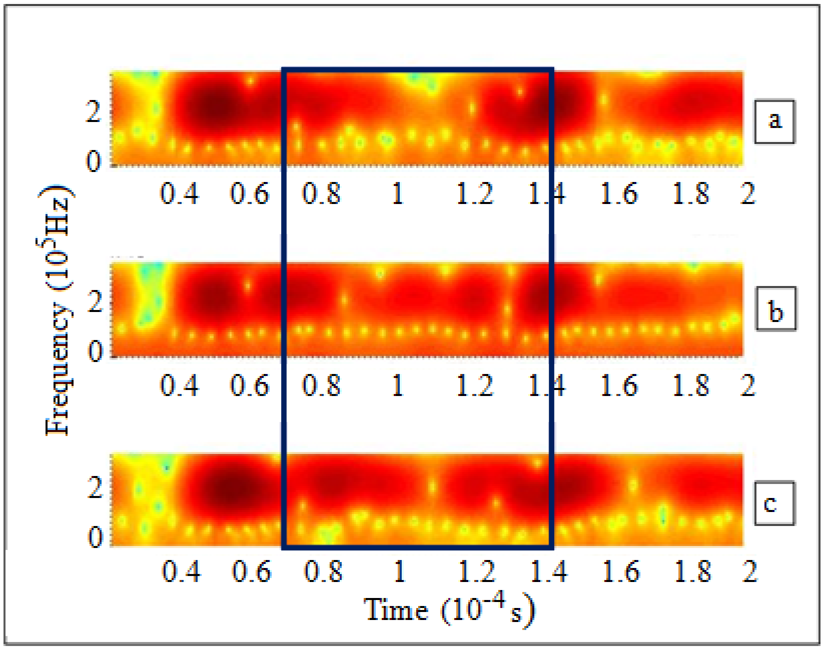

Figure B.15: Time – frequency representation at 225 KHz for deferent crack depths

(a) 40% TW (b) 60% TW (c) 80% TW

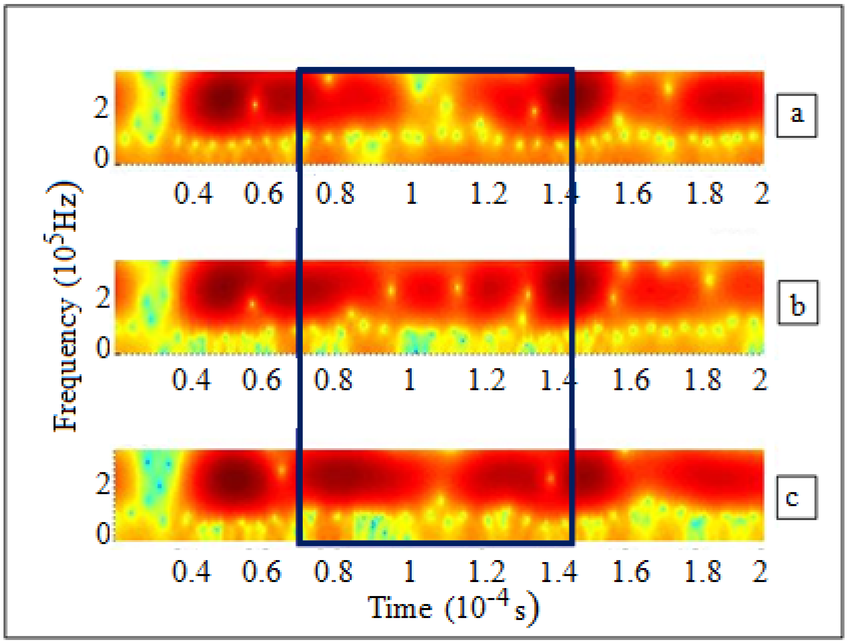

Figure B.16: Time – frequency representation at 250 KHz for deferent crack depths

(b) 40% TW (b) 60% TW (c) 80% TW

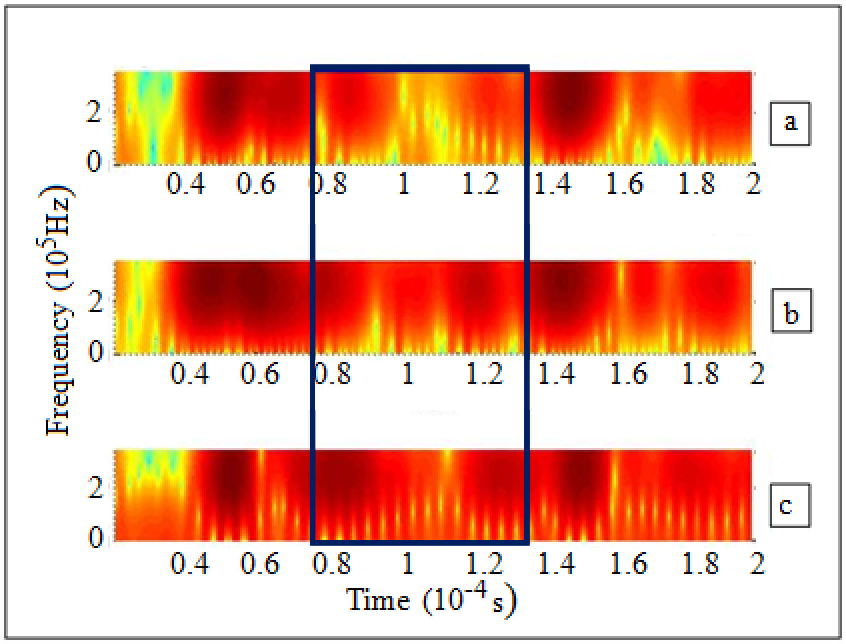

Figure B.17: Time – frequency representation at 275 KHz for deferent crack depths

(a) 40% TW (b) 60% TW (c) 80% TW

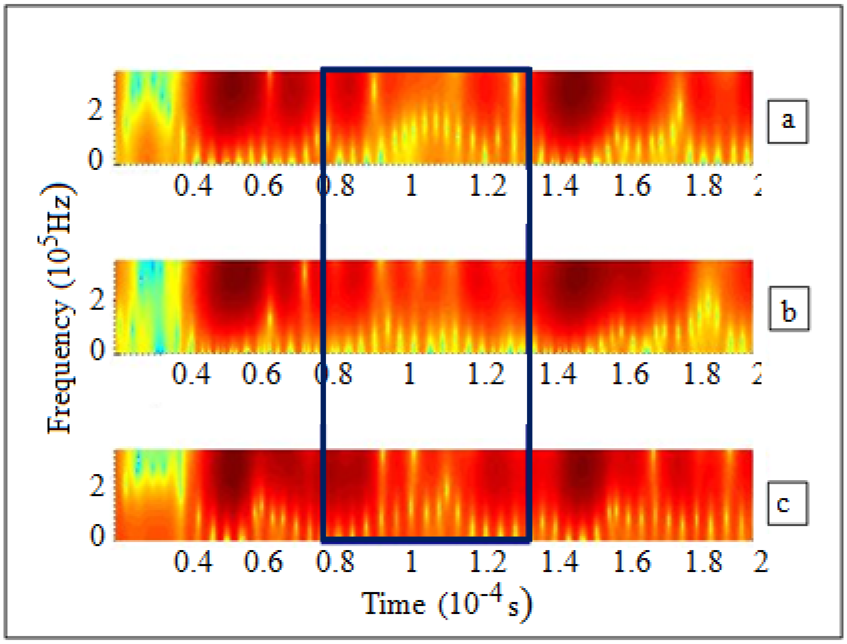

Figure B.18: Time – frequency representation at 300 KHz for deferent crack depths

(a) 40% TW (b) 60% TW (c) 80% TW

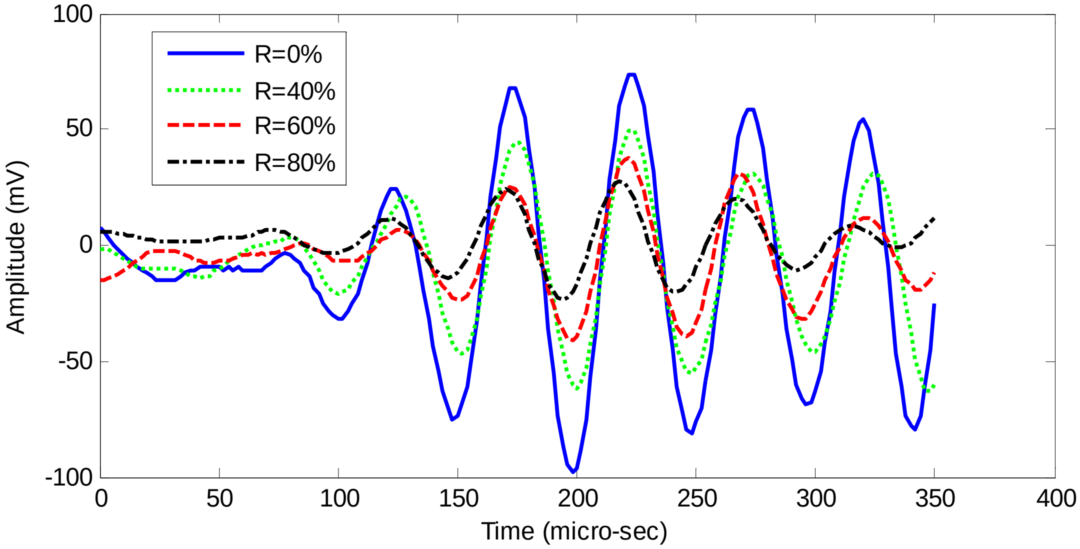

Figure B.19: S0 mode at 100 KHz for deferent crack depths

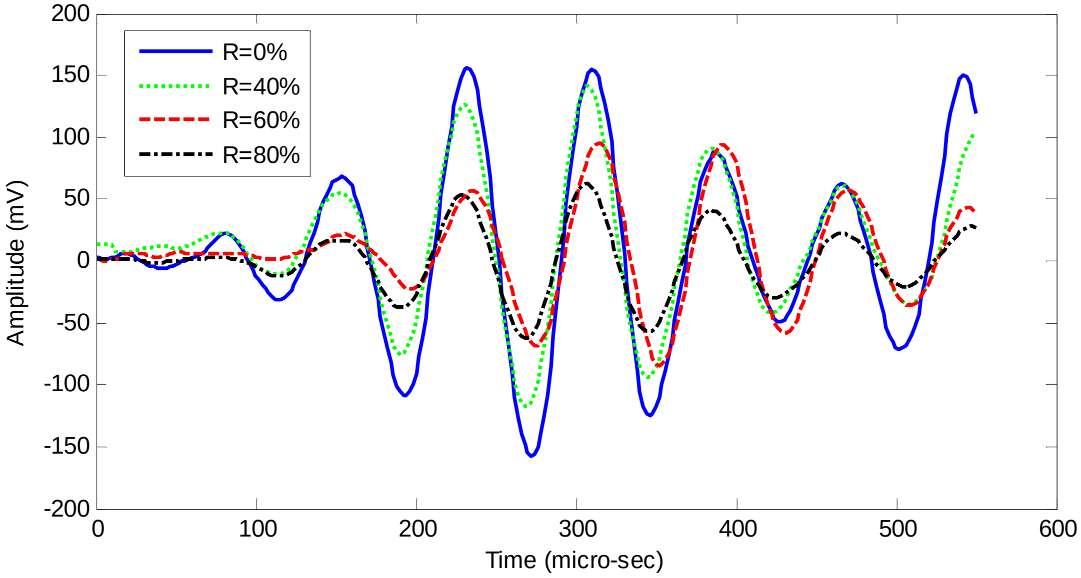

Figure B.20: S0 mode at 125 KHz for deferent crack depths

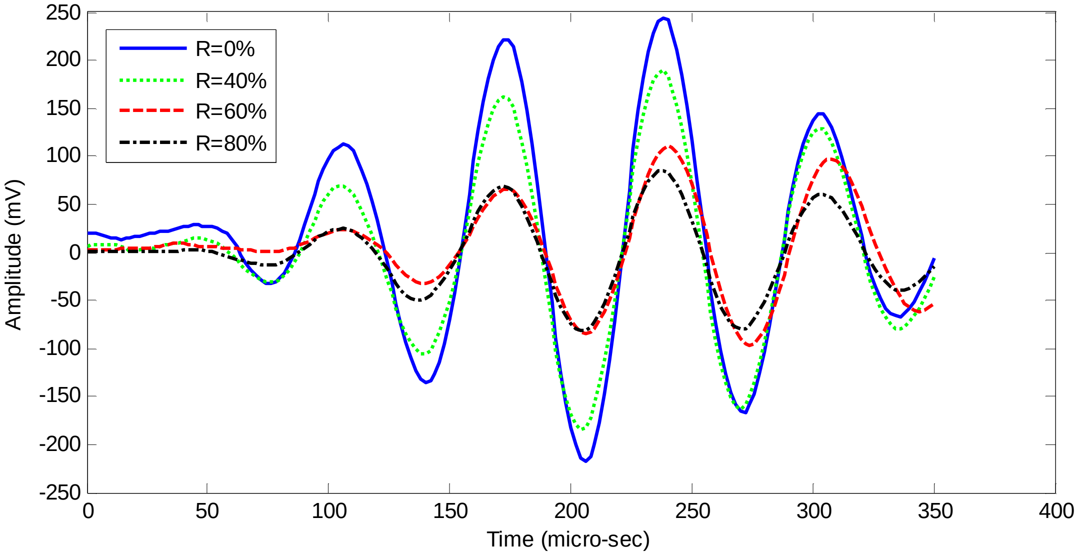

Figure B.21: S0 mode at 150 KHz for deferent crack depths

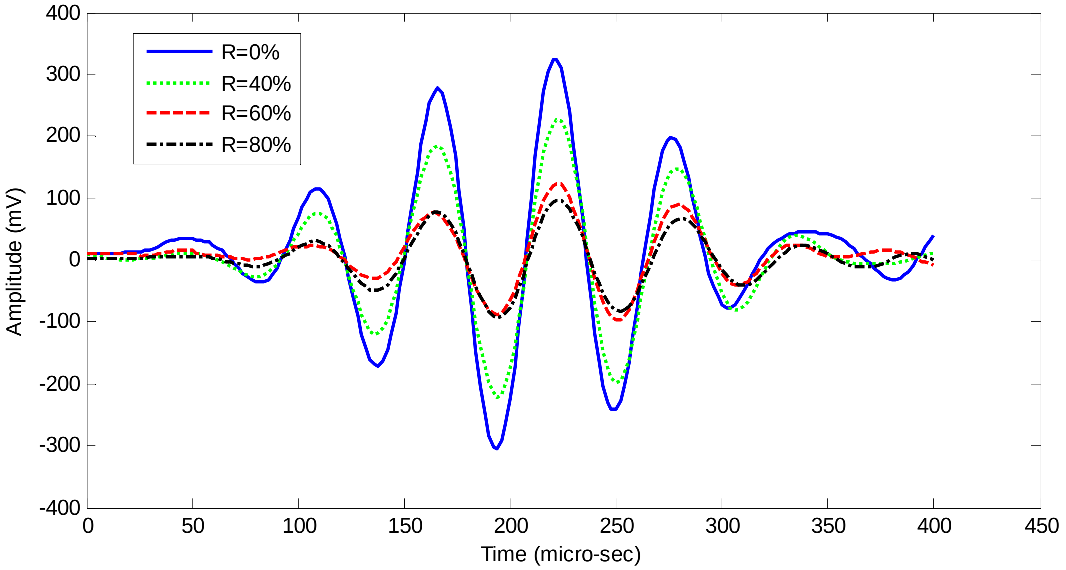

Figure B.22: S0 mode at 175 KHz for deferent crack depths

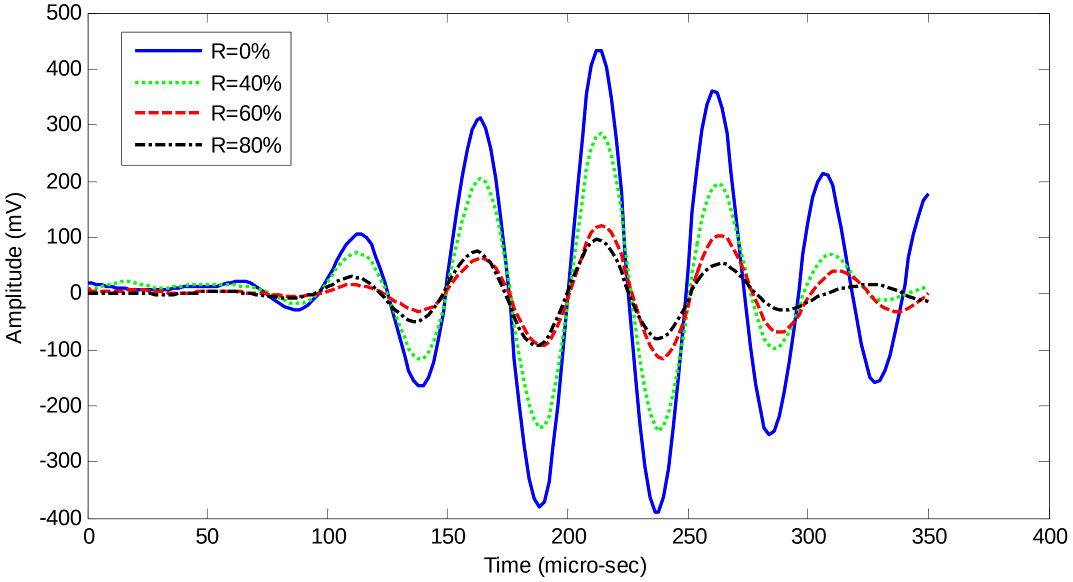

Figure B.23: S0 mode at 200 KHz for deferent crack depths

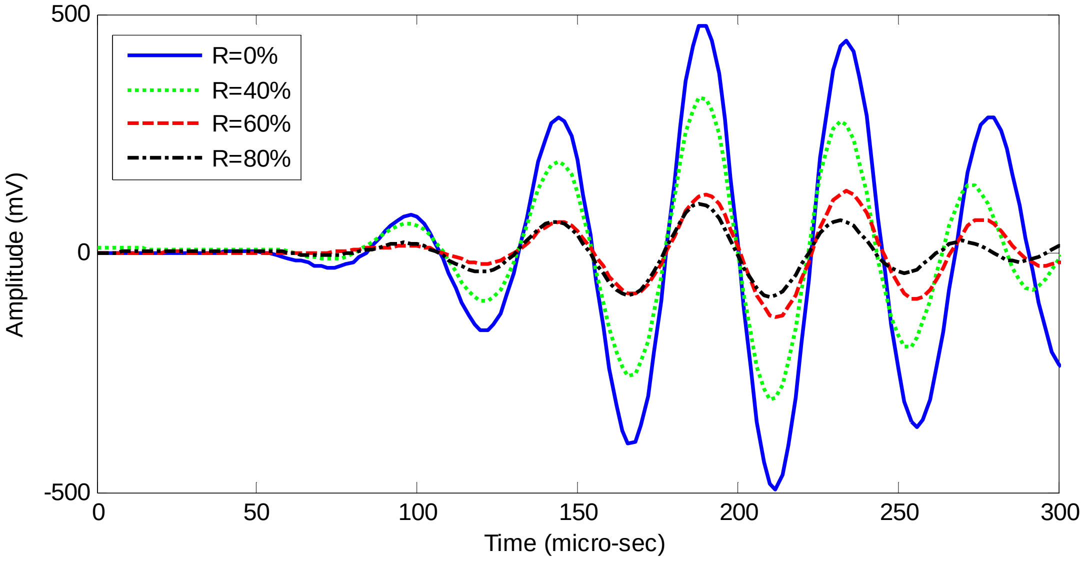

Figure B.24: S0 mode at 225 KHz for deferent crack depths

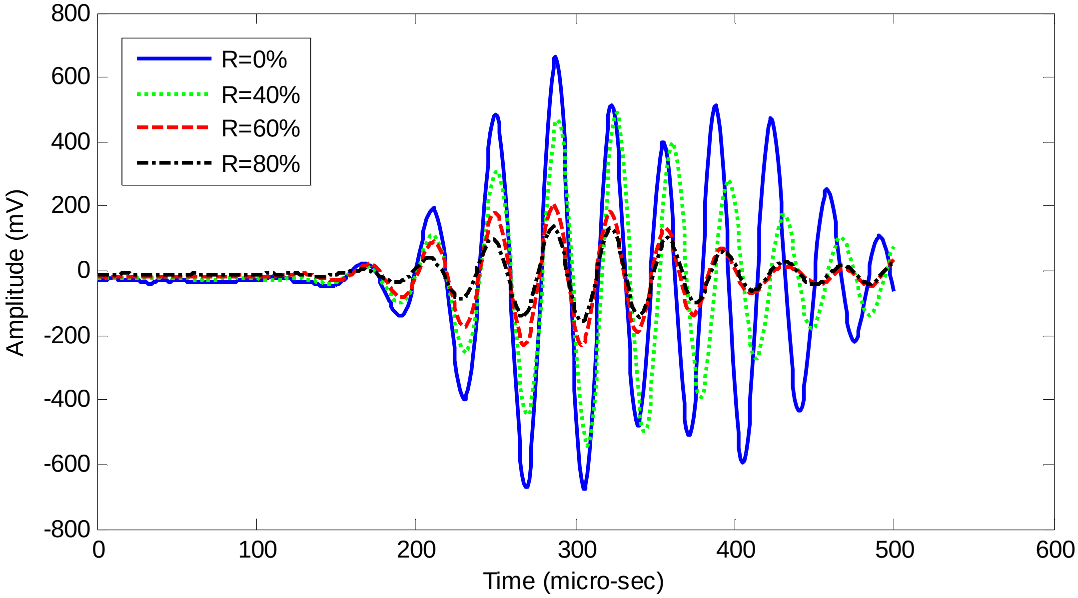

Figure B.25: S0 mode at 275 KHz for deferent crack depths

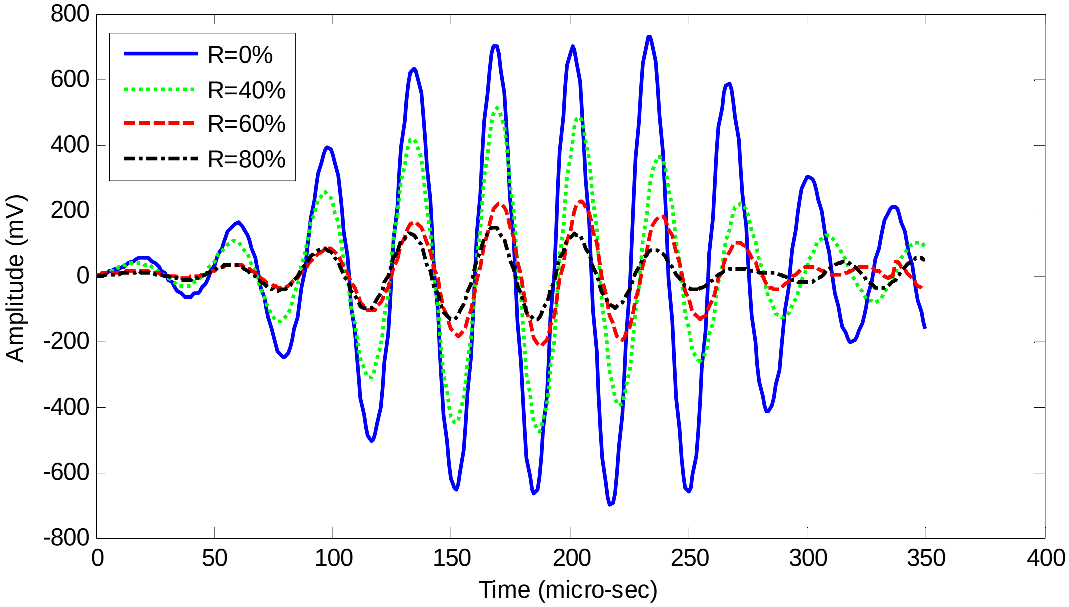

Figure B.26: S0 mode at 300 KHz for deferent crack depths

BIBLIOGRAPHY

BIBLIOGRAPHY

[01] Alleyne, D.N., Cawley, P. (Documentation) (1990), “A 2-dimensional Fourier transform method for the quantitative measurement of Lamb modes”, IEEE Ultrasonics Symposium, 1990, p. 1143-1146.

[02] Alleyne, D.N., Cawley, P. (1991), “The measurement and prediction of Lamb wave interaction with defects”, IEEE Ultrasonics Symposium, 1991, p. 855-857.

[03] Alleyne, D.N., Cawley, P. (1992), “The interaction of Lamb waves with defects. IEEE Transactions on Ultrasonics”, Ferroelectrics (Azar, 2000) (Balageas) (Bar-Cohen, 1998) and frequency control. 39 N° 3, 1992, p. 381-397.

[04] ANSYS Documentation: http://www.kxcad.net/ansys/ANSYS/ansyshelp/ansys.set.html.

[05] Azar et al (2000) Azar, L., Shi, Y. and Wooh, S. C. (2000) “Beam focusing behavior of linear phased arrays” NDT&E Int. 33 189–98.

[06] Balageas, D., Fritzen, C.-P., and Gemes, A. (2006), “Structural Health Monitoring”, ISTE, London, England.

[07] Bar-Cohen, Y., Mal, A., Chang, Z. (1998) “Composite material defects characterization using leaky lamb wave dispersion data”. SPIE`s NDE Techniques for Aging Infrastructure & Manufacturing. N: 3396-25.

[08] Bouraszeau, N. (2001), “(Bourasseau, 2001)”. Thèse de doctorat, 2001, Université de Valenciennes et du Hainaut Cambrèsis. N° d’ordre : 01-13.

[09] Deutsch, W. A. K., Cheng, A. and Achenbach, J. D. (1997) “Self-focusing of Rayleigh waves and Lamb waves with a linear phased array”. Research in Nondestructive Evaluation, 9(2):81–95, 1997.

[10] Doebling, S. W., Farrar, C. R., Prime, M. B., and Shevitz, D. W. (1996), “Damage identification and health monitoring of structural and mechanical systems from changes in their vibration characteristics: A literature review”, Tech. Rep. Report Number LA-13070-MS, Los Alamos National Laboratory, Los Alamos, NM.

[11] Ecke, W., Latka, I., Willsch, R., Reutlinger, A., Graue, R. (2001), “Fibre optic sensor network for spacecraft health monitoring”, Journal of Measurement Science and Technology, Volume 12 Number 7, (2001 (Ecke, 2001)), pp 974–980

[12] FHWA (2005), “Railroad Safety Statistics (FHWA, 2005) 2005 Annual Report“.

[13] FHWA (2006), “2006 Status of the Nation's Highways, Bridges, and Transit: Conditionsand Performance”. http://www.fhwa.dot.gov/policy/2006cpr/pdfs.htm

[14] Ghosh, D. P. and Gopalakrishnan, S., (2003) "Structural health monitoring in a composite beam using magnetostrictive material through a new FE formulation", Proc. SPIE, Vol. 5062, 704 (2003); doi:10.1117/12.514687

[15] Giurgiutiu, V., Jichi, F., Rogers, C. A., Quattrone, R., Berman, J. B., Kamphaus, J. (1999), "Experimental Study of Magnetostrictive Tagged Composite Strain Sensing Response for Structure Health Monitoring" 2nd International Workshop of Structural Health Monitoring, Sept. 8-10, 1999, Stanford University.

[16] Giurgiutiu, V. and Zagrai, A.N. (2000) "Characterization of Piezoelectric Wafer Active sensors". Journal of Intelligent Material Systems and Structures, Vol. 11 – December 2000.

[17] Giurgiutiu, V. and Bao, J. (2002) "Embedded Ultrasonic Structural Radar for the Nondestructive Evaluation of Thin-Wall Structures". In Proceedings of the 2002 ASME International Mechanical Engineering Congress, pages 17–22, 2002.

[18] Giurgiutiu, V., Zagrai, A., and Bao, J. (2004), "Damage identification in aging aircraft structures with piezoelectric wafer active sensors," Journal of Intelligent Material Systems and Structures, Vol. 15, No. 9-10, pp. 673–687.

[19] Giurgiutiu (2004) "Health Monitoring With Piezoelectric Wafer Active Sensors". p-247

[20] Giurgiutiu, V. and Cuc, A. (2005), "Embedded non-destructive evaluation for structural health monitoring, damage detection, and failure prevention", Shock and Vibration Digest, Vol. 37, No. 2, pp. 83 – 105.

[21] Giurgiutiu, V. (2008), "Structural Health Monitoring With Piezoelectric Wafer Active Sensors", Academic Press, London, England.

[22] Grisso, B. L. and Inman, D. J. (2006), "Impedance-based structural health monitoring of thermal protection systems," Proceedings of SPIE - The International Society for Optical Engineering, Nondestructive Evaluation and Health Monitoring of Aerospace Materials, Composites, and Civil Infrastructure V, February 26 - March 2, San Diego, CA, Vol. 6176, p. 61760M.

[23] Grondel, S. (2000), "Contribution à l'optimisation du contrôle santé intégré par ondes de Lamb : Application à la surveillance de structures aéronautiques". Thèse de doctorat, 2000, Université de Valenciennes et du Hainaut Cambrèsis. N° d'ordre : 00-34.

[24] Guo, N. Cawley, P. (1993), "The interaction of Lamb waves with delaminations in composite laminates" Journal of Acoustical Society of America. 94 (4), 1993, p. 2240-2246.

[25] Han, S., Palazotto, A.N., Asce, F., and Leakeas, l., (2009) "Finite-element analysis of lamb wave propagation in a thin aluminum plate" Journal of Aerospace Engineering 10.1061/ASCE 0893-1321 (2009) 22:2(185).

[26] Inman, D. J., Farrar, C. R., Lopes Jr., V., and Steffen Jr., V. (2005), “Damage Prognosis: For Aerospace, Civil and Mechanical Systems”, John Wliey & Sons, Chichester, West Sussex, England.

[27] Kannappan, L., Shankar, K. (2007), “Non destructive inspection of plates using frequency measurements”, 5th Australasian Congress on Applied Mechanics, ACAM 2007 10-12 December 2007, Brisbane, Australia.

[28] Kim, S.B., Sohn, H. (2007), “Instantaneous reference-free crack detection based polarization characteristics of piezoelectric materials”, Journal of Smart Materials and Structures. Vol. 16 (2007) 2375–2387

[29] Kwun, H., Light, G. M., Kim, S., and Spinks, R. L. (2002), “Magnetostrictive sensor for active health monitoring in structures,” Proceedings of SPIE - The International Society for Optical Engineering, Smart Nondestructive Evaluation for Health Monitoring of Structural and Biological Systems, March 17-21, San Diego, CA, Vol. 4702, pp. 282–288.

[30] Lamb, H. (1917) “On waves in an elastic plate” Proc. R. Soc. London, Ser. A, 93(648), 114-128.

[31] Liang, C., Sun, F., and Rogers, C. (1994), “Coupled electro-mechanical analysis of adaptive material systems - determination of the actuator power consumption and system energy transfer”, Journal of Intelligent Material Systems and Structures, Vol. 5, No. 1, pp. 12 – 20.

[32] Light, G.M., Kwun, H., Kim, S. Y., Spinks, R. L. (2003) ,“Health Monitoring of Piping and Plate Using the Magnetostrictive Sensor (MsS) Guided-Wave”, 2nd Middle East Nondestructive Testing Conference and Exhibition Proceedings, December 8-10, 2003.

[33] Lines, D. and Dickson, K. (1999) “Optimization of high-frequency array technology for lap-joint inspection”. Proceedings of the 3rd Joint Conference on Aging Aircraft.

[34] Liu, W. and Giurgiutiu, V., (2007), “Finite Element Simulation of Piezoelectric Wafer Active Sensors for Structural Health Monitoring with Coupled-Filed Elements”, Sensors and Smart Structures Technologies for Civil, Mechanical, and Aerospace Systems 2007.

[35] Lowe, M.J.S., Cawley, P., Kao, J-Y. Diligent, O. Prediction and measurement of the reflection of the fundamental anti-symmetric Lamb wave from cracks and notches. Review of Progress in Quantitative Nondestructive Evaluation, 509 (1), 25-30 July 1999, p. 193-200.

[36] Lowe, M.J.S., Cawley, P., Kao, J.Y., Diligent, O. (2002), “The low frequency reflection characteristics of the fundamental antisymmetric Lamb wave A0 from a rectangular notch in a plate”, J. Acoust. Soc. Am. 112 (6), 2002, p 2612-2622.

[37] Lowe, M.J.S., Diligent, O., “Low-frequency reflection characteristics of the S0 Lamb wave from a rectangular notch in a plate”. J. Acoust. Soc. Am. 111 (1), 2002, p 64-74.

[38] Lu, L., Ye, L., Su, Z., Yang, C. (2008), “Quantitative assessment of through-thickness crack size based on Lamb wave scattering in aluminum plates”, NDT&E International 41 (2008) 59–68.

[39] Measures, R. M. (2001), “Structural Monitoring with Fiber Optic Technology”, Academic Press, San Diego, CA.

[40] NTSB. “Aviation Accidents” http://www.ntsb.gov/

[41] Park, G., Sohn, H., Farrar, C. R., and Inman, D. J. (2003), “Overview of piezoelectric impedance-based health monitoring and path forward,” The Shock and Vibration Digest, Vol. 35, No. 6, pp. 451–463.

[42] Park, S., Ahmad, S., Yun, C. B., and Roh, Y. (2006), “Multiple crack detection of concrete structures using impedance-based structural health monitoring techniques”, Experimental Mechanics, Vol. 46, No. 5, pp. 609 – 618.

[43] Park, S., Chung-Bang, Y., Yongrae, R. (2007) “Damage diagonistics on a welded zone of a steel truss member using an active sensing network system”. NDT& E international ISSN 0963-8695, vol. 40, pp. 71-76.

[44] Raghavan, A. and Cesnik, C. E. (2007), “Review of guided-wave structural health monitoring”, Shock and Vibration Digest, Vol. 39, No. 2, pp. 91 – 114.

[45] Rippert, L., Papy, J-M., Wevers, M., Van Huffel, S. (2002), “, Fibre optic sensor for continuous health monitoring in CFRP composite materials”, Smart Structures and Materials, Proceedings of SPIE Vol. 4693 (2002), pp. 312 – 323.

[46] Shang, H. M., Tay, T. E., Lwin, M. (1992), “Holographic Inspection of Plates with Regions of Local Thinning as Defects”, Journal of Nondestructive Evaluation, Voume 11, No. 2, 1992.

[47] Sohn, H., Farrar, C., Hemez, F., Czarnecki, J., Shunk, D., Stinemates, D., and Nadler, B. (2001), “A review of structural health monitoring literature 1996-2001,” Tech. Rep. Report Number LA-13976-MS, Los Alamos National Laboratory, Los Alamos, NM.

[48] Su, Z., Ye, L., Lu, Y. (2006), “Guided Lamb waves for identification of damage in composite structures: a review”. Journal of Sound and Vibration. No 295 (2006), 753-780.

[49] Torvik, P.J. (1967), “Reflection of wave trains in semi infinite plates”, J. Acoust. Soc. Am. (1967), 99(4), pp. 346-353.

[50] Tua, P.S., Quek, T., Wang, Q. (2004), “Detection of cracks in plates using piezo-actuated Lamb waves”. Journal of Smart Materials and Structures. 13 (2004) 643–660.

[51] Wang, L., Yuan, F. G. (2007), “Active damage localization technique based on energy propagation of Lamb waves”, Smart Structures and Systems, Vol. 3, No. 2 (2007) 201-217.

[52] W. Liu, and Hong, J.W., (2010) “Three dimensional Lamb Wave propagation excited by a phased piezoelectric array” Journal of Smart Materials and Structures, Vol:19 N^0 8.

[53] Weber, Y. B., Schweitzer, D., Bar, H., Shilo, D. (2008), “Health Monitoring of Adhesive Joints using Magnetostrictive Fillers”, Proceedings of the 9th Biennial ASME Conference on Engineering Systems Design and Analysis ESDA 2008.

[54] Wilcox, P. D., Lowe, M. J. S. and Cawley, P. (2000) “Lamb and SH wave transducer arrays for the inspection of large areas of thick plates”. In Annual Review of Progress in QNDE volume 19A, pages 1049 – 1056, 2000.

[55] Worlton, D.C. (1957), “Ultrasonic Testing with Lamb Waves”, Nondestructive Testing, 15:218 222.

[56] Zhongqing S., Ye, L., “Identification of Damage Using Lamb Waves: From Fundamentals to Applications”, Lecture Notes in Applied and Computational Mechanics, Vol. 48.

[57] Zhou, Z. and Ou, J. (2004) “Development of FBG sensors for structural health monitoring in civil infrastructures”. Proceeding of North American Euro-Pacific Workshop “Sensing Issues in Civil Structural Health Monitoring”, 2004, Waikiki Beach, Oahu, Hawaii, USA.